Copyright 2013 Michael T. Marty

ANALYSIS OF MEMBRANE SYSTEMS USING LIPOPROTEIN NANODISCS

BY

MICHAEL T. MARTY

DISSERTATION

Submitted in partial fulfillment of the requirements
for the degree of Doctor of Philosophy in Chemistry
in the Graduate College of the
University of Illinois at Urbana-Champaign, 2013

Urbana, Illinois

Doctoral Committee:

Professor Stephen Sligar, Chair
Professor Jonathan Sweedler
Associate Professor Ryan Bailey
Assistant Professor Mary Kraft

ABSTRACT

Membrane systems play a critical role in biochemistry by regulating the chemical, energy, and information flow into the cell and its various compartments. However, the amphipathic nature of membrane proteins and lipids makes their analysis challenging. Engineered nanoscale lipoprotein Nanodiscs provide a well-defined and native-like lipid bilayer to solubilize membrane proteins and lipids. This dissertation details the analysis of Nanodiscs containing various membrane proteins and lipids with bioanalytical methods, including mass spectrometry and photonic biosensors.

Mass spectrometry offers several powerful techniques for fundamental characterization of Nanodiscs and Nanodisc-solubilized membrane proteins. Native mass spectrometry delivers single-lipid resolution of intact Nanodisc complexes to determine their mass distributions. Mass spectrometry-based proteomics demonstrates that heterogeneous Nanodisc-solubilized membrane protein libraries model the membrane proteome. Matrix-associated laser desorption ionization methods facilitate characterization of membrane proteins embedded in Nanodiscs.

To study biomolecular interactions involving membrane systems, silicon photonic microring resonator biosensors provide a multiplexed platform for detecting interactions between soluble proteins and Nanodiscs. A novel direct physisorption strategy was developed to interface Nanodiscs with the silica surface. Implementation of a nonlinear analyte gradient approach extends the capabilities of the microring resonator technology to single run kinetic experiments.

Mass spectrometry and silicon photonic biosensor techniques developed in this thesis extend the capabilities of the Nanodisc platform for the analysis of membrane systems and lay the foundation for future applications of Nanodiscs in biochemistry, target identification, and drug discovery.

ACKNOWLEDGEMENTS

A number of people have contributed both directly and indirectly to this dissertation. I first thank Prof. Stephen Sligar for his support, encouragement, and inspiration. By his example and teaching, Steve challenged me to become an inquisitive researcher, effective communicator, and independent scientist. His excitement and critical eye will continue to guide me throughout my career.

I thank all of the past and current members of the Sligar research group for their teaching and help. I joined the group with almost no experience in experimental biochemistry, and they have taught me more than they realize. Mark McLean, Tim Bayburt, and Lena Grinkova taught me fundamental biochemical methods, Nanodisc formation, and protein expression. Ilia Denisov provided critical insights on a number of topics. I thank Aditi Das for her contributions to the MALDI and SMPL work. Finally, thanks to Abhi Luthra, Mike Gregory, Dan Frank, Xin Ye, Katie Baker, and Ivan Lenov for all of their major and minor help, for fun ski trips, and for their companionship.

I have had the opportunity to work with a number of wonderful collaborators, many of whom contributed directly to the work in this dissertation. I thank Hao Zhang, Weidong Cui, Prof. Robert Blankenship, and Prof. Michael Gross at Washington University in St. Louis for their spectacular work on native mass spectrometry of Nanodiscs. Working with them was very educational, exciting, and rewarding. I will miss visiting them in St. Louis.

Thanks to Prof. Ryan Bailey and Courtney Sloan at the University of Illinois Urbana-Champaign for their excellent work on the microring resonator biosensors. Both have inspired me with their success as professor and postdoc respectively. I thank Prof. Bill Klein and Kyle Wilcox at Northwestern University for their contributions to the SMPL project. Finally, thanks to

Kevin Tucker at the UIUC Mass Spectrometry Facility as well as Peter Yau at the UIUC Protein Sciences Facility for performing and supporting crucial experiments.

Although their work was not directly mentioned in this dissertation, thanks to Prof. Emad Tajkhorshid and Josh Vermaas at UIUC for molecular dynamics simulations of gas-phase Nanodiscs. Also, thanks to Prof. Martin Jarrold, David Keifer, and Lizz Pierson at Indiana University for very interesting charge detection mass spectrometry.

Much of my interest in chemistry is due to influential teachers in high school and undergraduate studies. Phil Deist gave me a solid foundation in the fundamentals of chemistry and physics. Prof. Doug Beussman at St. Olaf College got me excited about analytical chemistry and mass spectrometry and encouraged me to go to graduate school. Prof. Gary Miessler, also at St. Olaf College, taught me how to research and communicate science. Rich Engler at the Environmental Protection Agency showed how chemistry could make a difference in the world. I thank all of my former teachers, named and unnamed, as well as my classmates, especially in the Analytical Chemistry program at UIUC, for shaping me as a scientist.

My graduate education was funded by the Robert C. and Carolyn J. Springborn Endowment. I thank the Springborns for their generous support and this amazing opportunity to pursue new scientific directions.

Finally, I thank my family for their love and support. My parents provided encouragement, perspective, and countless meals over the last few years. My grandparents have been scholarly role models who have inspired my academic pursuits. Finally, my wonderful wife has been with me every step of the way. From editing my graduate school applications (and numerous other documents) to deciding where to go next, she has been my constant companion and my greatest asset. Claire, I dedicate this work to you.

TABLE OF CONTENTS

ABBREVIATIONS vi

CHAPTER 1: INTRODUCTION 1

CHAPTER 2: CHARACTERIZATION OF NANODISCS BY NATIVE MASS SPECTROMETRY 17

CHAPTER 3: DEVELOPMENT AND CHARACTERIZATION OF *E. COLI* NANODISC-SOLUBILIZED MEMBRANE PROTEIN LIBRARY 46

CHAPTER 4: ULTRA-THIN LAYER MALDI MASS SPECTROMETRY OF MEMBRANE PROTEINS IN NANODISCS 62

CHAPTER 5: INTERFACING NANODISCS WITH SILICON PHOTONIC MICRORING RESONATORS 79

CHAPTER 6: NONLINEAR CONCENTRATION GRADIENTS FOR KINETIC EXPERIMENTS EMPLOYING MICRORING RESONATORS 91

CHAPTER 7: CONCLUSIONS AND FUTURE DIRECTIONS 120

REFERENCES 124

ABBREVIATIONS

4HCCA	4-Hydroxy-α-cyano-cinnamic Acid
ApoAI	Apolipoprotein A-I
AβO	Amyloid β Oligomer
BCA	Bicinchoninic Acid
BSA	Bovine Serum Albumin
CPR	Cytochrome P450 Reductase
CTB	Cholera Toxin Subunit B
CYP3A4	Cytochrome P450 3A4
DMPC	1,2-Dimyristoyl-*sn*-glycero-3-phosphocholine
DPPC	1,2-Dipalmitoyl-*sn*-glycero-3-phosphocholine
DPPE	1,2-Dipalmitoyl-*sn*-glycero-3-phosphoethanolamine
E. Coli	*Escherichia Coli*
EDTA	Ethylenediaminetetraacetic Acid
FTICR	Fourier Transform Ion Cyclotron Resonance
FWI	Formic Acid/Water/Isopropanol
HDL	High-density Lipoprotein
HPLC	High Performance Liquid Chromatography
HXMS	Hydrogen Exchange Mass Spectrometry
ISCAD	In-source Collisionally Activated Dissociation
IRMPD	Infrared Multiphoton Dissociation
LC-MS/MS	Liquid Chromatography – Tandem Mass Spectrometry
MALDI	Matrix Assisted Laser Desorption Ionization

MP	Membrane Protein
MS	Mass Spectrometry
MSP	Membrane Scaffold Protein
Ni-NTA	Nickel-nitrilotriacetic Acid
OG	Octyl-β-glucoside
PBS	Phosphate-buffered Saline
PBST	Phosphate-buffered Saline with Tween
POPC	1-Palmitoyl-2-oleoyl-*sn*-glycero-3-phosphocholine
POPS	1-Palmitoyl-2-oleoyl-*sn*-glycero-3-[phospho-L-serine]
PSA	Prostate Specific Antigen
rHDL	Reconstituted High Density Lipoprotein
Rho	Rhodopsin
SA	Sinapinic Acid
SAMDI	Self-assembled Monolayer Desorption Ionization
SDS	Sodium Dodecyl Sulfate
SDS-PAGE	Sodium Dodecyl Sulfate – Polyacrylamide Gel Electrophoresis
SEC	Size Exclusion Chromatography
SMPL	Soluble Membrane Protein Library
SPR	Surface Plasmon Resonance
TFA	Trifluoroacetic Acid
TWA	Trifluoroacetic Acid/Water/Acetonitrile

CHAPTER 1: INTRODUCTION

1.1 Challenges in Analysis of Membrane Systems

Lipid membranes play a crucial role in biology. Membranes serve as physical barriers to separate the cell from its environment and to define compartments within the cell. Proteins localized to lipid membranes, termed membrane proteins, perform a variety of biological functions including signaling, transport, catalysis, and energy conversion. Proteins interact with the membrane in a number of ways, ranging from integral membrane proteins buried within the hydrophobic lipid bilayer to peripheral membrane proteins that are water-soluble and interact with the hydrophilic membrane surface. The lipid membrane is more than a physical barrier or architectural scaffold. It is a dynamic environment that participates in modulating and regulating cellular biochemistry.

It is estimated that membrane proteins account for around 20-30% of the proteome in most organisms[1] and over half of all drug targets.[2] Despite their biological and pharmaceutical importance, membrane proteins have proven challenging to interrogate with biochemical and analytical methods for three primary reasons: low abundance, aggregation, and environmental sensitivity.

First, it is challenging to get large amounts of membrane proteins. Membrane proteins generally have low natural copy numbers, and their recombinant over-expression is difficult.[3,4] Thus, membrane protein analysis is often limited by the amount of material available. The low abundance of membrane proteins requires sensitive analytical methods that consume small amounts of material.

Second, membrane proteins often have poor solubility in aqueous buffers typically required for analysis. Because they are evolved with hydrophobic regions to match the membrane environment, membrane proteins tend to form ill-defined aggregates in solution. The membrane itself is insoluble and not suited for many analysis techniques. Analysis of membrane proteins generally requires a means for solubilization and stabilization.

Finally, the membrane environment has important effects on protein structure and function.[5,6] The bilayer thickness, charge, and specific lipid composition may all modulate membrane protein activity.[5-7] However, protein-lipid interactions are difficult to study, and many solubilization strategies fail to model the native lipid environment. These three challenges, low abundance, aggregation, and environmental sensitivity, have led to a deficit in understanding of membrane proteins compared to soluble proteins.

1.2 Strategies for Membrane Protein Solubilization

1.2.1 Detergents and Amphipols

The most common solubilization strategy employed for membrane protein analysis is the use of amphipathic detergents to extract membrane proteins into soluble micelles. A multitude of detergent molecules exist, and they are divided into classes based on their charge: nonionic, anionic, cationic, or zwitterionic. Detergents are essential tools for working with membrane proteins and can be very effective at solubilizing and extracting proteins from the membrane. Special care must be taken to ensure that detergents do not denature the proteins or otherwise disrupt their native structure and function. Although certain classes, particularly nonionic, are generally regarded as non-denaturing, there is no ideal detergent that works universally in all systems.[8-12]

A related strategy for membrane protein solubilization is the use of amphipathic polymers, also known as amphipols. Amphipols are heteropolymers containing both hydrophobic and hydrophilic monomer units. They are synthesized as a polydisperse mixture of species. Unlike detergents, which must be maintained at relatively high concentrations to form micelles, amphipols bind membrane proteins tightly and do not require large excesses of free polymers. Amphipols have been shown to effectively solubilize membrane proteins while preserving their activity.[13,14]

The chief concern in using detergent micelles and amphipols to solubilize membrane proteins is that they are not true lipid bilayers and thus may not capture the native form of the protein. Both are fairly heterogeneous and do not necessarily model the lipid bilayer environment effectively. Although they address the solubility challenge, detergents and amphipols can be problematic for analysis of membrane proteins when the bilayer environment is key to their structure and function.

1.2.2 Liposomes and Bicelles

To provide a more native-like environment, lipid bilayer preparations such as liposomes or bicelles are employed to solubilize membrane proteins. Liposomes are lipid vesicles that may contain one or more lipid species. Membrane proteins are incorporated into liposomes by adding detergent-solubilized membrane proteins and removing the detergent by dialysis or hydrophobic beads to yield proteoliposomes.[15] Liposomes are particularly useful in studying transporters and channels as the interior of the liposome forms a distinct compartment separate from the bulk solution. However, the large size, polydispersity, and heterogeneity of liposome preparations make them unsuitable for some analysis techniques.

A related preparation, known as a bicelle, utilizes two lipid species to form nanoscale discoidal lipid bilayer segments. A long or medium chain lipid forms a bilayer. A short chain lipid or detergent forms curved caps at the edge of the bicelle to shield the hydrophobic interior. There are several strategies for inserting membrane proteins into bicelles, and different sized bicelle preparations are accessible. Because they are generally smaller than liposomes, bicelles are a popular membrane mimetic for use in nuclear magnetic resonance studies (NMR).[16-18] Additionally, bicelles are becoming more widely used in crystallization of membrane proteins for x-ray crystallography.[19,20]

1.2.3 Lipoproteins

Whereas bicelles terminate the bilayer with a curved segment of short chain lipids or detergents, it is possible to terminate the bilayer with an amphipathic alpha-helical protein to form a lipoprotein particle. Lipoproteins are combinations of lipids and amphipathic proteins that naturally exist in several structural forms. Nascent high-density lipoprotein (HDL) particles form discoidal structures similar to bicelles but with a protein belt. Discoidal HDL can be self-assembled by combining apolipoprotein A-I (ApoAI) with detergent solubilized phospholipids.[21,22] Removal of the detergent drives self-assembly of reconstituted HDL (rHDL) nanoscale lipid bilayers. If a membrane protein is introduced in the self-assembly process, the membrane protein may be incorporated into the rHDL bilayer.[23-25] In addition to ApoAI, other engineered or natural apolipoproteins form similar nanoscale lipid bilayers, sometimes referred to as nanolipoprotein particles.[21,22,24,26] The most widely used construct is a class of proteins known as membrane scaffold proteins (MSP) to form particles known as Nanodiscs.[27,28]

1.3 Nanodiscs – Well-defined Engineered Lipoproteins

1.3.1 Development and Characteristics of Nanodiscs

Nanodiscs are nanoscale discoidal lipid bilayers encircled by two membrane scaffold proteins. The original membrane scaffold protein, MSP1, was derived from ApoAI, truncated to remove the globular N-terminal domain, and engineered for expression in *Escherichia Coli* (*E. Coli*). Similar to other lipid reconstitution systems, Nanodiscs are self-assembled by removing detergent from a mixture of cholate-solubilized phospholipids and MSP.

Characterization of Nanodiscs by atomic force microscopy and size exclusion chromatography revealed they are discoidal in shape with a diameter of 10 nm and a thickness of 5-6 nm.[27] Titration of lipids provided the optimal protein to lipid ratios for self-assembly of monodisperse and homogeneous Nanodiscs. Further engineering of MSP proteins showed that the first 11 residues of MSP1 do not interact with the bilayer. Deletion of these 11 residues and addition of a tobacco etch virus (TEV) protease cleavable polyhistidine tag yielded MSP1D1. MSP1D1 interacts with the bilayer through eight amphipathic helices. Addition of extra copies of a 22 amino acid helix extended the MSP length to form larger Nanodiscs with diameters up to 12 nm.[28] By fusing two MSP sequences together, even larger particles were engineered with diameters ranging from 16 to 17 nm.[29] Due to its high expression yields and consistency in Nanodisc formation, MSP1D1 is the most widely used MSP variant.

Similar to rHDL, inclusion of detergent-solubilized membrane proteins during the self-assembly process leads to incorporation of membrane proteins into the Nanodisc lipid bilayer.[30-32] Nanodiscs offer several potential advantages over other membrane mimetic technologies. The next section outlines seven advantages of Nanodiscs with examples of how each advantage has been utilized for biochemical applications.

1.3.2 Advantages of Nanodiscs

First, although detergents are required for assembly of Nanodiscs, they are removed during the self-assembly process. Nanodiscs offer a soluble yet detergent-free environment for membrane proteins that avoids many of the deleterious effects of detergents. For example, some detergents alter the binding of substrates to membrane-bound cytochrome P450 3A4 (CYP3A4). Nanodiscs offer a platform for studying CYP3A4 without the interfering effects of detergents.[30]

Second, Nanodiscs provide a native-like lipid bilayer, which reflects the physiological environment of membrane proteins more closely than detergent micelles. Epidermal growth factor receptor, a receptor tyrosine kinase, demonstrated significantly better stability in Nanodiscs compared to detergent micelles.[33] Improved stability of membrane proteins is an important potential advantage of lipid bilayer Nanodiscs over detergent micelles.

Third, the lipid content of the Nanodisc bilayer can be precisely defined to investigate protein-lipid interactions and to probe how lipids modulate membrane protein biochemistry. For example, Nanodiscs were used to observe the influence of the lipid membrane environment on redox potentials of membrane-embedded cytochromes P450.[7] Additionally, Nanodiscs have been used to demonstrate that the phospholipid bilayer composition can modulate the interaction of G proteins with G protein-coupled receptors (GPCR).[34]

Fourth, adjusting the ratio of membrane protein to MSP in the Nanodisc self-assembly process gives control of membrane protein stoichiometry. Unlike the native membranes or liposomes, Nanodiscs offer the ability to isolate specific oligomeric states. By controlling the stoichiometry, Nanodiscs can be used to study the effect of oligomerization on membrane protein function. This advantage has been exploited to determine the effect of various oligomerization states on rhodopsin activity.[35]

Fifth, membrane scaffold proteins can be modified with a variety of tags to allow easy interfacing with sensing and capture technologies. Tagging of the MSP circumvents the need for modifying, thus potentially disrupting, the membrane protein target. There are several ways to tag MSP. Polyhistidine, FLAG, and other genetically programmed tags can be engineered into the MSP sequence and expressed on the protein itself. These modifications are generally added to the ends of the MSP sequence and thus do not interfere with the bilayer interactions. Additionally, MSP mutants containing a single cysteine residue can be chemically modified with a variety of cysteine specific labels. The wide range of tagging strategies allows Nanodiscs to be easily tailored for different systems and analysis techniques. For example, Borch *et al.* examined a variety of strategies for attaching Nanodiscs to surface plasmon resonance (SPR) surfaces when conventional nickel-nitrilotriacetic acid (Ni-NTA) attachment was not suitable.[36]

Sixth, Nanodiscs allow access to both sides of the membrane protein. This is important for studying membrane proteins such as integrins where binding on one side of the membrane induces binding on the opposite side.[37] In liposomes, this type of interaction would be very difficult to study due to physical separation of the solution on each side of the membrane. However, access to both sides of the membrane may be a disadvantage in the study of transporters or channels, where liposomes would be more appropriate.

Finally, Nanodiscs are the most monodisperse of the membrane mimetics outlined above. Thus, each membrane protein in Nanodiscs experiences the same environment. Monodispersity is important for applications of Nanodiscs in electron microscopy where images of individual complexes are stitched together *in silico* to form a composite structure[38-40] and for small angle x-ray scattering experiments that rely on molecular modeling for data interpretation.[30,41] A detailed discussion of Nanodisc polydispersity is provided in Chapter 2.

1.4 Bioanalytical Applications of the Nanodisc Platform

Nanodiscs have been used to study membrane systems with a wide range of analytical techniques. Hydrodynamic methods including size exclusion chromatography,[27] free flow electrophoresis,[42] and ultracentrifugation[43-45] were used to characterize and purify Nanodiscs. Thermal methods such as differential scanning calorimetry were used to probe lipid bilayer phase changes.[46,47] Because of their small size, Nanodiscs have very low scattering and are ideally suited for spectroscopic studies. Optical,[30-32,48,49] fluorescence,[35,46,47,50,51] and Raman[52,53] spectroscopy were applied to Nanodiscs to study membrane protein structure and function. Nanodiscs may also be used for electrochemical studies[7,54] of membrane proteins. Due to their particular importance to this dissertation, applications of Nanodiscs to surface-based biosensors, mass spectrometry, and interactomics are discussed extensively in Sections 1.4.1, 1.4.2, and 1.4.3 respectively.

Although they have proven elusive to x-ray crystallography, Nanodiscs are emerging as a vital tool for other structural biology techniques. Imaging methods including electron microscopy[37-40,55,56] and atomic force microscopy[27,32] have provided low-resolution structures of membrane proteins in Nanodiscs as well as information on membrane topology. Small angle x-ray and neutron scattering have been used to characterize Nanodisc structure and study Nanodisc-solubilized membrane proteins.[28,30,31,41,46,57-59] Nanodiscs have also been applied to NMR for a range of studies including high-resolution structures.[60-69]

1.4.1 Biosensors

Due to their sensitivity, temporal resolution, and minimal need for labeling, biosensors are widely used to characterize and detect biomolecular interactions. Surface-based biosensors operate on the principle of detecting local changes at the biosensor surface, typically refractive

index, as a biomolecule in solution binds to a partner that is attached to the surface. A central challenge in developing biosensor assays is tethering one of the binding partners to the sensor. Previous methods to study membrane systems on biosensors have utilized many of the same membrane mimetic strategies outlined above.[70] However, detergent-solubilized membrane proteins are limited by the need for a constant concentration of detergent, which may interfere with biomolecular interactions. Liposomes and supported lipid bilayers are limited by heterogeneity, access to only one side of the membrane, and the inability to control oligomerization state of membrane proteins.

Nanodiscs are an ideal platform for interfacing membrane systems with surface-based biosensors. One particular advantage of Nanodiscs is that they may be attached to the surface through tags on the MSP, leaving membrane proteins within the Nanodisc unperturbed. Thus, interactions between membrane proteins or lipids and their binding partners may be probed without labels on either species. Nanodiscs have been applied to several biosensor platforms with various strategies for interfacing Nanodiscs to the surface.

Surface plasmon resonance (SPR) experiments utilized Nanodiscs to detect binding of soluble peripheral membrane proteins to lipid ligands. Nanodiscs were affixed to the surface using polyhistidine tags on the MSP and a nickel-chelating sensor surface to study the binding of clotting factors to Nanodiscs with varying levels of 1-palmitoyl-2-oleoyl-*sn*-glycero-3-[phospho-L-serine] (POPS).[71] Another report measured the binding of cholera toxin B (CTB) subunit to ganglioside glycolipid GM1 in Nanodiscs. Because CTB also binds to nickel-chelating surfaces, alternative immobilization strategies were employed including a polyhistidine specific antibody and a FLAG/anti-FLAG system.[36] It was also shown that Nanodiscs may be used as the soluble analyte to bind with an immobilized partner on the surface.[72]

Beyond SPR, Nanodiscs have been covalently coupled to resonant localized surface plasmon resonance nanoparticles to detect binding of small molecules to cytochromes P450.[73] Covalent coupling was also used to detect binding of CTB to GM1 Nanodiscs using microcantilevers.[74] Finally, Nanodiscs were patterned in a microfluidic device using biotinylated lipids and covalently bound streptavidin. Binding of fluorescent annexin V to Nanodiscs containing varying levels of POPS was quantitated by fluorescence microscopy.[75] These experiments demonstrate a range of biosensor technologies amenable to Nanodiscs and the potential for parallel detection of interactions at the membrane surface.

1.4.2 Mass Spectrometry

Mass spectrometry is a powerful analytical technique that is applied in a number of ways to study biological systems. Mass spectrometry analysis of proteins can be divided into three paradigms based on which structural elements are conserved. Native mass spectrometry preserves tertiary and quaternary structure of noncovalent complexes. Conventional mass analysis measures the mass of covalently intact but denatured proteins. Primary structure is preserved, but higher structure is lost. Finally, mass analysis of peptide fragments, often called bottom-up proteomics, preserves segments of primary structure but fragments the complete primary structure. Nanodiscs have been studied with all of these mass spectrometry techniques.

By measuring the mass of noncovalent complexes, native mass spectrometry provides information on the composition, stoichiometry, and interactions of subunits in complexes. Although native mass spectrometry of Nanodiscs is still in its infancy (see Chapter 2), it has been used to study the interaction of soluble proteins with lipid ligands. Pentameric cholera toxin B was combined with Nanodiscs containing GM1 glycolipid. The CTB-Nanodisc complex was not resolved, but fragmentation of the complex yielded CTB pentamer bound to GM1 molecules.

With a low loading percentage of GM1, CTB was observed with zero or one GM1 molecule bound. At higher loading ratios, four and five molecules of GM1 were bound to the five binding sites on the CTB pentamer.[76] This study demonstrated the unique potential of coupling native mass spectrometry with Nanodiscs to study stoichiometry of protein-lipid interactions.

The first reported use of mass spectrometry with the Nanodisc platform was in an innovative assay of G protein-coupled receptor activation that detected full protein masses. Here, Nanodiscs containing rhodopsin were attached to a self-assembled monolayer (SAM) on a gold substrate. Activation of rhodopsin by light shined on the surface caused the binding of transducin. Transducin was detected directly on the SAM surface using a special form of matrix-assisted laser desorption ionization (MALDI) know as self-assembled monolayer desorption ionization (SAMDI) mass spectrometry. Weak peaks from the Nanodisc-embedded rhodopsin were also observed and served to verify that the Nanodiscs were attached to the surface. This study demonstrated that mass spectrometric detection of full proteins could be utilized as an effective bioassay.[77]

Two studies from John Engen and coworkers used hydrogen-deuterium exchange mass spectrometry (HXMS) to study Nanodiscs and membrane proteins embedded in Nanodiscs.[78,79] HXMS provides low-resolution structural information on solvent accessibility and protein dynamics by monitoring the exchange of deuterium from deuterium oxide buffer with hydrogen atoms on the protein backbone. Bottom-up proteomic methods are used to quantitate the deuterium uptake of peptide fragments. HXMS of Nanodiscs presents several technical challenges in sample preparation. Because hydrogen-deuterium exchange is reversible, the reaction must be quenched with low temperature and low pH. Subsequent sample preparation must be done quickly and at these extreme sample conditions to avoid reverse exchange.

Two central challenges in mass spectrometric analysis of Nanodiscs are the relative abundance of lipids and MSP over membrane proteins. For each monomeric membrane protein, the Nanodisc contains two MSP molecules and dozens of lipids. Engen and coworkers found that lipids did not interfere with HXMS sample preparation and analysis but led to deterioration of the ultra performance liquid chromatography (UPLC) column used to separate peptide digests for mass spectrometry. They removed lipids from the system by disassembling Nanodiscs with cholate and adsorbing phospholipids on zirconia beads. Addition of cholate also improved the efficiency of protease digestion. Following digestion, peptides were analyzed with liquid chromatography-mass spectrometry (LC-MS) using a UPLC separation optimized for rapid analysis of amphipathic membrane protein peptides. Control samples from empty Nanodiscs allowed discrimination of MSP peptides from Nanodisc-embedded gamma-glutamyl carboxylase (GGCX). Although this report did not perform a detailed interpretation of results from GGCX, HXMS methods will facilitate future Nanodisc studies probing membrane protein topology and dynamics.[78]

Another study from Engen and coworkers utilized HXMS to study MSP and probe conformational dynamics of Nanodiscs. Gross conformational changes were observed between free MSP and MSP associated with Nanodiscs. The presence of EX1 or cooperative unfolding kinetics for deuteration of MSP in Nanodiscs suggests that regions of MSP near the N-terminus are disordered and dynamic.[79] This study revealed interesting conformational mobility in the MSP belt and established an understanding of the HXMS behavior of MSP, which will aid future HXMS studies of membrane proteins in Nanodiscs.

1.4.3 Interactomics

Another use of mass spectrometry-based bottom-up proteomic techniques is in the identification of protein interaction partners, known as interactomics. One type of interactomic experiment, known as a co-immunoprecipitation, relies on a "bait" molecule that can be immunocaptured for easy separation. A pool of "prey" molecules is allowed to interact with the bait before the bait and any bound proteins are removed. Prey that remains bound to the bait is identified with proteomics to reveal interaction partners of the bait molecule. Nanodiscs present a unique platform for interactomics assays involving membrane proteins and lipids.

The first interactomic study to employ Nanodiscs used glycolipid GM1 Nanodiscs as the bait and cell-culture extract from enterotoxigenic *E. Coli*. Co-immunoprecipitation isolated and identified heat labile toxin, a homolog of CTB, bound to GM1 in Nanodiscs.[80] This study demonstrated the potential of Nanodisc interactomics experiments to reveal soluble binding partners for lipid ligands.

Another study extended the use of interactomics to study membrane proteins in Nanodiscs.[81] Here, Nanodiscs were assembled with one of three proteins, SecYEG, MalFGK, or YidC. *E. Coli* cell cultures were grown in minimal media with either normal or stable isotope labeled amino acids to form a "light" proteome and a stable isotope labeled "heavy" proteome. This technique, known as stabile isotope labeled amino acids in cell culture (SILAC) provides a control for nonspecific binding. The light proteome was incubated with empty Nanodiscs that did not contain a membrane protein. The heavy proteome was incubated with Nanodiscs containing one of the membrane protein baits. Nanodiscs in both samples were isolated using the polyhistidine tag on the MSP and were pooled. Nonspecific interactions showed an equal

distribution of light and heavy isotopes while specific interactions were enriched in the heavy isotopes.

Using this SILAC experiment, a number of interaction partners were identified for all three proteins, but quantitative analysis of enrichment ratio revealed that only a few strongly interacting partners were present for SecYEG and MalFGK. Interestingly, SecYEG Nanodiscs formed with *E. Coli* total lipids were most enriched with Syd while SecYEG Nanodiscs assembled with phosphatidylglycerol were most enriched with SecA. This difference demonstrated the importance of anionic lipids in the interaction between SecA and SecYEG.[81] This SILAC experiment along with other interactomics studies performed in rHDL systems[82] demonstrates the unique capability of Nanodiscs to identify new interactions between soluble and membrane-bound proteins.

1.5 Dissertation Overview

This dissertation leverages the opportunities of the Nanodisc platform to develop novel bioanalytical techniques to study membrane systems. These bioanalytical techniques extend the capabilities of mass spectrometry and biosensors for Nanodisc systems. Special focus is given to the development and analysis of heterogeneous libraries of membrane proteins in Nanodiscs.

Chapter 2 describes the characterization of Nanodiscs by native mass spectrometry. Previous studies described above failed to resolve Nanodiscs in the gas phase.[76] Here, intact Nanodiscs were detected with single lipid resolution.[83] This analysis provided the first molecular characterization of Nanodisc polydispersity and demonstrated the robustness of Nanodiscs. The fundamental behavior of Nanodiscs in the gas phase is explored using various fragmentation methods and theoretical investigation. In addition to providing a fundamental characterization of

Nanodiscs, these experiments lay the foundation for native mass spectrometry studies of membrane proteins in Nanodiscs.

Chapter 3 details the development and characterization of Nanodisc-solubilized membrane protein libraries.[84] Previous interactomics studies with Nanodiscs used homogeneous purified membrane protein bait with a pool of soluble protein prey.[81] This experiment can be inverted to detect interactions between purified soluble protein bait and a heterogeneous Nanodisc-solubilized membrane protein library (SMPL) prey. Chapter 3 develops the SMPL approach and characterizes libraries formed from *E. Coli* membranes.

Chapter 4 details improved sample preparation techniques for MALDI mass spectrometry analysis of membrane proteins in Nanodiscs.[85] As demonstrated in the SAMDI assay described in Section 1.4.2,[77] mass spectrometric detection of proteins holds the potential for unique bioassays, but MALDI analysis of Nanodiscs is complicated by excesses of lipids and MSP. The ultra-thin layer sample preparation method removes the MSP signal while enhancing signal from membrane proteins inside the Nanodisc. The method is effective with a range of membrane proteins and can identify components from a known mixture of membrane protein Nanodiscs.

Chapter 5 discusses the interfacing of Nanodiscs with multiplexed silicon photonic microring resonator biosensors.[86] A novel strategy was used to attach Nanodiscs to the surface via direct physisorption on the silica biosensors. After correcting for differences in loading, the strategy can be used to quantitate the binding of soluble proteins to Nanodiscs with different lipid compositions. Moreover, the multiplex capabilities of the microring resonator technology were employed to develop a four-plexed assay with different Nanodisc species adsorbed on specific regions of the sensor surface.

Chapter 6 extends the capabilities of the microring resonator platform to single-run kinetic assays using nonlinear analyte gradients.[87] Conventional kinetic assays consume more time and materials, as the assay must be repeated at multiple concentration steps. Analyte gradients allow a full kinetic experiment to be performed in a single run by continuously sweeping the analyte concentration through a relevant range. Chapter 6 describes the development and testing of a nonlinear analyte gradient generator, theoretical validation of the analyte gradient approach, and application of the technique to measure the binding kinetics of prostate specific antigen (PSA) with an anti-PSA antibody.

Chapter 7 provides a concluding discussion of topics outlined in this dissertation and offers a perspective on future directions for the use of Nanodiscs, mass spectrometry, biosensors, and Nanodiscs libraries for the study of membrane systems.

CHAPTER 2: CHARACTERIZATION OF NANODISCS BY NATIVE MASS SPECTROMETRY

2.1 Introduction

Native mass spectrometry (MS), which seeks to preserve solution phase structure and noncovalent interactions, has emerged as a powerful technique to study membrane systems due to its low sample requirements and unique structural information on complex structure and lipid binding.[6,88-92] Nanodiscs offer a promising technology for native mass spectrometry of membrane systems due to their monodispersity, homogeneity, and native-like lipid bilayer.[76]

This chapter presents the first evidence that intact Nanodisc complexes can be introduced into the gas phase of a mass spectrometer using native electrospray MS for direct measurement of their molecular weight and polydispersity.[83] Native mass spectra of Nanodiscs are characterized by broad distributions of narrow peaks (see Figure 2.1 for example). The initial interpretation was that broader distributions arose from two components, the lipid count distribution and charge state distribution. Each narrow peak was due to Nanodiscs with a defined lipid count. Each broader peak was assumed to result from the lipid count distribution at a single charge state. Because the charge state can be determined from the difference between narrow peaks, fitting the broad peaks to Gaussian distributions yielded the mean and standard deviation of the lipid count.

Reproduced in part with permission from Marty, M. T.; Zhang, H.; Cui, W.; Blankenship, R. E.; Gross, M. L.; Sligar, S. G. Native mass spectrometry characterization of intact nanodisc lipoprotein complexes. *Anal. Chem.* **2012**, *84*, 8957-8960. The published version may be found online at http://pubs.acs.org/doi/abs/10.1021/ac302663f. Copyright 2012 American Chemical Society. Contributions of figures and data from Hao Zhang and Weidong Cui are gratefully acknowledged.

However, subsequent measurements and theoretical exploration revealed an additional factor contributing to the broad distributions. In addition to the lipid count and charge state distributions, the constructive overlap of adjacent charge states plays a dominant role in shaping the spectra. Overlap occurs specifically at m/z values near integer multiples of the lipid mass. Constructive overlap complicates peak assignments and requires more sophisticated deconvolution of the underlying mass and charge distributions.

This chapter presents both the initial two-component model and the improved three-component model for interpreting Nanodisc native mass spectra along with a probability-based algorithm for deconvolution. The deconvolution algorithm is applied to a series of native mass spectra from 1,2-dimyristoyl-*sn*-glycero-3-phosphocholine (DMPC) Nanodiscs at various fragmentation energies. The theory and algorithms described herein will aid in future studies of Nanodisc complexes containing more complex lipid and membrane protein systems.

2.2 Experimental Methods

2.2.1 Materials

1,2-Dimyristoyl-*sn*-glycero-3-phosphocholine (DMPC) and 1-palmitoyl-2-oleoyl-*sn*-glycero-3-phosphocholine (POPC) were purchased from Avanti Polar Lipids (Alabaster, AL). Sodium cholate, Amberlite XAD-2 beads, and ammonium acetate were purchased from Sigma-Aldrich (St. Louis, MO).

2.2.2 Nanodisc Self-Assembly

Nanodiscs were prepared using membrane scaffold protein (MSP) variant MSP1D1(-), which is a version of MSP1D1 with the polyhistidine tag removed. Expression and purification of MSP1D1(-) have been described previously.[27,28] MSP was prepared at a concentration around

150 μM. POPC and DMPC lipids were dissolved in chloroform, dried under nitrogen, and placed in a vacuum desiccator overnight to remove any residual chloroform. Dried lipids were resuspended in 0.1 M sodium cholate to a final lipid concentration of 50 mM. Nanodisc reconstitution mixture was made by combining MSP, lipids, and cholate in a molar ratio of 170:85:1 cholate:DMPC:MSP or 140:70:1 cholate:POPC:MSP. The reconstitution mixture was incubated for an hour at 25°C for DMPC and 4°C for POPC. To initiate the self-assembly process, detergent was removed by adding 0.5-0.8 g of Amberlite XAD-2 beads for each milliliter of solution and incubating overnight at the same temperatures as the previous incubation. Amberlite beads were removed, and the mixture was purified on a Superdex HR 200 10/30 size exclusion column (Amersham-Pharmacia Biotech, Piscataway, NJ) with an elution buffer of 0.1 M ammonium acetate at pH=6.8. Only the middle fractions of the Nanodisc peak were collected and pooled. Final concentrations measured between 5 and 15 μM.

2.2.3 Fourier Transform Ion Cyclotron Resonance Mass Spectrometry

Nanodisc samples were ionized by offline nano-electrospray ionization with PicoTip capillary needles (tip inner diameter 2 μm, capillary outer diameter/inner diameter 1.0/0.58 mm, New Objective) at a flow rate of 20-80 nL/min. Mass spectra were acquired with a Bruker Solarix 12 T Fourier transform ion cyclotron resonance (FTICR) mass spectrometer, utilizing a capillary voltage of 0.9-1.3 kV, a drying-gas temperature of 30°C, and a gas flow of 2.5 L/min. The voltage for in-source collisionally activated dissociation (ISCAD) varied from 10 to 190 V. The RF amplitude of the ion funnels were 320 V, and their voltages were 200 V (funnel 1) and 10 V (funnel 2). RF frequencies in all ion-transmission regions were the lowest available: multipole 1 (2 MHz), quadrupole (1.4 MHz), and transfer line (1 MHz). Ions were accumulated for 500 ms in the RF-hexapole ion trap before being transmitted to the ICR trap. The pressures

were ~2.3 mbar (source), 4×10^{-6} mbar (quadrupole), and 1×10^{-9} mbar (trap). The typical electron capture dissociation (ECD) pulse length was 0.01 – 0.03 seconds with an ECD bias of 0.1 – 0.3 V, an ECD lens voltage of 10 V, and a hollow cathode heater current of 1.6 A. Infrared multiphoton dissociation (IRMPD) was accomplished using a 10.6 μm CO_2 laser (SYNRAD 48-2KAL, Mukilteo, WA) at 25% full power (32 Watts) varying the laser pulse duration from 0.1 to 1.5 seconds. Hundreds to a few thousand scans were averaged for each spectrum with 32k (lower resolution) or 128k (higher resolution) data size. External calibration was done by using cesium perfluoroheptanoic acetate up to *m/z* 8500.

2.3 Results and Discussion

2.3.1 Two-Component Model of Nanodisc Native Mass Spectra

The native mass spectra for DMPC and POPC Nanodiscs as measured by FTICR mass spectrometry at lower resolution show a fine spacing within each broad peak (Figures 2.1 and 2.2 respectively with additional spectra shown in Figures 2.3 and 2.4). This spacing is due to slight differences in lipid packing, with each peak representing a Nanodisc ion with a defined number of lipids. Adjacent narrow peaks differ by the mass of a single lipid, so the charge for each species can be determined by dividing the mass of the lipid by the spacing between adjacent peaks. The three broad peaks seem to correspond to the +22, +21, and +20 charge states and were fit to three overlapping Gaussian distributions to calculate the average molecular weight and polydispersity (Figures 2.5 and 2.6). The mean and standard deviations of the three distributions were averaged, and errors are reported as one standard deviation.

Fitting FTICR mass spectra to Gaussian distributions (Figure 2.5) shows DMPC Nanodiscs with an average mass of 149.5 ± 0.5 kDa at 70 V ISCAD. Because charge is roughly proportional to the square root of mass,[93] some deviation in average mass between the charge

states is expected. DMPC Nanodiscs thus average 155 lipids per Nanodisc or 77.5 lipids per leaflet. This lipid count agrees well with the 77 lipids per leaflet, previously measured for DMPC by radioactive methods.[94] The average lipid count has a standard deviation of 2.4 ± 0.5 lipids.

The results for POPC Nanodiscs (Figure 2.6) yield an average mass of 151.7 ± 0.3 kDa at 70 V ISCAD. There are on average 141 POPC lipids per Nanodisc or 70.5 lipids per leaflet. This is in acceptable agreement with lipid counts for POPC Nanodiscs, which were reported to be 62 lipids per leaflet and 67 lipids per leaflet.[27,71,94] Similar to DMPC, the POPC lipid distribution is 2.61 ± 0.02 lipids.

Informed by the charges determined from lipid spacing, a simple formula was used to calculate the expected native mass-to-charge ratio of a Nanodisc, m/z_{ND}, as a function of the number of lipids:

$$m / z_{ND}(n) = \frac{2M_{MSP} + nM_L + 18m + z}{z}$$

where M_{MSP} is the mass of scaffold, 22044 Da; n is the number of lipid molecules; M_L is the average lipid mass, 677.933 Da for DMPC and 760.076 Da for POPC; and z is the charge state. The value of n was simulated for a range around the average lipid number calculated above. The 18m term was included to account for tightly bound solvent molecules or counter-ions such as ammonium (both water and ammonium have molecular weights of 18 Da), which were observed in previous native mass spectrometry studies. This value was determined by adjusting m to achieve minimal difference between the simulated peaks and the middle five peaks in the three distributions. The best fit was found when m was 6 for DMPC and 5 for POPC although the width of the peaks limits the precision of these numbers.

After correcting for bound solvent, simulated masses for the middle five peaks (approximately one standard deviation) in each of the three charge states agreed with measured

peaks to within 0.03% for DMPC and 0.02% for POPC. However, peaks at the edges of the distributions do not match as well owing to the overlapping of distributions from multiple charge states, as seen in Figures 2.1 and 2.2.

The Nanodisc ions remain stable upon ISCAD from 10 to 70 V with a slight decrease in charge state as ISCAD energy increases (see Figures 2.3 and 2.4). Ionization does not occur with large amounts of bound solvent, indicating the instrumental conditions are effective at desolvating the Nanodisc even at low ISCAD energies. Adding additional collisional energy by increasing the accelerating potential to 100 V and 130 V continued to shift the output to lower charge states.

Using the lipid spacing to determine the charge states, it was observed that both 100 V and 130 V ISCAD cause the average lipid count to decrease. This suggests that the Nanodiscs begin to release a small number of lipids without complete destruction. ISCAD at 100 V shows DMPC Nanodiscs with average lipid counts of 153, 148, and 146 (Figure 2.7A). ISCAD at 130 V with an ECD bias of 0.1 V shows DMPC Nanodiscs with average counts of 143 and 139 lipids (Figure 2.7B). These results are consistent with data on detergent complexes; those data demonstrate that lower aggregation numbers are observed at lower charge states.[95] At these higher energies, different charge states and lipid distributions begin to overlap, and the peaks become too difficult to assign based on lipid distribution.

Finally, the mass spectrum of monomeric MSP at charge states from +6 to +12 begins to appear in the low mass region at 130 V, suggesting the complete dissociation of some of the Nanodisc population (Figure 2.8). At 160 V, higher mass peaks largely disappear, leaving only low mass peaks for MSP and lipid clusters. The appearance of bare MSP at high, but not low,

collision energy further confirms the hypothesis that intact Nanodiscs are observed at low to moderate collision energy.

These spectra suggest a comprehensive hypothesis for the behavior of Nanodisc complexes in the gas-phase. At low to moderate ISCAD energies, Nanodisc complexes can be observed with a distribution of lipids. This represents a stable ionization region where the complexes are mostly desolvated but still intact. Increasing the ISCAD voltage begins to strip the complexes of lipids, leaving partially dissociated Nanodiscs. At high energies, the complex is entirely dismantled, leaving only bare MSP and lipid clusters at low *m/z* range.

Although the two-component model is a reasonable explanation for Nanodisc native mass spectra at low collision energies, it begins to break down at higher collision energy. The broader peaks appear at integer multiples of the lipid mass and do not assume a clear charge state distribution. The next section describes an improved model to explain the broad distributions of peaks observed in Nanodisc mass spectra.

2.3.2 Constructive Overlap of Adjacent Charge States

In addition to the intrinsic lipid count and change state distributions, Nanodisc native mass spectra are significantly shaped by the constructive overlap of adjacent charge states. This section mathematically demonstrates that Nanodisc ions with adjacent charge states and differing lipid counts overlap at m/z values close to integer multiples of the lipid mass.

Each Nanodisc contains two molecules of MSP and some number of DMPC lipids. The mass of the MSP1D1(-) construct, M_{MSP}, is 22044 Da. Because each Nanodisc contains two copies of MSP, it is useful to define the mass of the protein component, P, as $P = 2M_{MSP}$. The mass of the DMPC lipid, L, is 678 Da. Adding the protein and lipid components together, the mass of a single Nanodisc complex with k_1 lipids is $P + k_1 L$. This complex is referred to as ion

1. For clarity, the mass of the protons added in the electrospray process is disregarded. The error introduced by the added proton mass is negligible compared to the overall mass.

There is a distribution of lipid count values, so consider a separate Nanodisc complex, ion 2, with k_2 lipids where $k_1 > k_2$. Because k_1 and k_2 are integers, $k_1 - k_2 = n$, where n is also an integer. Assume the first ion has a charge z while the second has a charge of $z - 1$. Using simple arithmetic rearrangement, it can be demonstrated that:

$$\frac{P + k_1 L}{z} = \frac{P + k_2 L}{z - 1} \iff \frac{P + k_1 L}{z} = nL$$

In words, if Nanodiscs of adjacent charge states have the same m/z value, the m/z value is nL, where n is equal to the difference in lipid count and L is the mass of the lipid. The converse of this statement is also true. An analogous argument shows that Nanodisc ions at charge z will overlap with Nanodiscs of charge $z - 2$ at the half integer values, $mL/2$ where $m = 2n + 1$.

In this idealized case, $\frac{P+k_1 L}{z} = nL$ implies that $P = L(zn - k_1)$. Because z, n, and k_1 are all integers, P must be an integer multiple of L, and the entire system simplifies to the principle that $\frac{220L}{22} = \frac{210L}{21} = 10L$. With DMPC and MSP1D1(-), $\frac{P}{L} = 65.03$. Because the mass of the protein component is very close to an integer multiple of the lipid mass, there will be nearly perfect overlap of ions 1 and 2.

However, it is not necessary for P to be an exact integer multiple of L. Consider the case where $P = L(zn - k_1) + \varepsilon = L(zn - n - k_2) + \varepsilon$, where ε is some error such that $\varepsilon < L$. Simple rearrangement shows:

$$\frac{P - \varepsilon + k_1 L}{z} = \frac{P - \varepsilon + k_2 L}{z - 1}$$

$$\frac{P + k_1 L}{z} = \frac{P + k_2 L}{z - 1} + \frac{\varepsilon}{z(z - 1)}$$

The difference between the m/z values of ion 1 and ion 2 is $\frac{\varepsilon}{z(z-1)} < \frac{L}{z(z-1)}$. The error introduced by the protein component is bounded and scales roughly with the inverse square of the charge state. Thus, constructive overlap can occur for any P or L masses.

This model of constructive overlap between adjacent charge states suggests a strategy to minimize the effect. Lowering the charge increases the space between overlapping peaks and also increases the value of n. At high n, the difference in the number of lipids in ions 1 and 2 (recall that $k_1 - k_2 = n$) could be larger than the intrinsic lipid distribution. In other words, the lipid distribution is not wide enough that the adjacent charge state contributes significantly to the peak at nL. An example of this phenomenon is discussed below.

2.3.3 Probability-Based Deconvolution Algorithm

Peak assignment and interpretation of Nanodisc native MS spectra can be complex and must take into account the overlap of adjacent charge states demonstrated in the previous section. A probability-based deconvolution algorithm was developed to deconvolute the overlapping charge states and determine the underlying lipid count and charge distributions of the Nanodisc ions.

The central goal of the algorithm is to deconvolute the one-dimensional mass/charge spectrum into a two-dimensional matrix of mass and charge values. To simplify the problem, mass is quantized by lipid count and limited to a specific range so that mass is equal to $P + kL$, where $k \in (75,76,\ldots,225) = K$. Charge is also quantized and limited to $z \in (3,4,\ldots,32) = Z$. These limits are empirically set at the beginning of the algorithm and are based on previously established values for Nanodisc lipid counts and charges.[83,94]

The matrix of (k, z) pairs arising from sets K and Z is defined as M. Each element of M has an m/z value defined by the function μ as $\mu(k, z) = \frac{P+kL+z}{z}$ for $(k, z) \in M$. The probability matrix, P, is defined with the same dimensions as M such that $P_{i,j} = \Pr(M_{i,j}) = \Pr(K_i, Z_j)$.

In preparation for analysis, the experimental spectrum is linearized and normalized. No other manipulation of the data is used, and no peak picking is necessary. For clarity, the function, $\beta(m/z)$, is defined as the intensity of the experimental spectrum at m/z.

The simplest deconvolution strategy would be to set the probability in P of any given $(k, z) \in M$ as:

$$\Pr(k, z) \propto \beta(\mu(k, z)) \tag{2.1}$$

Normalization of matrix, P, corrects the proportionality and converts P into a true probability distribution. However, this simple strategy is foiled by the constructive overlap of adjacent charge states because the peak at a given m/z value may contain contributions from a number of potential (k, z) pairs.

To correct for the overlap effect, another factor is added to Equation 2.1.

$$\Pr(k, z) \propto \beta\big(\mu(k, z)\big) \times L(k, z) \tag{2.2}$$

Where $L(k, z)$ is the proportion of the spectra intensity, $\mu(k, z)$, that should be assigned to the particular (k, z) pair. $L(k, z)$ is defined by three separate factors:

$$L(k, z) = \frac{\beta(\mu(k,z)) \times N(k,z)}{\sum_{i \in K} \sum_{j \in Z} \beta(\mu(i,j)) \times dist((i,j),(k,z)) \times N(i,j)} \tag{2.3}$$

β was previously defined as the spectra intensity. $dist$ is a distance cutoff defined by a Gaussian distribution centered at $\mu(k, z)$ with a standard deviation of σ_d:

$$dist\big((i, j), (k, z)\big) = \frac{1}{\sigma_d \sqrt{2\pi}} e^{-\frac{(\mu(i,j) - \mu(k,z))^2}{2{\sigma_d}^2}} \tag{2.4}$$

The value of σ_d in the distance factor has a significant impact on the deconvolution. Some tuning is required to find the optimal cutoff distance. When σ_d is small, P is noisy with significant background signal. The algorithm overcorrects for the overlap effect and distributes the peak intensity across too many charge states. When σ_d is large, the algorithm does not effectively account for the overlap effect. Too much of the intensity is distributed to the most probable charge state. In general, a σ_d value around 1.5 times the standard deviation of the narrow peaks gave the best fit.

N is a factor designed to capture the neighborhood of each (k, z) pair. The central assumption is that the probability of any given (k, z) pair is proportional to the probability of neighboring pairs, including $(k, z-1)$, $(k, z+1)$, and $(k-1, z)$ for example. The central assumption is that there will be a low probability of any (k, z) pairs appearing in isolation. Implementation of this concept requires an iterative updating of the probability matrix, P. For each iteration, the probability matrix, P^n, is calculated based on the prior probability matrix, P^{n-1}, and then normalized. The first iteration, P^0 is given a uniform probability, so the probability of overlapping peaks is approximately equal. On each subsequent iteration of the algorithm, the prior probability, P^{n-1}, is blurred by a Gaussian filter. In other words, the probability of a given (k, z) is the average of all surrounding pairs weighted by a Gaussian function centered at (k, z) with standard deviations (σ_1, σ_2) given by:

$$N(k,z) = \frac{\sum_{x\in K}\sum_{y\in Z}\frac{1}{\sigma_1\sqrt{2\pi}}e^{-\frac{(x-k)^2}{2{\sigma_1}^2}}\times\frac{1}{\sigma_2\sqrt{2\pi}}e^{-\frac{(y-z)^2}{2{\sigma_2}^2}}\times \mathrm{Pr}^{n-1}(x,y)}{\sum_{x\in K}\sum_{y\in Z}\frac{1}{\sigma_1\sqrt{2\pi}}e^{-\frac{(x-k)^2}{2{\sigma_1}^2}}\times\frac{1}{\sigma_2\sqrt{2\pi}}e^{-\frac{(y-z)^2}{2{\sigma_2}^2}}} \tag{2.5}$$

For this study, $\sigma_1 = 2$ and $\sigma_2 = 1$ were used as values for the standard deviation. However, the algorithm is relatively insensitive to the precise values of (σ_1, σ_2) or the shape of

the blurring filter. For example, taking the arithmetic mean of a one-pixel radius gives a similar result. In any case, the algorithm typically converges to a final solution within eight iterations.

Following determination of P, the quality of the fit is determined by projecting the probability matrix back into a simulated mass spectrum in m/z space. This is accomplished by summing Gaussian distributions centered at each m/z value in M with the intensity of each determined from P. Some care must be taken to find the appropriate width of the distributions and to account for any adducts or fragments (see below). The relative populations of adduct species and an initial guess for peak widths are determined by fitting only the overlap peaks at integer multiples of the lipid mass. After determining the final P, the peak widths are optimized for the best fit. The sum of squared errors (SSE) may then be calculated between the experimental spectrum and the simulated spectrum determined from the deconvolution.

2.3.4 Applying the Three-Component Model for Interpretation and Deconvolution of Nanodisc Native Mass Spectra

The high-resolution spectrum of DMPC Nanodiscs at 70 V ISCAD illustrates the effect of overlapping charge states on Nanodisc native mass spectra and demonstrates the power of the probability-based deconvolution algorithm. As shown in Figure 2.9A, the spectrum contains a number of sharp narrow peaks and five larger broad peaks. Three of the broad peaks occur at integer multiples of the lipid at $n = 9,10,$ or 11. Two other broad peaks are found at half way between integer multiples. These are the locations predicted by the charge state overlap theory as detailed in Section 2.3.2.

Zooming in to peak **1** at $10L$ (approximately 6780 Da) and its neighbors, it is clear that the overlap effect precludes assignment of the peak at 6780 Da. Potential Nanodisc ions of various charge states are labeled with vertical lines below the peaks in Figure 2.9B. For peak **1**,

the potential ions are very closely spaced (too close to label clearly). Even for peak **2**, which does not overlap perfectly, the difference between many of the possible ions is small. The position of some possible m/z pairs for peak **2** is marked with black boxes in the mass/charge matrix in Figure 2.9C to illustrate the wide range of charge states and lipid counts that could contribute to peak **2**. Peak **3** can be attributed primarily to the +22 charge state with a secondary contribution from the +23 charge state.

One notable feature of the spectrum is that the three peaks are not perfectly Gaussian in shape but show a similar pattern. Because all Nanodisc ions that contain integer values of lipid, protein, and charge cluster closely at peak **1**, it is impossible to attribute some of these shoulders to Nanodisc ions containing only protein and lipid. One possible assignment of these peaks is to various adducts and fragments. The shoulder at lower m/z can be attributed to loss of a phosphocholine fragment at 184 Da. This loss of phosphocholine from phosphatidylcholine lipids is a well-known fragmentation reaction[96,97] but could also be attributed to a low level of contaminating diacylglycerol in solution.

The shoulders at higher m/z are harder to assign. They are likely due to heterogeneous adduction of water or ions from solution. The largest potential adduct is a Tris ion at 121 Da. Although Tris is largely removed in the size exclusion column, it is possible that some remains bound.[98,99] For the deconvolution algorithm, peak **1** along with peaks near $9L$ and $11L$ were fit to four overlapping Gaussian distributions, the pure protein/lipid complex, the phosphocholine fragment, and adducts with one or two Tris molecules, to determine the relative population of each of these species and an appropriate peak width. The peak width of these four Gaussians is used to determine the cutoff distance, σ_d, used in Equation 2.4.

With an appropriate distance cutoff, each factor contributing to P in the probability-based deconvolution algorithm can now be considered in the context of peaks **1**, **2**, and **3**. For peak **1**, the $dist$ values will all be close to one because the possible m/z values are very close to each other. The spectral intensity factor, β, will also be very similar for all (m, z) pairs. The probability of each possible (m, z) pair close to peak **1** is therefore primarily determined by the neighborhood factor, N. N is initially uniform for each possible value but converges to the final solution. In the case of peak **1**, N converges to similar values for the +22 and +23 charge states and nearly zero for all others. Figure 2.9C shows the final distribution and illustrates why the neighborhood factor would be small for all other charge states.

For peaks **2** and **3**, N behaves similarly to peak **1**. However, the spreading of charge states causes differences in the β and $dist$ factors. β is highest for the +22 and +23 charge states, especially in peak **3**. The $dist$ factor will limit the intensity from being distributed to charge states that are far away from the central m/z. Thus, even when the neighborhood factor is uniform in the first iteration of the algorithm, the +22 and +23 charge states have the highest probability for peak **3**. As shown in Figure 2.9D, the final solution assigns probabilities to both the +22 and +23 charge state for all three peaks.

Considering the whole spectrum in Figures 2.9A and 2.9D, the deconvolution algorithm reveals the overlap of multiple charge states contributing to the broader peaks. The probability matrix, Figure 2.9C, shows a centralized distribution of mass and charge. Summing the columns of the matrix yields the overall lipid distribution. For simplification, the lipid count distribution may then be fit to a Gaussian to determine the lipid count mean and standard deviation.

The same deconvolution algorithm was applied to high-resolution Nanodisc spectra with increasing levels of fragmentation. The deconvolution matrices for DMPC Nanodiscs at various

fragmentation energies with both in-source collision activated dissociation (ISCAD) and infrared multiphoton dissociation (IRMPD) are given in Figures 2.10A and 2.10B respectively. The overall lipid distributions from these matrices are shown in Figures 2.10C and 2.10D. Plotting the lipid count mean and standard deviation as a function of ISCAD voltage or IRMPD laser duration (Figure 2.11) provides a quantitative picture of Nanodisc fragmentation. The experimental data and final fits for each spectrum are shown in Figure 2.12 and Figure2.13.

For this data, the lipid count is slightly higher and the distribution is slightly broader than determined from the two-component model and low-resolution data described in Section 2.3.1. The mean lipid count is 165 at the 10 V ISCAD, whereas the literature value is reported at 154.[94] The elevated lipid count may be due to sample-to-sample variation or to gas-phase association with free lipid molecules. As described above,[83] lipid monomers and small oligomers are observed in the low mass region of all spectra. The lipid count standard deviation varies from ±4 at low fragmentation energies to ±7 at the highest. Although there is some background outside of these central distributions, especially at higher fragmentation energies, these data suggest that Nanodiscs undergo a rather well defined fragmentation pathway, staying relatively tightly grouped as they lose lipids.

One interesting feature observed in some of the IRMPD spectra is that the constructive overlap of adjacent charge states is relatively minor. This is due to charge reduction caused by IRMPD fragmentation. At lower charges, Nanodisc ions shift to higher m/z, and the regions of potential overlap shift to higher nL values. Because $n = k_1 - k_2$, where k_1 and k_2 are the overlapping lipid counts, overlap is more likely at lower values of n. For peak **1** at $10L$, lipid counts that are 10 apart have the potential to overlap. Because the lipid count distribution is ±5 at 70 V ISCAD, overlap is likely. However, at $22L$ (the highest peak in the 0.9 s IRMPD spectrum,

see Figure 2.13), lipid counts must be 22 apart to overlap. Because the central distribution is ±6 for this spectrum, overlap is unlikely. Minor overlap does occur, and it can be attributed to the presence of background peaks outside of the central distribution.

A major advantage of the probability-based deconvolution algorithm is that it does not assume a given model, such as a Gaussian distribution. Although the algorithm considers the neighborhood, the probability of each (m, z) pair is determined individually. This raises the question of whether the number of independent variables included in the probability-based deconvolution is statistically justified. Using the K and Z sets defined above, the probability matrix contains 4530 elements, which is more than the number of data points in some spectra. However, removal of all elements of P with a value smaller than 1% of the maximum probability in P reduces the number of variables in the model by a half to full order of magnitude without significantly reducing the quality of the fit.

A Levenberg-Marquardt algorithm was used to fit other models for the lipid and charge distributions, including Gaussian, Cauchy, and skewed distributions. The best of these was a Cauchy distribution in the lipid count and a Gaussian distribution in charge, based on a modified square root relationship to its mass (see Stengel *et al.*[100]). However, none of these distributions fit the spectra well. F-tests comparing the reduced probability-based model with the Cauchy distribution model revealed that the probability-based model was significantly better than the simpler models.

2.4 Conclusions

This chapter described the analysis of intact Nanodisc complexes by mass spectrometry. The theoretical basis of the constructive overlap of adjacent charge state was presented along with a probability-based algorithm to deconvolute these overlapping distributions. As

demonstrated with DMPC Nanodisc spectra at a range of fragmentation energies, charge state overlap plays a significant role in shaping the spectra, and a three-component model is superior to the simpler two-component model. The probability-based deconvolution algorithm provides an effective strategy for determining the lipid count distribution. The theoretical work and algorithms developed in this report will be critical for future studies of Nanodiscs with membrane proteins and mixed lipid populations. Also, the probability-based deconvolution approach could find applications in other native mass spectrometry systems with overlap of charge states from oligomeric species, such as heat shock proteins[100-102] and amyloid oligomers.[103]

Native electrospray MS provides structural information on protein complex subunit identity, stoichiometry, and interactions.[91] Native MS of membrane-bound proteins is currently accomplished by applying moderate collision energy to "shake off" detergent so that homogeneous membrane protein complexes emerge from heterogeneous detergent micelles.[89,104] Given the important protective nature of these micelles, there has been significant interest in understanding the behavior of detergent and lipid complexes in the gas phase.[95,105] Whether surfactant aggregates in the gas phase mirror solution-phase aggregates has been a matter of debate in the field of native mass spectrometry.[106] These results demonstrate that Nanodisc complexes in the gas phase closely mirror the properties of Nanodiscs in solution. This is likely due to the constraint from the MSP belt, which maintains the defined structure of the Nanodisc complex.

Native MS for analysis of Nanodiscs holds unique potential as a launch pad for studying membrane protein complexes. Given that Nanodiscs contain a native-like lipid bilayer, they provide a more physiologically relevant environment to study membrane protein complexes than

do micelles. Nanodiscs are also more monodisperse than detergent micelles, and the lipid content of the Nanodisc can be tailored to permit investigation of protein-lipid interactions. Two previous reviews speculated that Nanodiscs could be used to solubilize membrane proteins for native mass spectrometry.[90,107] This chapter provides the first experimental evidence for this possibility and lays the groundwork for performing and interpreting future studies of Nanodisc-solubilized membrane complexes by top-down, ion mobility, and other gas-phase analysis techniques.

2.5 Figures

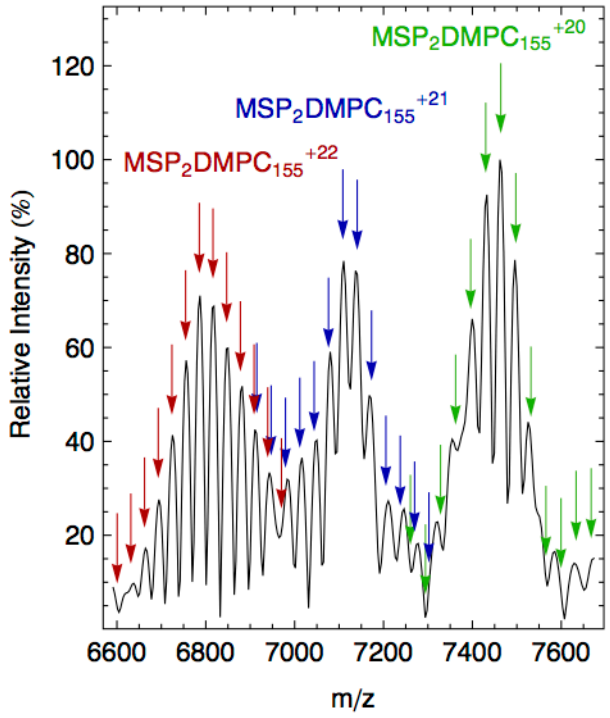


Figure 2.1: Native mass spectrum at 70 V ISCAD of DMPC Nanodiscs (*black*) with simulated masses of the +22 (*red*), +21 (*blue*), and +20 (*green*) charge states for Nanodisc complexes with two MSP molecules, six bound water molecules, and an average of 155 DMPC molecules. Arrows of the same color show simulated values for Nanodiscs in the same charge state with a varying number of lipid molecules. The average, 155 lipids, is the highest peak in each charge state. Simulated m/z values are marked by the arrows, and their vertical position was matched with the intensities of mass spectrum.

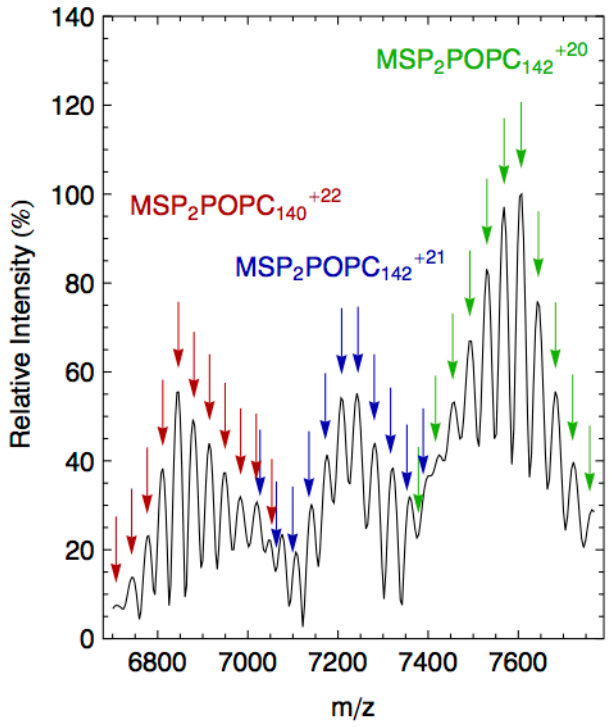


Figure 2.2: Native mass spectrum at 70 V ISCAD of POPC Nanodiscs (*black*) with simulated masses of the +22 (*red*), +21 (*blue*), and +20 (*green*) charge states for Nanodisc complexes with two MSP molecules, five bound water molecules, and an average of 141 POPC molecules. Arrows of the same color show simulated values for Nanodiscs of the same charge state with a varying number of lipid molecules. The highest peak in each charge series is annotated. Simulated m/z values are marked by the arrows, and their vertical position was matched with the intensities of mass spectrum.

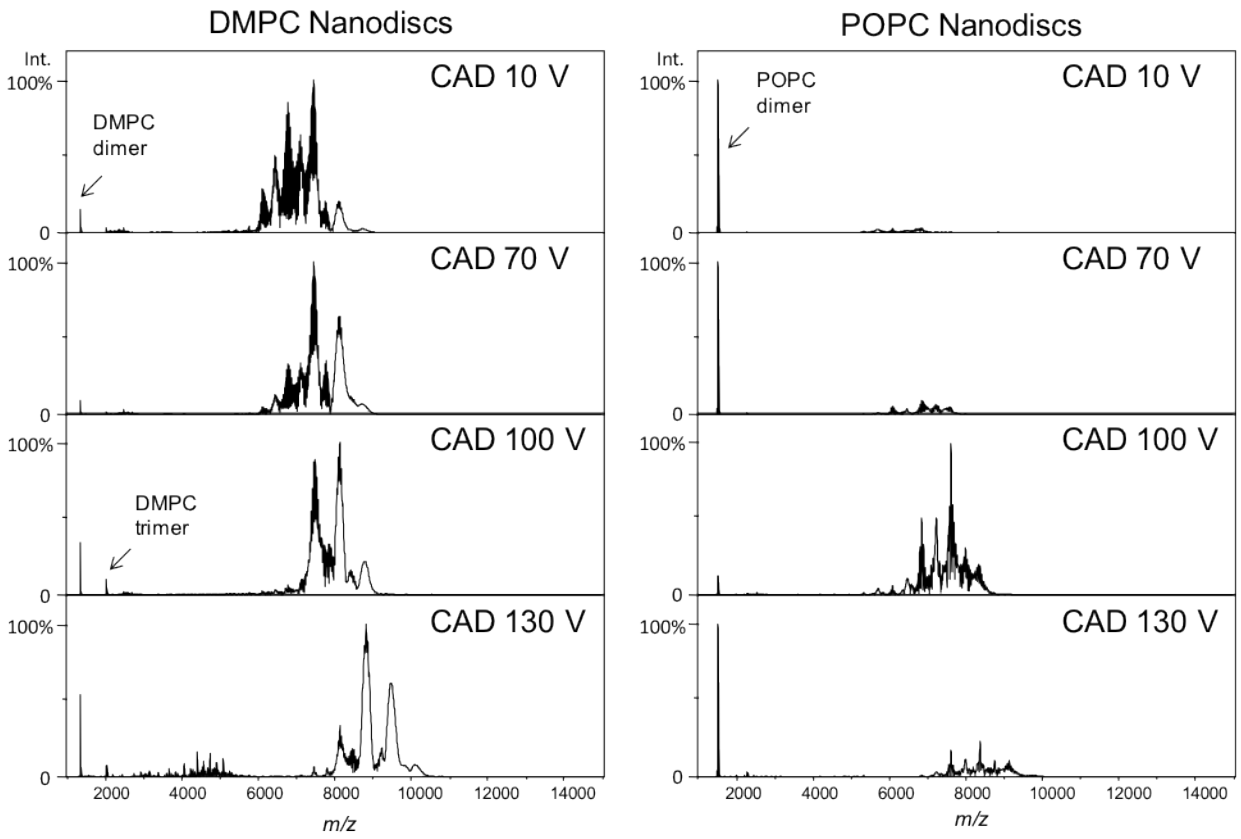


Figure 2.3: The full spectra of DMPC (*left*) and POPC (*right*) Nanodiscs at different in-source ISCAD voltages. A close up of the higher mass range for each spectrum is given in Figures 2.4. The ISCAD 70V spectra are fit to models in Figures 2.1, 2.2, 2.5, and 2.6.

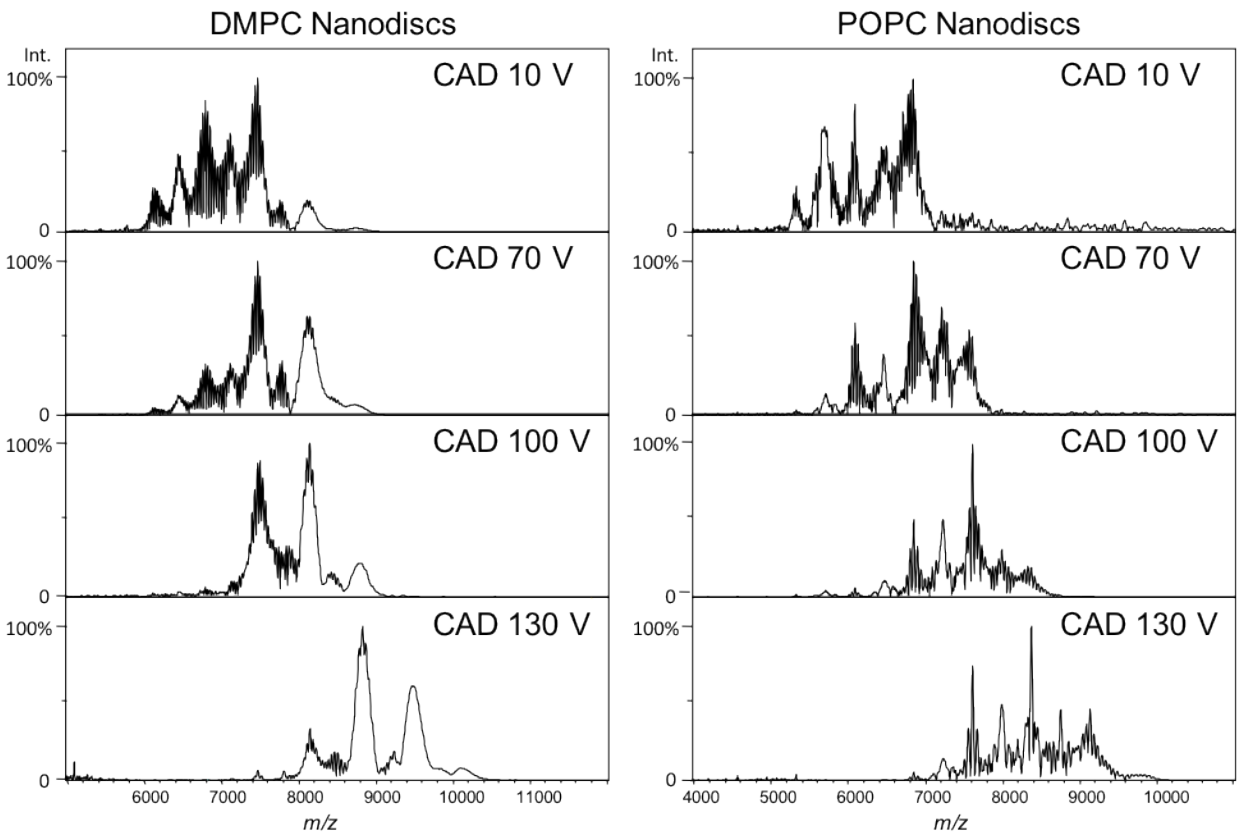


Figure 2.4: The native mass spectra of DMPC (*left*) and POPC (*right*) Nanodiscs at different ISCAD voltages. For full spectra, see Figure 2.3.

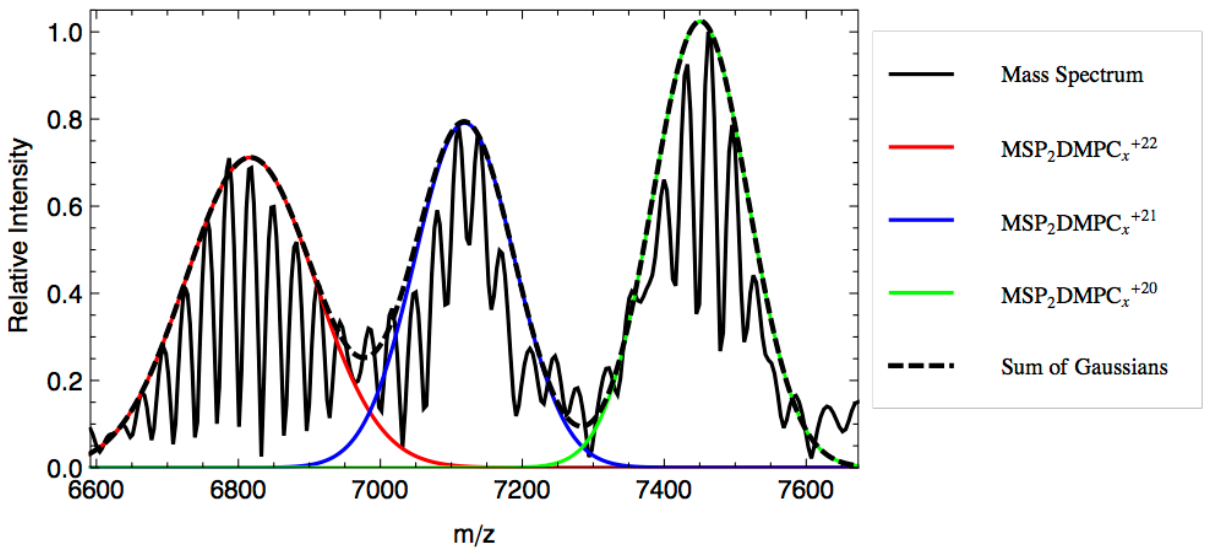


Figure 2.5: Fit of DMPC Nanodisc native mass spectra at 70V ISCAD (from Figure 2.1 and Figure 2.3) to three overlapping Gaussian distributions.

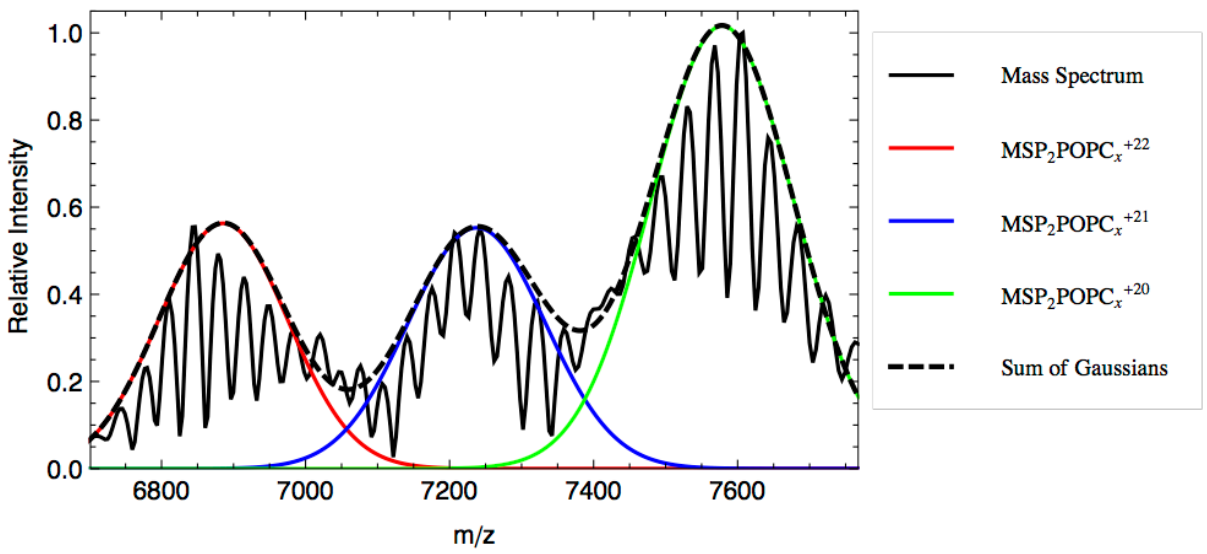


Figure 2.6: Fit of POPC Nanodisc native mass spectra at 70V ISCAD (from Figure 2.2 and Figure 2.3) to three overlapping Gaussian distributions.

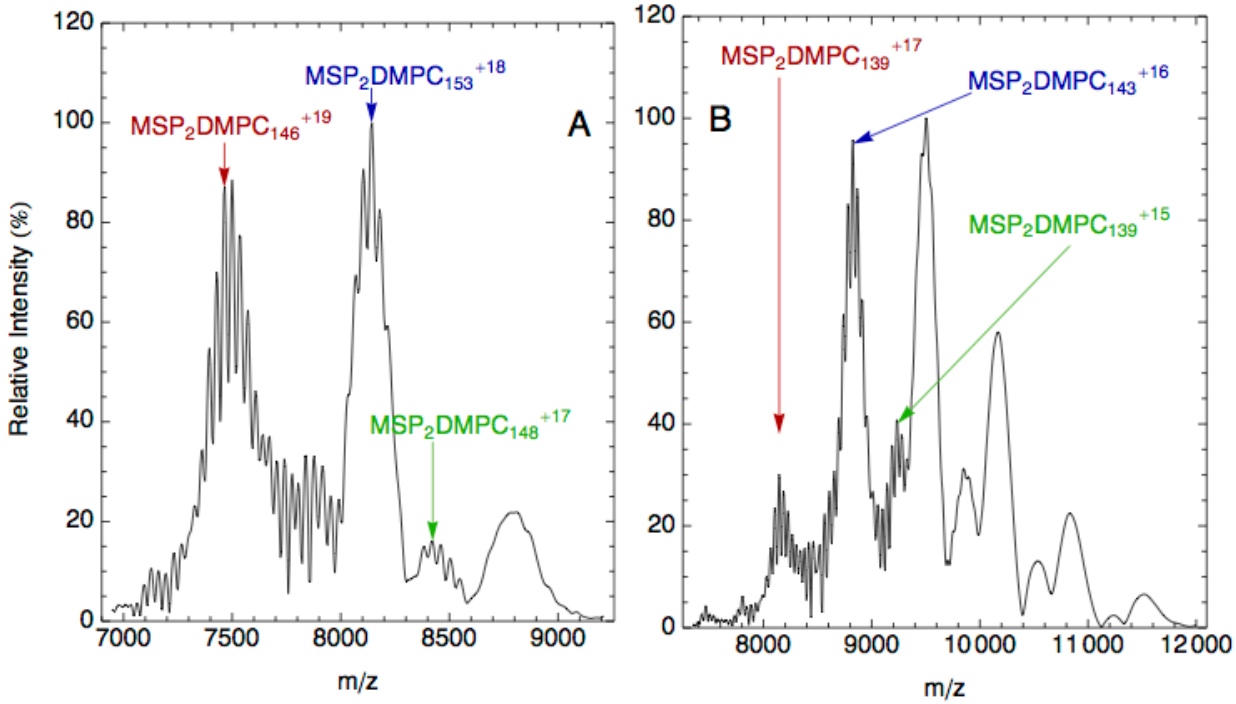


Figure 2.7: Native mass spectrum of DMPC Nanodiscs with (*A*) 100V ISCAD and with (*B*) 130V ISCAD combined with 0.1 V and 10 ms ECD. Determining the fine spacing of peaks allows assignment of charge state and lipid count for some peaks. Charge states and the associated lipid composition for a single peak in each series are annotated. Full spectra are shown in Figure 2.3.

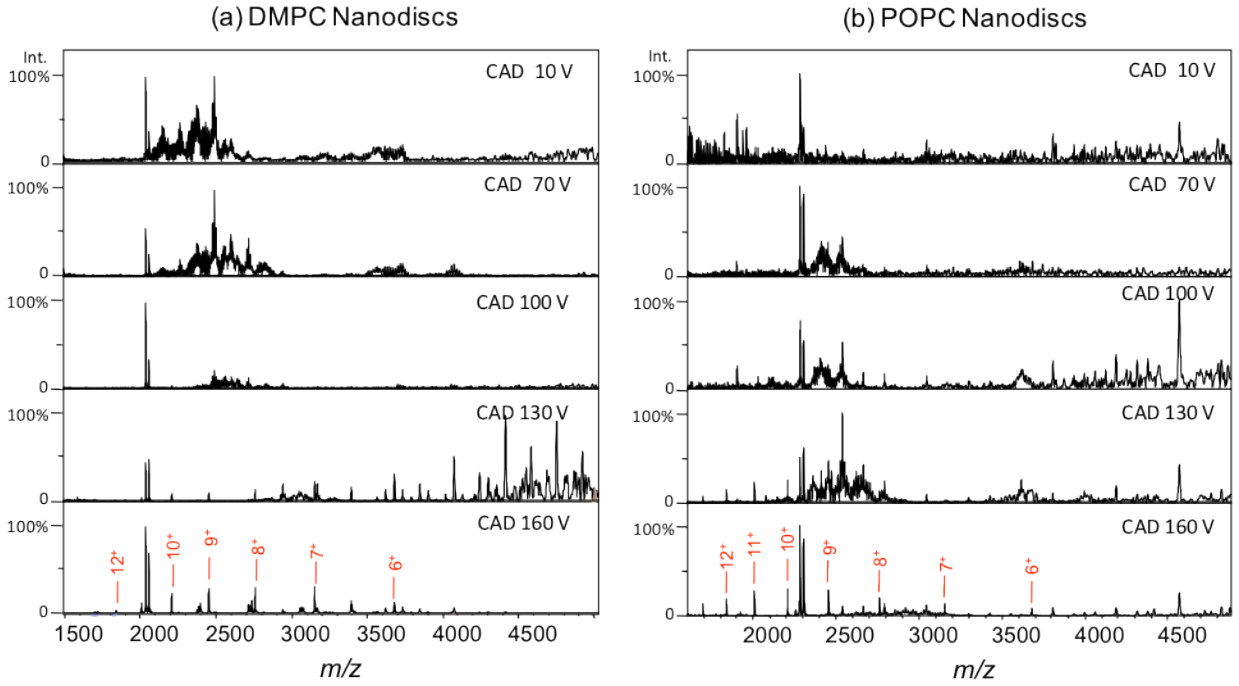


Figure 2.8: Low *m/z* range of ISCAD spectra of DMPC (*a*) and POPC Nanodisc (*b*). The peaks of membrane scaffold protein (*red*) demonstrate that scaffold protein is released at higher collision energies.

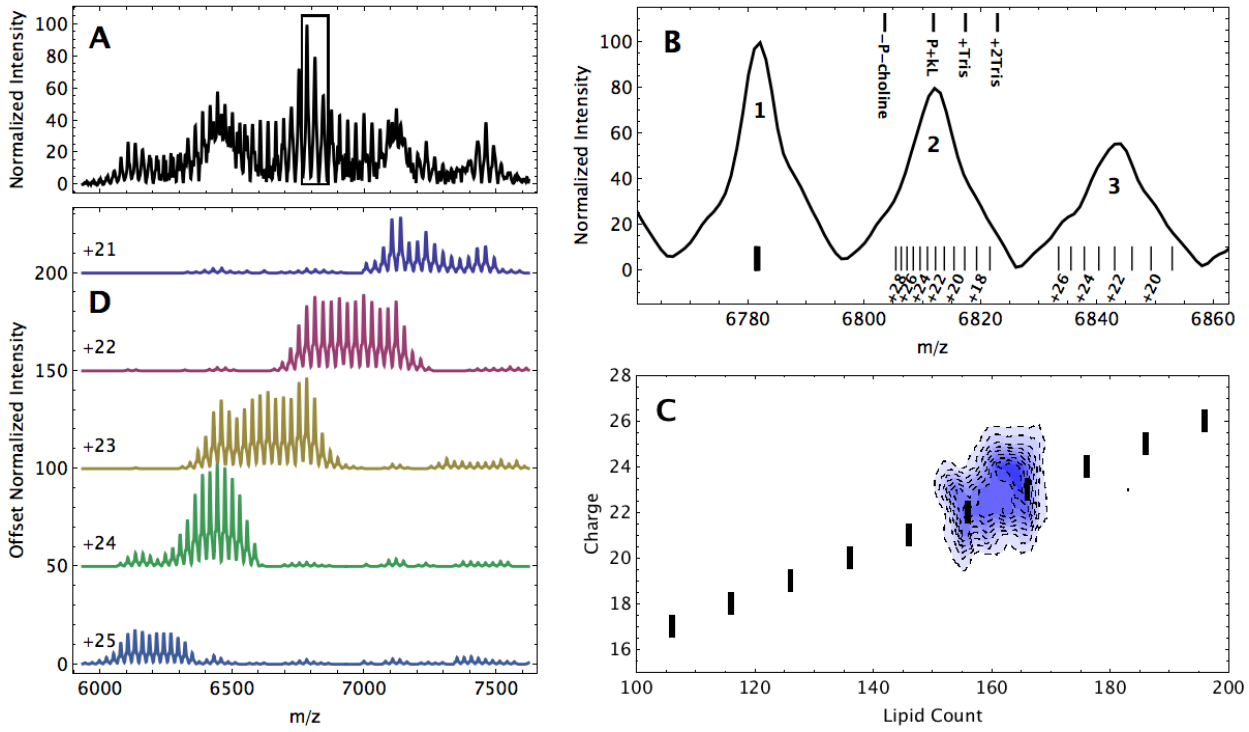


Figure 2.9: Native mass spectrum (*A*) of DMPC Nanodiscs at 70 V ISCAD. A zoom of the boxed region in *A* is given in *B*. Position of the nearest Nanodisc ions are marked with vertical lines below the spectrum, and ions with an even charge are annotated. Ions on peak **1** at $10L$ are very closely spaced, and hence not labeled. Because each peak is not perfectly Gaussian, other possible species are marked above peak **2** for the center peak with the adduction of one or two Tris molecules or the loss of a phosphocholine fragment. The mass and charge values for peak **2** are marked as black boxes in the deconvolution matrix (*C*). The blue contour plot presents the deconvoluted lipid count and charge distributions. Projection of deconvolution into m/z space is shown in *D* with offset charge states for the most abundant charges.

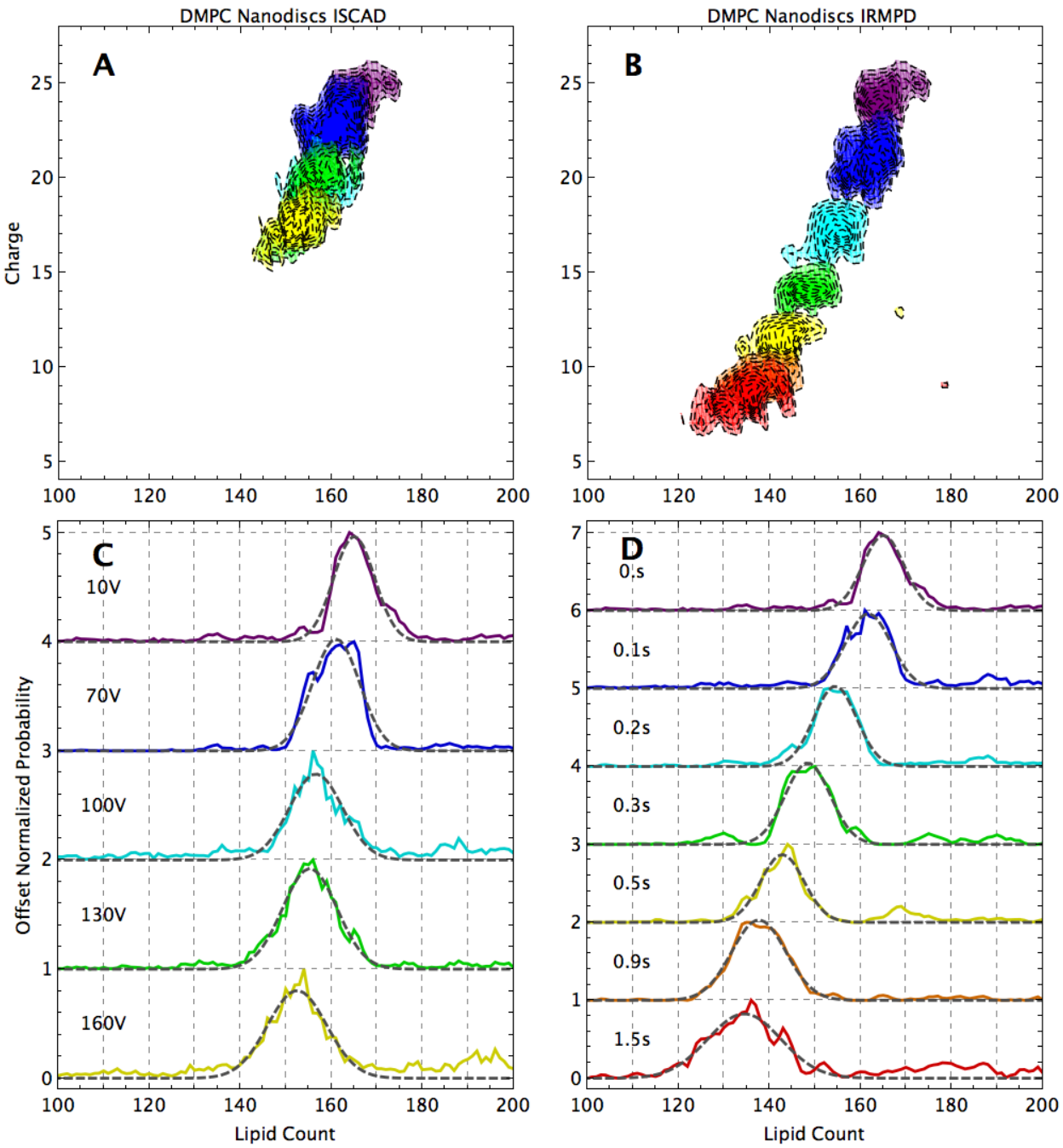


Figure 2.10: Deconvolution of lipid count and charge for DMPC Nanodiscs at a variety of fragmentation energies from both (*A*) ISCAD and (*B*) IRMPD. Summation of the columns from these matrices gives the lipid count distributions, which are plotted below in *C* and *D*. Regions from the top contour plots correspond with the same color that is labeled in the bottom distributions. Fits of each lipid count distribution to a Gaussian distribution are shown as black dashed traces in *C* and *D*.

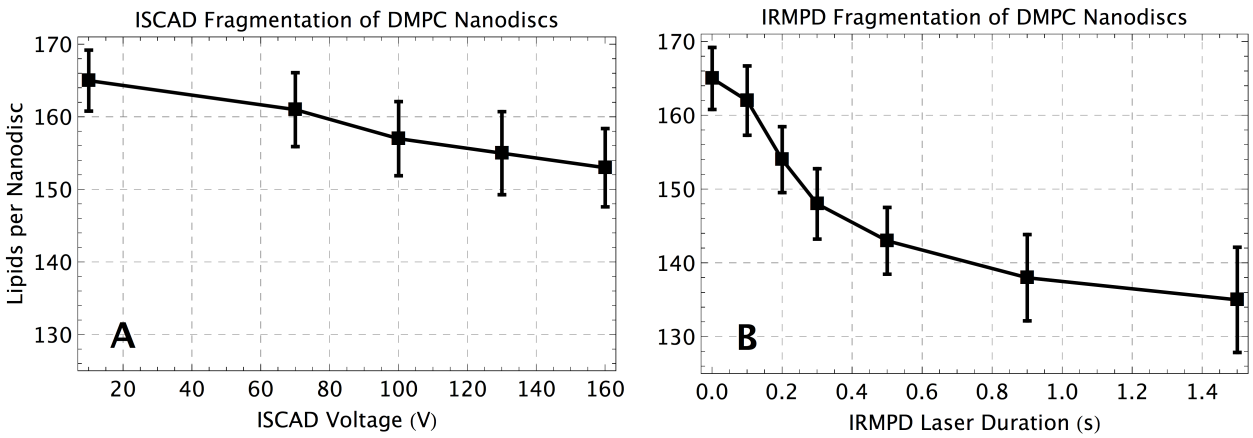


Figure 2.11: Lipid count distribution for DMPC Nanodiscs as a function of (*A*) ISCAD voltage and (*B*) IRMPD laser duration. Error bars are shown at one standard deviation. Mean and standard deviations are taken directly from the fits in Figures 2.10B and D.

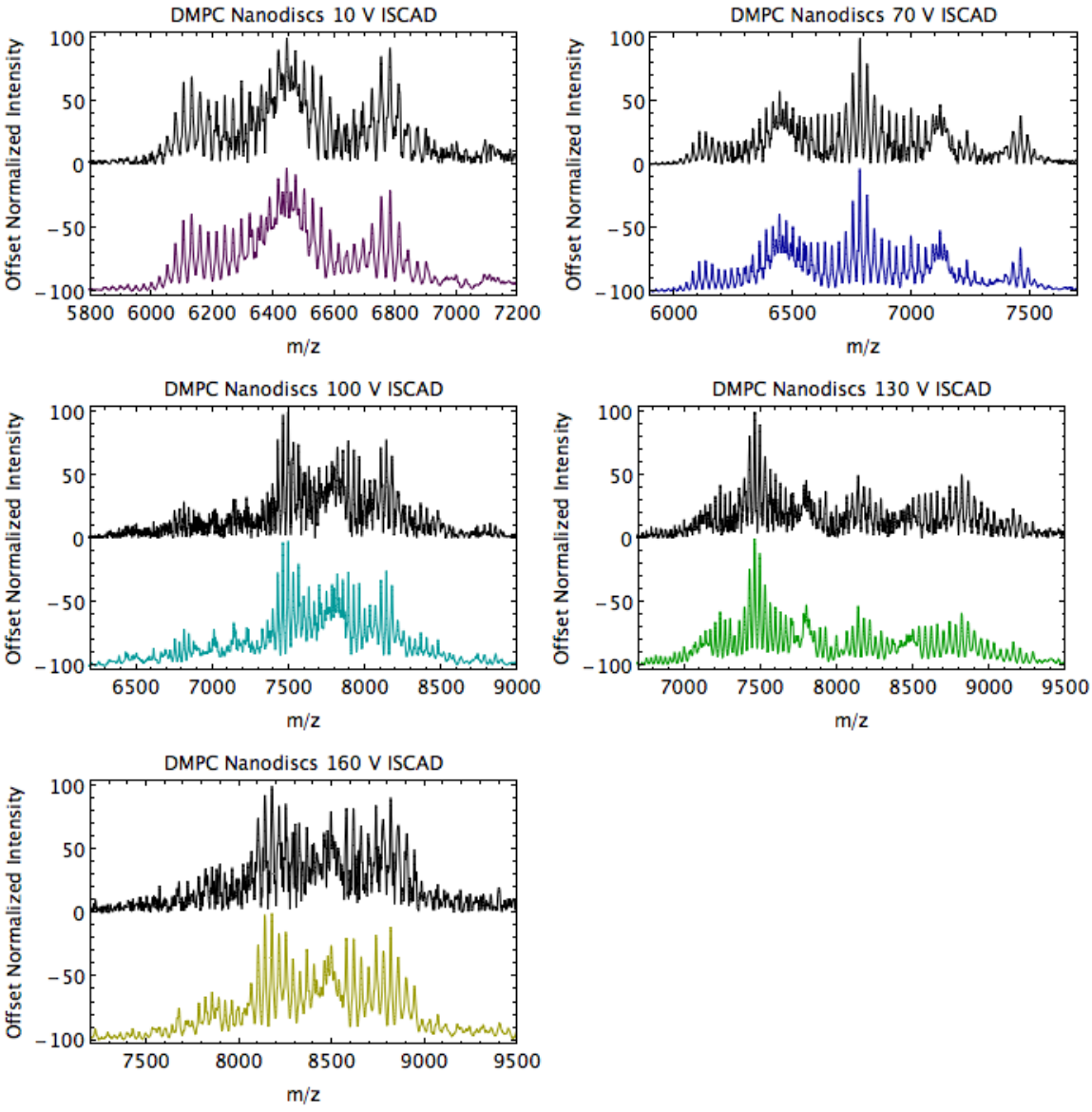


Figure 2.12: Mass spectra (*black, top*) and fits (*colored, bottom*) for DMPC Nanodiscs at various levels of ISCAD fragmentation energy. Each lower colored spectrum corresponds with the color scheme used in Figure 2.10.

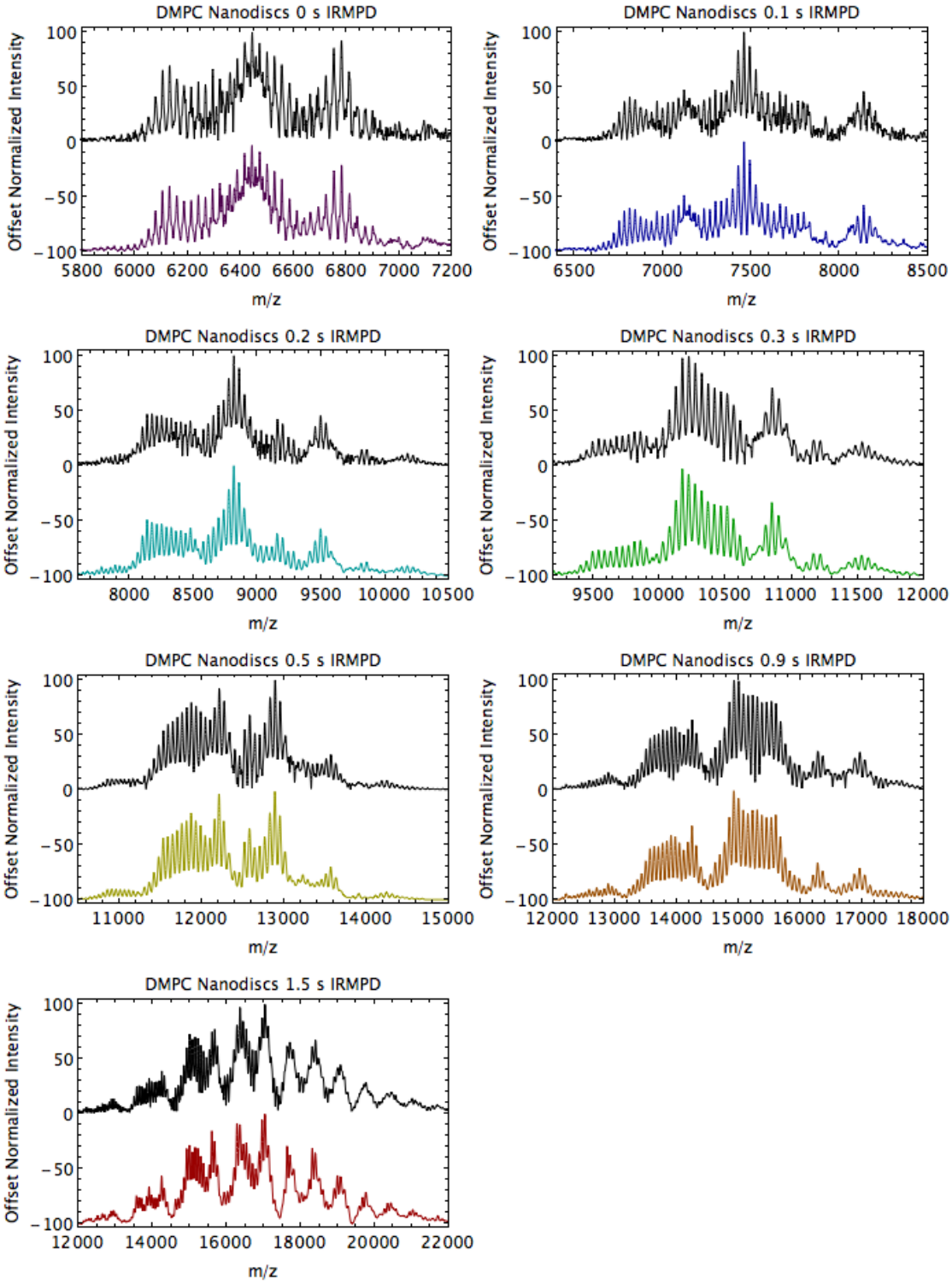


Figure 2.13: Mass spectra (*black*, *top*) and fits (*colored*, *bottom*) for DMPC Nanodiscs at various levels of IRMPD laser durations. Each lower colored spectrum corresponds with the color scheme used in Figure 2.10.

CHAPTER 3: DEVELOPMENT AND CHARACTERIZATION OF *E. COLI* NANODISC-SOLUBILIZED MEMBRANE PROTEIN LIBRARY

3.1 Introduction

Identification of membrane protein receptors for soluble ligands has the potential to reveal new drug targets and to elucidate important biochemical interactions. However, isolating membrane protein targets is challenging due to the difficulty of solubilizing membrane proteins outside of the lipid bilayer without disrupting native interactions.[108,109] *In vivo* studies, including yeast two-hybrid[110] and fluorescence resonance energy transfer, have been applied to mapping membrane protein interactions. However, these whole-cell measurements suffer from high levels of false positives and false negatives, and they require genomic modification of proteins to introduce appropriate labels.[111] *In vitro* measurements are complicated by the need to solubilize membrane proteins using detergents, which can disrupt key protein-protein interactions and interfere with down-stream analysis methods.[108]

Nanodiscs have proven to be an effective technology for solubilizing membrane proteins in detergent-free buffers.[94] Typically, the protein of interest is purified and isolated prior to incorporation. Controlling the ratios of membrane proteins and MSP allows the assembly of membrane protein-Nanodisc complexes with defined stoichiometry.[48,112] Civjan *et al.*

Reproduced in part with permission from Marty, M.; Wilcox, K.; Klein, W.; Sligar, S. Nanodisc-solubilized membrane protein library reflects the membrane proteome. *Anal. Bioanal. Chem.* **2013**, *405*, 4009-4016. Copyright 2013 Springer. The published version may be found online at http://link.springer.com/article/10.1007%2Fs00216-013-6790-8.

demonstrated that a functional cytochrome P450 may be incorporated directly from a solubilized membrane and can be purified post-incorporation.[32]

As described in Section 1.4.3, Nanodiscs have been used in previous proteomics applications as "bait" for isolating and identifying glycolipid and membrane protein interaction partners. Borch *et al.* assembled Nanodiscs with ganglioside GM1.[80] Co-immunoprecipitation of the GM1 Nanodiscs with culture media from *Escherichia coli* (*E. coli*) isolated heat labile enterotoxin B. Another study assembled Nanodiscs with membrane transporters SecYEG and MalFGK, and each membrane protein-Nanodisc system was incubated with stable isotope-labeled cell culture extracts.[81] Soluble proteins interacting with the membrane protein bait in Nanodiscs were isolated, separated with sodium dodecyl sulfate-polyacrylamide gel electrophoresis (SDS-PAGE), and identified with liquid chromatography-tandem mass spectrometry (LC-MS/MS). Both studies demonstrated the utility of Nanodiscs as a platform for interactomics.

Although previous studies have measured the interaction of a heterogeneous soluble protein pool with homogenous Nanodiscs containing a single membrane protein species, it is possible to invert the experiment to measure the interaction of a single homogenous soluble ligand with a heterogeneous Nanodisc-solubilized membrane protein library (SMPL). In such an experiment, Nanodiscs serve as the "prey" towards immobilized ligand bait. This inversion allows isolation and identification of unknown membrane protein targets *in vitro* without the need for detergent buffer. However, the utility of this approach depends on the formation of SMPL Nanodiscs that faithfully reflect the membrane proteome. This chapter details a general protocol for optimization of SMPL formation and examines the degree to which the SMPL reflects the membrane proteome of pooled inner and outer membranes from *E. coli*.[84]

3.2 Experimental Methods

3.2.1 Materials

Lysozyme, octyl-β-glucoside, imidazole, ampicillin, ethylenediaminetetraacetic acid (EDTA), and Amberlite XAD-2 beads were purchased from Sigma-Aldrich (St. Louis, MO). Phenylmethanesulfonyl fluoride (PMSF) was obtained from Fisher Scientific (Pittsburgh, PA). Sodium cholate as obtained from Affymetrix (Maumee, OH). Sodium dodecyl sulfate was purchased from Bio Rad (Hercules, CA). 1-palmitoyl-2-oleoyl-*sn*-glycero-3-phosphocholine (POPC) was obtained from Avanti Polar Lipids (Alabaster, AL).

3.2.2 *Escherichia coli* Growth and Membrane Isolation

Library competent $DH_{5\alpha}$ *E. coli* cells were purchased from Invitrogen and transformed with pUC 19 control DNA plasmid. Cells were cultured in terrific broth media with 100 μg/mL ampicillin and were grown for 24 hours. Cell pellets were harvested by centrifugation and frozen at -80 °C. Cell pellets were resuspended in cold lysozyme buffer (75 mM Tris HCl, 0.25 M sucrose, 0.25 mM EDTA, 0.02 mg/mL lysozyme, pH 8) and pelleted again by centrifugation. Pelleted cells were resuspended in cold lysis buffer (50 mM Tris HCl, 1 mM PMSF, pH 8) and were lysed by sonicating on ice. Lysed cells were centrifuged at 2000×*g* for 10 minutes at 4 °C to remove any unbroken cells or debris. The supernatant was removed and centrifuged at 90000×*g* (maximum radial centripetal force) for 1 hour to harvest the cell membrane.[9] The membrane pellet was resuspended in 0.1 M phosphate buffer, pH 7.7, and flash frozen. The concentration of membrane proteins in the resuspension was typically 2 mg/mL, as measured by a bicinchoninic acid (BCA) assay (Thermo Scientific, Rockford, IL).

3.2.3 Detergent Extraction of Membrane Proteins

Assembly of membrane proteins into Nanodiscs relies on the initial solubilization of the membrane protein in detergent. The membrane solution was centrifuged at 12000×*g* for 30 minutes. Membranes were resuspended in an equal volume of either octyl-glucoside (OG) buffer (1% w/v OG, 0.1 M phosphate, pH 7.7) or sodium dodecyl sulfate (SDS) buffer (0.1% w/v SDS, 20 mM Tris, 0.1 M NaCl, 0.1% w/v sodium azide). Membranes were thoroughly mixed and incubated at room temperature for 15 minutes to extract membrane proteins. Insoluble membranes were removed by centrifugation at 12000×*g* for 15 minutes. The concentration of membrane proteins in the detergent extract was measured by a BCA assay. Typically, the membrane protein concentration was 1-2 mg/mL in the detergent extract.

3.2.4 Nanodisc-Solubilized Membrane Protein Library Preparation

Expression and purification of membrane scaffold protein (MSP) was described previously.[27,28] MSP1E3D1, a variant of MSP with three extended helices and a polyhistidine tag, was used because this scaffold makes Nanodiscs with a 12.1 nm Stokes diameter that will accommodate large membrane proteins. This represents an upper limit on the size of membrane proteins or complexes that will be incorporated in the Nanodisc, as anything that extends more than 12 nm along the membrane will not fit inside the Nanodisc. Membrane proteins that extend less than 12 nm along the membrane may be incorporated in Nanodiscs and may extend any length perpendicular to the membrane surface, which will increase the overall Stokes diameter of the Nanodisc complex. MSP from a stock concentration of around 175 μM was added in a ratio ranging from 2 to 20 μg membrane proteins in detergent per nmol MSP. POPC in chloroform was dried under nitrogen and solvated in 0.1 M sodium cholate to 50 mM concentration. The molar ratio of POPC:MSP was tested within the range of 40 to 130 as described below.

Detergent-solubilized membrane proteins, MSP, and cholate-solubilized POPC were combined. Extra cholate was added to bring the final cholate concentration to 20 mM. This reconstitution mixture was incubated for two hours at 4 °C. Self-assembly of the Nanodisc library was initiated by adding 0.5-0.8 g Amberlite XAD-2 hydrophobic beads per mL of reconstitution mixture, and the mixture was incubated overnight on an orbital shaker at 4 °C. The Amberlite XAD-2 hydrophobic beads serve to remove the detergents and drive Nanodisc assembly.

Nanodiscs were purified by immobilized metal affinity chromatography. The reconstitution mixture was removed from the hydrophobic beads and filtered through a 0.22 μm filter from Millipore (Marlborough, MA). Filtered reconstitution mixture was loaded on nickel-nitrilotriacetic acid (Ni-NTA) agarose resin (Qiagen, Valencia, CA), washed with buffer containing 15 mM imidazole, and eluted in buffer containing 500 mM imidazole. The Ni-NTA column captured Nanodiscs by the poly-histidine tag on MSP1E3D1, washing away proteins or lipids not incorporated into Nanodiscs.

Size exclusion chromatography (SEC) was performed with a calibrated Superdex HR 200 10/30 size exclusion column (Amersham-Pharmacia Biotech, Piscataway, NJ). Samples were filtered prior to analysis and injected using a 500 μL sample loop and a flow rate of 0.5 mL/min. To evaluate the optimal protein to lipid ratio, a chromatogram from lipid-only POPC Nanodiscs was aligned with chromatograms from SMPL Nanodiscs of various lipid ratios with a custom program in Mathematica 8.0.4. The sum of squared errors was calculated between the SMPL Nanodisc chromatograms and the aligned control Nanodisc chromatogram.

3.2.5 SDS-PAGE Analysis

SDS-PAGE analysis of membrane protein libraries in Nanodiscs is complicated by the large excess of MSP in the sample. To observe the proteins in the Nanodisc library, MSP was removed by a Ni-NTA column. Samples were loaded on the column, washed with a 15 mM imidazole buffer, and eluted by adding buffer with 50 mM sodium cholate. The cholate disassembled the Nanodiscs allowing the membrane proteins to elute from the column while MSP remained bound. Membrane proteins released from the Nanodiscs, proteins from the raw membranes, and proteins from the detergent extract were prepared for SDS-PAGE using a methanol-chloroform-water precipitation to remove lipids, salts, and detergents.[113] Around 10 μg total protein was used for each precipitation. Precipitated samples were dissolved in Laemmli buffer, incubated at 70 °C for 20 min, and separated on Bio Rad Mini-PROTEAN TGX 12% PAGE gels. Gels were stained with Imperial Protein Stain (Thermo Scientific) and imaged with a Molecular Dynamics Typhoon 9400 Multilaser Scanner. Multiple gels were analyzed with similar results, but data is shown for a single gel.

Image analysis of gels was performed using a custom program in Mathematica 8.0.4. Median value of the pixel intensity was calculated for each row of pixels in a lane for the region ranging from 20 kDa to 100 kDa. Peaks in the line trace were identified using a custom continuous wavelet transform algorithm.[114] Peaks were considered overlapping if they were within 16 pixels; the total region of consideration was around 1600 pixels.

3.2.6 Proteomic Identification

Gel slices were excised, destained, and digested in 25 μL sequencing-grade trypsin (G-Biosciences, St. Louis, MO) at a concentration of 12.5 ng/μL with a CEM Discover microwave digester (Mathews, NC) for 15 minutes at 55 °C. Peptides were extracted using 50% acetonitrile

with 5% formic acid, dried, and resuspended in 13 μL of 5% acetonitrile with 0.1% formic acid. Ten μL were injected for LC-MS/MS.

Mass spectrometry (MS) was performed on a Waters quadrupole time-of-flight connected to a Waters nano Acquity Ultra Performance Liquid Chromatography system. A Waters Atlantis C-18 column (0.003 mm particle, 0.075 mm by 150 mm) was used at a flow rate of 250 nL/min. Peptide elution was performed using a linear gradient of water with acetonitrile containing 0.1% formic acid with the gradient ramping from 0-60% acetonitrile over one hour. Mass spectrometry utilized data dependent acquisition with MS/MS scans being performed on the four most abundant peaks at a given time. Data analysis was performed using the Waters Lynx Global Server 2.2.5 and Mascot (Matrix Sciences). Mascot searches were performed with the NCBI NR database and the SwissProt database specifying *E. coli* as the organism. Both databases gave similar results. The peptide tolerance was set to 0.5 Da for both MS and MS/MS measurements. One missed trypsin site as well as variable oxidation of methionine were allowed.

3.3 Results and Discussion

There are several important steps and variables to consider when preparing a Nanodisc library (see Figure 3.1 for schematic). The best approach for each step will depend on the specific biological system of interest. This chapter outlines a generalized protocol for the formation of Nanodisc-solubilized membrane protein libraries and characterizes the method as applied to a prototype *E. coli* membrane system.

3.3.1 Isolation and Detergent Extraction of Membrane Proteins

SMPL formation begins with isolated membranes. Inner and outer membranes from *E. coli*, which provide a well-characterized assortment of membrane proteins for establishing benchmarks for SMPL formation, were used as a prototype membrane system. The membrane

protein pool is solubilized in detergent to extract proteins. The type, concentration, and molar amount of detergent will all be potentially important parameters in solubilization because any unextracted proteins will not be incorporated into Nanodiscs. A detailed investigation of detergent extraction is outside the scope of this chapter but may be found in several reviews.[8-12] In general, the best detergent system will efficiently extract the membrane proteins without denaturing them.

Two detergent systems were tested for SMPL formation, 1% octyl-glucoside (OG) and 0.1% sodium dodecyl sulfate (SDS). Each was used at a ratio of around 1-2 mg of membrane protein per mL detergent solution. Both detergent systems efficiently extracted membrane proteins and were compatible with Nanodisc formation as seen by SEC and SDS-PAGE analysis (data shown for OG only). Because it is impossible to analyze whether every extracted protein retains its native fold and activity, it is advisable to screen several detergents to find the best system to maintain the specific biological interaction of interest. Due to its widespread use to solubilize functional membrane proteins[8,115] and its compatibility with SMPL formation, 1% OG was used for the remainder of the studies.

3.3.2 Nanodisc Formation

There are two key ratios to consider for SMPL formation. The first is the ratio of membrane protein to MSP. In general, an excess of MSP and lipid is used to drive the system towards a single protein or complex in each Nanodisc.[31,48,116] At higher loading ratios, the probability increases of multiple proteins randomly incorporating into a single Nanodisc. This is undesirable for most applications as it could lead to nonspecific interaction or co-localization of proteins that randomly become incorporated into the same Nanodisc complex. However, at lower ratios, the excess of empty Nanodiscs dilutes the membrane protein concentration leading to

higher levels of background MSP and lipids. A range of loadings from 2 to 20 μg membrane protein (MP) per nmol MSP were evaluated. Increasing the membrane protein loading showed a shift in the SEC peak as the incorporation of membrane proteins into the Nanodiscs increased the average Stokes diameter of the particles. A ratio of 10 μg MP/nmol MSP was used for optimization of lipid:MSP ratios. At this ratio, the average Stokes diameter is 12.7 nm, 0.6 nm larger than empty Nanodiscs (Figure 3.2). Assuming an average membrane protein (MP) molecular weight of 50 kDa, the ratio, 10 μg MP/nmol MSP, will be 0.2 nmol MP/nmol MSP or 0.4 nmol MP/nmol Nanodiscs, because each Nanodisc contains two MSP molecules. Therefore, a maximum of 2 out of every 5 Nanodiscs will contain a membrane protein assuming a perfect efficiency in incorporation.

After determining the proper amount of MP and MSP, the second key ratio is the proportion of supplemental synthetic lipid to MSP. Too many lipids lead to the formation of large aggregate species. Too few lipids cause poor formation of Nanodiscs, which leads to a polydisperse size exclusion chromatogram (Figure 3.3). For POPC, the optimal molar ratio for MSP1E3D1 Nanodiscs has been established previously as 130 POPC:MSP for Nanodiscs without membrane proteins.[28] However, the addition of detergent-solubilized lipids from the starting membrane and the displacement of lipids by the incorporated proteins lower the ratio of lipids that must be added. Thus, the optimal ratio of POPC to MSP will depend on the protein to lipid ratio in the starting membrane, the detergent extraction,[117] and the membrane protein to MSP loading ratio. Libraries were formed with a range of lipid ratios to determine the optimal value. Samples were prepared from the same detergent extract (1% OG) with a fixed amount of membrane proteins, 10 μg MP/nmol MSP. Each sample was analyzed by SEC and compared with a control sample of lipid-only POPC Nanodiscs. To account for the shift caused by the

increasing Stokes diameter, the control Nanodisc chromatogram was shifted to align the maxima. The sum of squared errors between the aligned control sample and each chromatogram showed the minimum difference and hence optimal lipid ratio at 90 POPC:MSP, about 70% of what is required for POPC-only Nanodiscs (Figure 3.4). Even at optimal lipid loading, a small shoulder is observed on a shifted Nanodisc peak (see Figure 3.2). This may be attributed to incorporation of protein complexes with large extracellular or cytosolic domains, which significantly increase the Stokes diameter of the Nanodisc.[118,119] In general, performing a pilot study similar to this for each new system to find the optimal ratio of lipid to MSP is advisable.

3.3.3 Analysis of the SMPL Proteome

To evaluate the degree to which the Nanodisc library mirrored the protein content of the starting membrane proteome, delipidated protein extracts were analyzed with SDS-PAGE from the starting membranes (lane B), detergent extracts (lane C), and SMPL (lane D) as shown in Figure 3.5. To avoid interference from MSP in the SMPL sample, Nanodiscs were captured on a Ni-NTA column. Membrane proteins were eluted by disassembling the Nanodiscs with cholate, leaving MSP bound to the column. Image analysis was performed to count and compare bands between lanes. The SMPL bands overlapped with 89% of bands in the detergent extract (25 of 28 bands) and 86% of bands in the raw membranes (25 of 29 bands). These data demonstrate that the SMPL contains a large percentage of the proteins present in the membrane proteome. It was also observed that 93% of bands in the detergent extract overlapped with bands in raw membranes (27 of 29 bands). This suggests that some of the proteins absent in the SMPL are lost due to incomplete detergent extraction, while others are efficiently solubilized but not efficiently inserted into Nanodiscs.

Although it is difficult to ascertain precise quantitative data from Figure 3.5, the intensities for many of the bands are similar from lane to lane. Comparing the peak intensities of matching bands reveals that on average they differ by around 15% from lane to lane. This suggests that the incorporation efficiency is roughly similar for many of the proteins. However, there are several bands, most notably bands 4 and 5, where the incorporation efficiency is significantly lower. Future studies will seek to determine the mechanism behind the quantitative differences in incorporation efficiency.

Prominent bands in the gel were excised and digested for mass spectrometric identification. Several bands were selected from the detergent and membrane lanes due to slightly higher levels of protein in those bands, which improved confidence in identification as seen in bands 4 and 5. The bands are annotated in Figure 3.5 and proteomic results are given in Table 3.1. Several outer membrane proteins were observed, including OmpA, OmpW, OmpC, Maltoporin, and BamA. OmpA and OmpW are both monomeric proteins while OmpC and Maltoporin form trimers in native membranes.[120] BamA is a larger outer membrane assembly factor with a significant extra-membrane domain.[121] These proteins demonstrate the successful incorporation of integral outer membrane proteins of a range of sizes.

In addition to outer membrane proteins, two inner membrane proteins were identified, the alpha subunit of ATP synthase and molecular chaperone DnaK.[122] The detection of ATP synthase is to be expected as purified ATP synthase was previously studied in Nanodiscs under similar sample preparation conditions.[123] Detection of these proteins demonstrates both the incorporation of inner membrane proteins and the incorporation of peripheral membrane proteins. These proteomic data suggest that SMPL Nanodiscs provide a faithful model of the membrane proteome in a soluble form useful for a range of novel biochemical analyses.

It is important to note that the SMPL is best considered a model of the starting membrane proteome rather than an exact duplicate. It is not expected that 100% of the proteins in the starting membrane will be functionally incorporated in the SMPL. As such, this approach could lead to false negatives and should not be used to exclude a particular protein. Other approaches to membrane protein solubilization, including detergent-based techniques, face the same challenge. However, the above results suggest that the SMPL contains a large percentage of the protein pool and serves as a useful *in vitro* model of the membrane proteome.

3.4 Conclusion

Nanodisc libraries offer a novel technique for solubilizing membrane proteomes. Although the specifics for SMPL formation will depend on the system of interest, the general protocol, optimization, and analysis techniques described in this chapter will guide future studies. Membrane proteins were extracted from *E. coli* inner and outer membranes and incorporated into SMPL Nanodiscs with different loading ratios. At a relatively high loading of membrane proteins, displacement of lipids by the incorporated membrane proteins and the presence of natural lipids from the membrane in the detergent extract caused the optimal lipid to MSP molar ratio to be significantly less than is required for empty Nanodiscs. SDS-PAGE and proteomic analysis of the library suggest that the Nanodisc library faithfully reflects the starting membrane proteome.

3.5 Figures and Tables

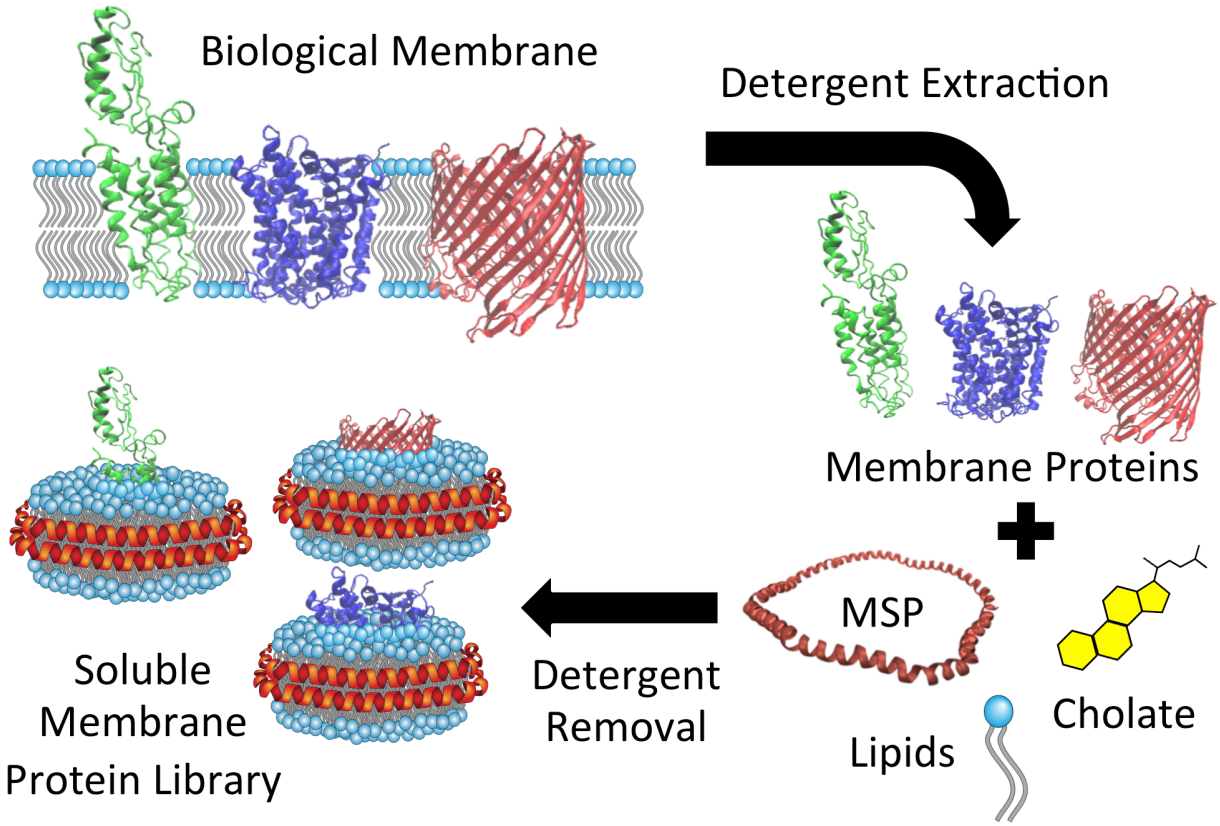


Figure 3.1: Schematic of SMPL formation. Membrane proteins are extracted from the membranes with detergent and added to a mixture of MSP, lipids, and cholate. As the detergents are removed, the components self-assemble into a Nanodisc library.

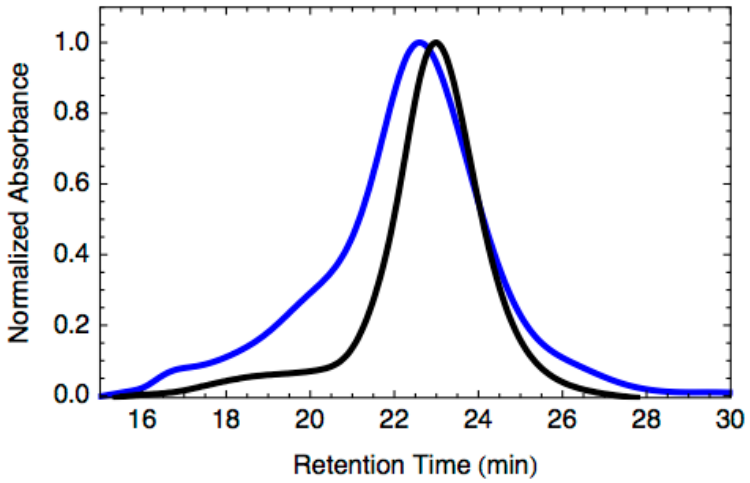


Figure 3.2: Size exclusion chromatogram for control Nanodiscs (*black*) and purified SMPL Nanodiscs (*blue*) made with a loading ratio of 10 μg MP/nmol MSP and a lipid ratio of 100 POPC:MSP.

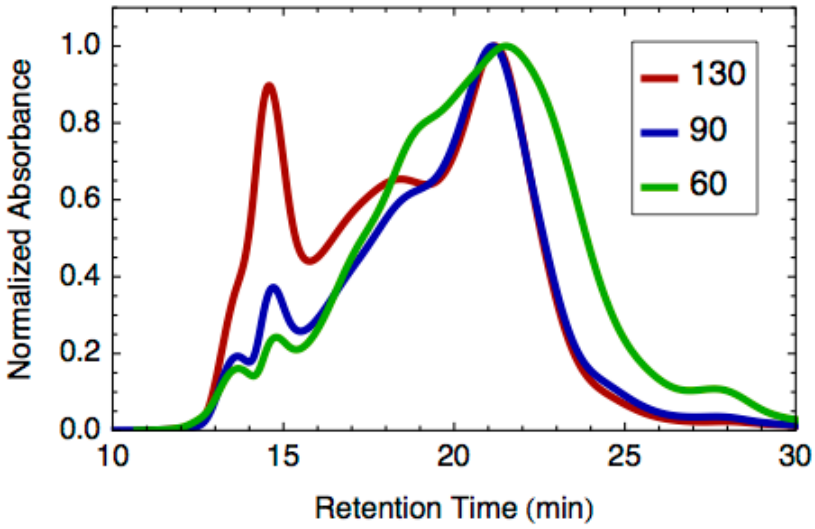


Figure 3.3: Size exclusion chromatogram of unpurified Nanodiscs following SMPL formation at 130 (*red*), 90 (*blue*), and 60 (*green*) POPC:MSP molar ratio. Large aggregate species are observed for at 130 POPC:MSP, and poorly-formed polydisperse Nanodiscs are formed at 60 POPC:MSP

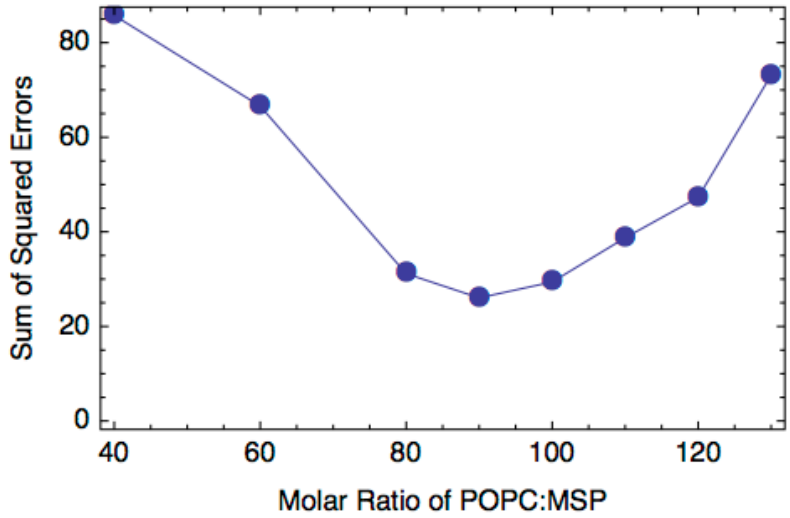


Figure 3.4: Optimization of POPC:MSP ratio for SMPL Nanodiscs made from 1% OG-solubilized membrane proteins at a loading ratio of 10 µg MP/nmol MSP with different amounts of lipid added. Unpurified reconstitution mixtures were analyzed by SEC. Chromatograms were aligned with a chromatogram of control Nanodiscs, and the sum of squared error was calculated. The optimal ratio is the minimum difference, 90 POPC:MSP

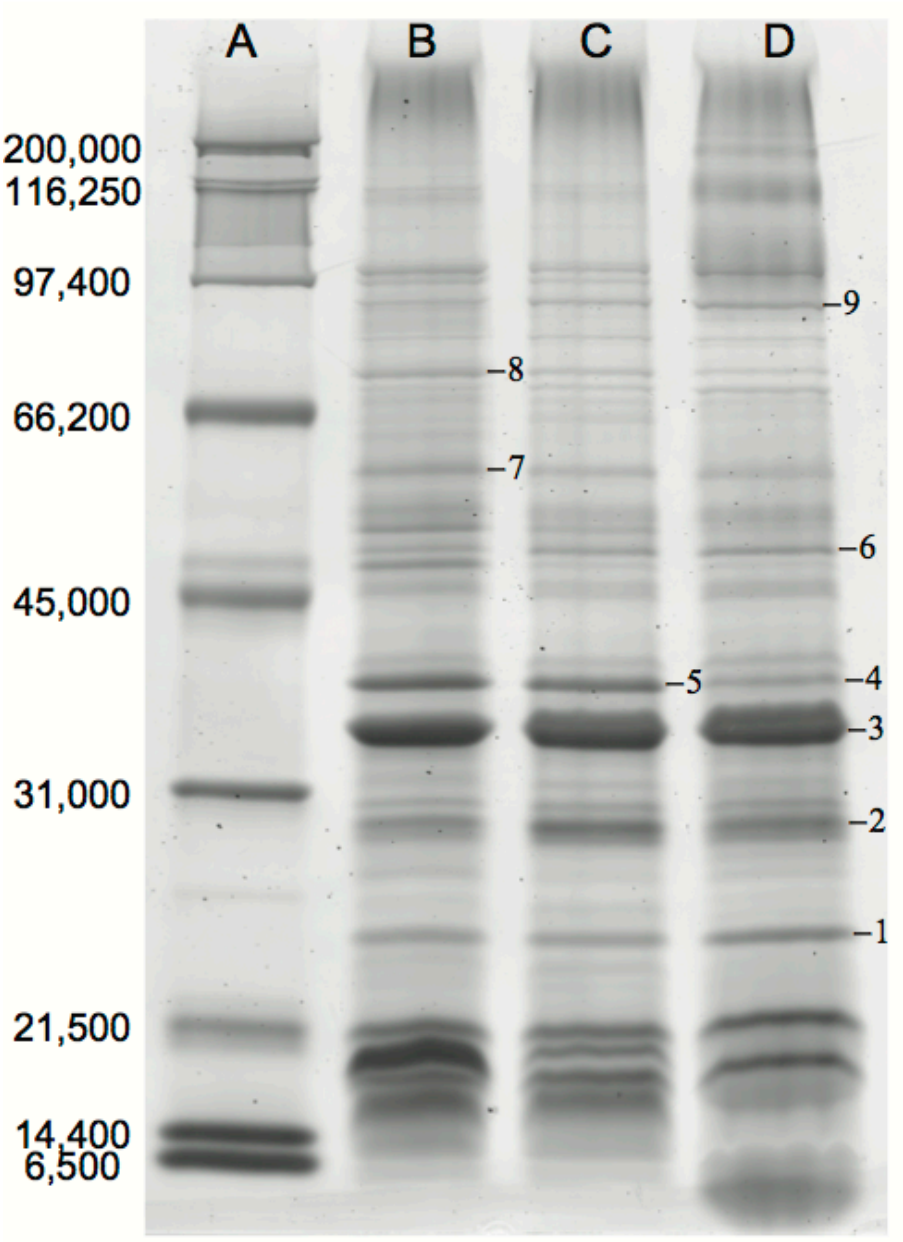


Figure 3.5: SDS-PAGE gel of protein extracts of the Nanodisc library (lane D) compared to the raw membranes (lane B) and detergent extracted proteins (lane C). Standards are annotated (in Da) in lane A. The SMPL was formed with a loading ratio of 10 µg MP solubilized in 1% OG per nmol MSP and a lipid ratio of 100 POPC:MSP. Bands 1-9 were excised and identified with mass spectrometry as given in Table 3.1.

Table 3.1: Proteomic identification of select bands from Figure 3.5 with proteomic statistics.

Band no.[a]	Protein Name	Accession no.[c]	Mascot Score	Mass (Da)	Sequence Coverage
1	Outer Membrane Protein W	OMPW_ECOLI	1958	22913	48%
2[b]	Outer Membrane Protein A (fragment)	gi|195940407	1578	28716	80%
3	Outer Membrane Protein A	OMPA_ECOLI	2901	37178	61%
4	Outer Membrane Protein C	OMPC_ECOLI	554	40343	53%
5	Outer Membrane Protein C	OMPC_ECOLI	3471	40343	91%
6	Maltoporin	LAMB_ECOBW	1402	49881	37%
7	ATP synthase subunit alpha	ATPA_ECOLI	1014	55188	40%
8	Chaperone protein DnaK	DNAK_ECOLI	975	69072	24%
9	Outer membrane protein assembly factor BamA	BAMA_ECOLI	970	90496	26%

[a] According to Figure 3.5.

[b] This OmpA fragment was found in the NCBI database but was not in the SwissProt database. Results are given for the NCBI database search.

[c] Accession numbers are given for SwissProt database except for band 2 which was determined using the NCBI NR database.

CHAPTER 4: ULTRA-THIN LAYER MALDI MASS SPECTROMETRY OF MEMBRANE PROTEINS IN NANODISCS

4.1 Introduction

Membrane proteins in Nanodiscs have been studied with several types of mass spectrometry as described in Section 1.4.2. There is great potential for the study of full-length proteins in Nanodiscs using mass spectrometry. In addition to functional assays such as the SAMDI assay described above,[77] interactions involving proteins complexes and heterogeneous populations of Nanodiscs could be probed in novel binding experiments. In general, precise values of protein molecular weights can be used to identify inhomogeneity in protein samples, the presence of post-translational modifications, or the efficacy of label attachment.[124-127] Mass spectrometry following limited proteolysis can give key structural information and has become important in identifying domains for crystallization.[128,129] Finally, post-ionization fragmentation of proteins can be used for investigation with top-down proteomics.[130,131] Nanodiscs offer the unique ability to perform these experiments on membrane proteins in a soluble, native-like lipid bilayer.

However, as observed in the SAMDI assay and in data presented here, conventional MALDI sample preparation techniques give weak membrane protein peaks and strong MSP peaks, which complicate the spectrum and overwhelm the signal observed from the membrane

---

Reproduced in part with permission from Marty, M. T.; Das, A.; Sligar, S. G. Ultra-thin layer MALDI mass spectrometry of membrane proteins in nanodiscs. *Anal. Bioanal. Chem.* **2012**, *402*, 721-729. Copyright 2012 Springer. The published version may be found online at http://link.springer.com/article/10.1007%2Fs00216-011-5512-3. Contribution of materials from Aditi Das is acknowledged.

protein of interest. Membrane proteins have been difficult to study using mass spectrometry due to their poor solubility in common solvents and the deleterious effects of many detergents on the spectra. Since lipids and MSP are generally present in Nanodiscs at least at a 65:2:1 lipid/MSP/membrane protein ratio, membrane proteins in Nanodiscs are in relatively low abundance and are in the presence of high lipid concentrations. There are several sample preparation methods that have been developed to improve detection of membrane proteins in detergent that could potentially be applied to Nanodisc samples.[124,132] However, sample preparation that involves liquid chromatography is generally more time and material intensive.

In this chapter, an ultra-thin layer MALDI method has been optimized for membrane proteins in Nanodiscs.[85] This method has been previously applied to MALDI of membrane proteins in detergent.[126,133,134] It relies on preparation of the sample plate surface with a thin layer of matrix, which acts as seed crystals to nucleate formation of homogenous polycrystalline matrix layer on the surface. The speed and simplicity of this method have led to its widespread adoption, especially as a partner to crystallographic studies of membrane proteins.[129]

The ultra-thin layer method was applied to membrane proteins in Nanodiscs, and nearly complete elimination of the MSP signal along with a dramatic enhancement of the membrane protein signal was observed. The method was tested on several structurally diverse proteins including cytochrome P450 3A4 (CYP3A4), which is monotopically embedded in the membrane; cytochrome p450 reductase (CPR), which is a peripheral membrane protein associated through a single hydrophobic transmembrane helix; and rhodopsin (Rho), which is a polytopic integral membrane protein (Figure 4.1). Further, this method was used to identify multiple proteins in a heterogeneous mixture of membrane proteins in Nanodiscs. Enhancement of membrane protein peaks and elimination of the scaffold protein allows fast and easy analysis

of modifications to proteins in Nanodiscs and opens the door for experiments involving structural studies, heterogeneous libraries of membrane proteins in Nanodiscs, and novel mass spectrometry assays.

4.2 Experimental Methods

4.2.1 Materials

Sinapinic acid (SA) was obtained from Sigma-Aldrich-Fluka and used without further purification, and α-cyano-4-hydroxycinnamic acid (4HCCA) was obtained from Sigma-Aldrich (St. Louis, MO) and recrystallized in ethanol. HPLC-grade methanol, isopropanol, and acetonitrile as well as 88% formic acid and LC/MS grade trifluoroacetic acid (TFA) were obtained from Fisher Scientific (Pittsburgh, PA). Water was purified with Millipore (Marlborough, MA) cartridges to 18.2 MΩ•cm.

POPC was obtained from Avanti Polar Lipids (Alabaster, AL), and octyl glucoside was obtained from Anatrace (Maumee, OH). Sodium cholate, Triton X-100, and Amberlite XAD-2 were purchased from Sigma Chemical (St. Louis, MO). Emulgen 913 was from Karlan Research Products (Santa Rosa, CA).

4.2.2 Protein Expression and Purification

CYP3A4, CPR, and rhodopsin were assembled into Nanodiscs using MSP1D1 as the membrane scaffold protein. MSP1D1 has been described previously in detail.[28] MSP1D1 with the polyhistidine tag removed is referred to as MSP1D1(-) and was used with CYP 3A4 and CPR Nanodiscs.

CYP3A4 with a pentahistidine affinity tag was expressed from the NF-14 construct in the pCWOri+ vector and purified as previously described.[30,119] Rat CPR was expressed in the

pOR262 vector and purified as previously described.[7] Bovine rhodopsin was purified by isolating rod outer segments from frozen bovine retina (SPCI Retina Inc.). Rhodopsin was purified from these rod outer segments on ConA-Sepharose (GE Healthcare) as previously described.[135]

4.2.3 Self-assembly of Nanodiscs Containing Membrane Proteins CYP3A4, CPR and Rhodopsin

The assembly of CYP3A4 and CPR Nanodiscs has been previously described in detail.[30,112,119] The assembly of rhodopsin Nanodiscs has been also been described previously.[35] The components used to self-assemble CYP3A4, CPR, and rhodopsin into Nanodiscs were MSP1D1, cholate-solubilized POPC, and purified membrane proteins initially solubilized in detergent. For CYP 3A4 and CPR, MSP1D1(-) was used. CYP 3A4 was initially solubilized in 0.1% (v/v) Emulgen 913, and CPR was initially solubilized in 0.1% (w/v) Triton X-100. For rhodopsin, MSP1D1 was used was used, and rhodopsin was initially solubilized in 90 mM octyl glucoside. Membrane proteins were typically concentrated to around 100 μM before being mixed with the other components. MSP was prepared as described above and concentrated to around 200 μM. POPC was dissolved in chloroform, dried under nitrogen, and put in a vacuum desiccator overnight to remove all residual chloroform. The dried phospholipids were then dissolved in a buffer containing 100 mM cholate to a lipid concentration of 50 mM and sonicated to ensure solubilization of the phospholipids.

Cholate-solubilized POPC, detergent-solubilized membrane protein, and MSP were combined in a molar ratio of (1:65:130:0.1) (MSP:POPC:cholate:membrane protein). Typically, the final concentration of the different components in the mixture were around: 15.3 μM membrane protein, 153 μM MSP, 10 mM POPC, 20 mM cholate, and residual amounts of

Emulgen 913, Triton X-100, or octyl glucoside. The excess of MSP in the assembly mixture ensures an excess of empty Nanodiscs to statistically favor incorporation of only one membrane protein molecule per Nanodisc. Thus, a single Nanodisc would consist of two MSP1D1 molecules, 130 POPC molecules, and one membrane protein molecule. This mixture was incubated on ice for 1 hour.

To initiate the self-assembly process, detergent was slowly removed from the mixture by 4 hours of incubation on an orbital shaker at 4 °C with 0.5-0.8 g of Amberlite XAD-2 per mL of solution. Following removal of Amberlite beads from the solution by centrifugation, Nanodiscs were purified from any lipid or MSP aggregates by size exclusion chromatography (SEC) on a Superdex HR 200 10/30 size exclusion column (Amersham–Pharmacia Biotech, Piscataway, NJ). Fractions containing Nanodiscs were pooled.

With rhodopsin and CPR, no further purification was performed to separate membrane protein-containing Nanodiscs from the excess lipid-only Nanodiscs. For CYP3A4, the Nanodiscs containing CYP3A4 were isolated on a nickel nitrilotriacetic acid (Ni-NTA) metal chelating column using the pentahistidine affinity tag on CYP3A4. Finally, all Nanodisc samples were concentrated to around 10 μM membrane protein concentration using a 10,000 Da molecular weight cut off centrifugal protein concentrator from Millipore.

4.2.4 MALDI Sample Preparation

For the dried-drop method of sample preparation, a matrix-saturated solution was prepared by adding solid matrix to 1:1 water/acetonitrile with 0.1% TFA and mixing thoroughly. Enough solid matrix was added so that some of the matrix remained undissolved, and the solid matrix settled to the bottom of the tube. Nanodisc samples were diluted 1:10 in the matrix-

saturated solution, and 1 μL was spotted directly onto a stainless steel 100-spot Voyager sample plate. The spot was allowed to dry in air.

The ultra-thin layer method relies on preparation of the sample plate with a thin layer of dried matrix.[126,133,134] The stainless steel 100-spot Voyager sample plate or ground steel 384-spot Bruker sample plate was washed thoroughly with multiple alternating methanol and water rinses. To prepare the ultra-thin layer solution, 150 μL of 1:500:500 (v/v/v) TFA/water/acetonitrile (TWA) was added to 10 mg of solid matrix. After thoroughly mixing at room temperature by repeated aspiration into a pipette tip and by vortexing, the TWA-matrix suspension was centrifuged at 14,000 rpm for 5 minutes to pellet the remaining solid matrix. The supernatant was carefully removed and diluted with 450 μL of isopropanol. This final ultra-thin layer solution was spread across the sample plate with the side of a pipette and allowed to dry. Typically, 25 μL of ultra-thin layer solution was enough to cover most of a 100-spot Voyager sample plate or a quarter or 384-spot Bruker sample plate. Finally, the dried matrix was gently wiped off the plate by a lint-free wipe, leaving a barely-visible matrix layer.

The Nanodisc matrix solution was prepared in a manner similar to the ultra-thin layer matrix solution. First, a 2:1:3 (v/v/v) formic acid/water/isopropanol (FWI) solution was prepared and allowed to sit overnight. Then, 150 μL of FWI solution was added to 10 mg of solid matrix. This suspension was mixed thoroughly by pipette aspiration and by vortexing. It was then centrifuged at 14,000 rpm for 5 minutes, and the supernatant was removed. Nanodisc samples were diluted 1:20 in this supernatant FWI-matrix solution, and 0.3 μL were spotted on the ultra-thin layer plate. After 10-15 seconds, a homogenous polycrystalline layer had formed across the spot, and the remaining solution was removed from the plate by aspiration through a vacuum line attached with a pipette tip. Each spot was washed for several seconds with a 2 μL drop of cold

0.1% TFA in water, which was also removed by aspiration. Both 4HCCA and SA matrices were explored, but SA was used in the majority of studies since it showed superior membrane protein molecular ion peaks.

4.2.5 MALDI-TOF Mass Spectrometry

MALDI-TOF mass spectrometry was performed on an Applied Biosystems Voyager-DE STR MALDI-TOF Mass Spectrometer operating at 25 kV accelerating voltage in linear positive ion mode with delayed extraction and a 337 nm nitrogen laser with 3 ns pulses. Laser power was optimized to suit each matrix and varied minimally from sample to sample. Spectra were averaged over 1000 shots and were analyzed, smoothed, and baseline corrected in Voyager Data Explorer 4.0.0.0 software.

Depth probing MALDI experiments and MALDI mass spectrometry imaging were performed on a Bruker UltrafleXtreme MALDI-TOF/TOF mass spectrometer operating with in linear positive ion mode with pulsed ion extraction. The proprietary smartbeam™-II laser was capable of varying repetition rates from 1-1000 Hz. Spectra were baseline corrected, smoothed, and analyzed in FlexAnalysis (Bruker Daltronics). MALDI imaging was performed with the FlexImaging software pack (Bruker Daltronics).

Two different depth probing MALDI experiments were performed. In the first experiment, the laser was rastered across the sample in a regular pattern with 150 μm steps, collecting just one laser shot at each raster point. After rastering across the sample once, the pattern was repeated in the same manner so that the laser fired on the same raster points a second time. The spectra from each pass were summed to give the first shot and second shot spectra. This is referred to as a first shot MALDI experiment.

Because the first shot MALDI experiment using MALDI imaging was relatively time intensive, a second technique was used to access deeper depths. In this second experiment, the laser was rastered over the sample in a random walk pattern. The number of shots taken at each specific raster point was changed to include 1, 3, 5 and 10. Spectra were then summed and compared based on how many shots the laser had taken at each raster point. The resultant spectra indicated the average composition of the first shot, shots one through three, shots one through five, and shots one through ten.

Coffee ring spots were formed in the same way as the optimized ultra-thin layer spots except that the solution was aspirated off the sample plate immediately after it had been spotted. To image the coffee ring spots, the laser was rastered across the image in 75 μm steps collecting 200 shots at each raster point at a 1 kHz laser firing rate. Spectra were baseline corrected and smoothed in FlexAnalysis and imaged in FlexImaging.

4.3 Results and Discussion

4.3.1 Comparing the Ultra-thin Layer Method and the Dried Drop Method for CYP3A4 Nanodiscs

The most common method of sample preparation for proteins and peptides is the dried-drop method. The dried-drop method involves simply mixing the analyte with matrix and spotting the mixture on the sample plate to dry. To test the applicability of the dried-drop method to membrane proteins in Nanodiscs, cytochrome P450 3A4 in Nanodiscs was analyzed using conventional MALDI sample preparation. Cytochrome P450 3A4 is the most abundant human P450 and is involved in xenobiotic metabolism. CYP3A4 is monotopically embedded in the lipid bilayer and has been extensively studied in Nanodiscs.[136] With the dried-drop method, strong MSP signal was seen at 22.0 kDa with MSP dimers and trimers appearing at 44.0 kDa and 66.0

kDa respectively (see Figure 4.2). Comparatively small CYP3A4 peaks were observed at 57.0 kDa and 28.5 kDa corresponding to the mono- and di-cation species. The strong signal from MSP and weak signal from CYP3A4 is problematic for analysis of the membrane protein inside the Nanodiscs.

To improve the membrane protein signal, the ultra-thin layer sample preparation technique, originally developed for membrane proteins in detergent,[133] was optimized for membrane proteins in Nanodiscs. The MALDI-TOF spectra of CYP3A4 in Nanodiscs using dried-drop method and ultra-thin layer method are compared in Figure 4.2. Applied to CYP3A4 in Nanodiscs, the ultra-thin layer method showed almost no detectable MSP signal and a roughly 2-4 fold signal enhancement of the CYP3A4 peaks.

Two different matrices were used in conjunction with the ultra-thin layer method to determine their utility with Nanodisc samples. Each matrix showed MSP elimination and enhanced CYP3A4 peaks. Similar to previous studies,[133] α-cyano-4-hydroxycinnamic acid (4HCCA) showed more polycationic species than sinapinic acid (SA) (data not shown). Multiply charged species are beneficial in studies where high mass accuracy is needed, as multiple ion peaks can be averaged to get more precise mass values. On the other hand, SA showed much better signal from the singly and doubly charged CYP3A4 but fewer species of higher charge. This matrix is useful for mixtures or other applications where simpler spectra or singly charged species are desirable. Because it showed better singly charged protein peaks, sinapinic acid was used in the remaining studies.

4.3.2 First Shot and Imaging MALDI to Understand MSP Elimination

Given its success in detergent-based systems, it was not surprising that the ultra-thin layer method improved the membrane protein signal. However, the discovery that the ultra-thin layer

method nearly completely eliminated the MSP signal was serendipitous and raised the question of the ultimate fate of the MSP. Several experiments were performed to characterize the spots formed by the ultra-thin layer method. In the first simple experiment, the laser was manually moved to probe various regions of the spot. It was observed that the CYP3A4 signal had a fairly homogeneous lateral distribution with few "hot spots." Moreover, MSP was not localized to any region of the spot.

To investigate the depth profile of the sample spots, MALDI experiments, including first shot MALDI, were performed utilizing the laser as a depth probe. Spectra were sorted based on the number of times a laser had fired on a specific location.[137] By examining how the mass spectra change as the laser probed different depths, these experiments showed the vertical distribution of protein within the polycrystalline matrix spot. In both experiments, there were no significant changes in spectra as the laser probed deeper into the spot. The distribution of CYP3A4 was vertically homogenous throughout the spot, and no MSP was observed throughout the sample. Thus, the enhanced membrane protein signal is not due to an upconcentration of membrane protein at the surface or in any other region of the spot, and the lack of MSP signal is not likely due to a sequestration within the matrix polycrystalline layer.

One important step in ultra-thin layer sample preparation is the removal of excess solution following the co-crystallization of matrix and protein on the ultra-thin layer. The solution is removed by vacuum aspiration before the sample dries completely. This step and the subsequent rinse with 0.1% TFA in cold water serve to remove salts, lipids, and other contaminants [133] and greatly improve the quality of the spectra. In the process of optimizing the method, it was observed that the amount of time given for the spot to crystallize before aspiration of the solution had significant effects on the MSP signal. When the spots were allowed to dry for

10 seconds or more before aspirating the remaining solution, the crystal layer looked very homogenous and showed almost no MSP signal across the spot.

However, if the solution was quickly aspirated off the surface, a coffee ring drying pattern was observed with a thicker layer of matrix around the edges and a thin matrix deposit in the middle. MALDI mass spectrometry imaging of these rapidly dried spots showed almost no MSP present in the thick layer around the ring (similar to the optimized ultra-thin layer spectra), strong MSP peaks in the thin deposits in the middle (similar to the dried-drop spectra), and a mixed spectra showing moderate MSP and membrane protein peaks in the region of the edge directly adjacent to where the vacuum aspirator removed the solution. The MALDI image of a coffee ring spot is shown in Figure 4.3 with the integrated intensity of the 57.0 kDa CYP3A4 peak in blue and the integrated intensity of the 22.0 kDa MSP peak in red. The region of purple near the top indicates the mixed spectra formed near the aspirator.

The heterogeneous coffee ring spots observed with fast drying by aspiration provide a model for understanding MSP elimination that is similar to previous models of differential protein detection.[138] The 2:1:3 formic acid/water/isopropanol solvent breaks up the Nanodisc and solvates the protein, lipids, and MSP. The ultra-thin layer on the surface of the sample plate forms a layer of seed crystals, which nucleates crystal formation on the surface. Because sinapinic acid crystals have hydrophobic faces,[139] a partitioning occurs between the hydrophobic matrix and the solvent. With longer drying times, MSP partitions into the solvent while the membrane proteins partition onto the growing polycrystalline film and are co-incorporated homogeneously as the solvent evaporates and the crystal layer grows. MSP remains in solution and is removed with the solution by aspiration. Any residual MSP is washed away with the TFA rinse.

Under conditions of fast drying, there is a brief period of time before aspiration begins where the partitioning observed with normal drying conditions occurs. In this short period of time, the membrane protein partitions into the coffee ring layer forming at the exterior of the drop. MSP remains partitioned in solution. Vacuum aspiration, however, causes much faster evaporation of the drop. Thus, MSP does not have time to partition freely into solution and becomes trapped in precipitating matrix crystals. Kinetic limitations cause the formation of crystals that resemble the dried-drop method more closely than the ultra-thin layer method. MSP deposits in this way in the center of the spot and over top of the existing coffee ring directly adjacent to the site of aspiration as the drop is pulled from the center, over the coffee ring, and into the aspirator.

4.3.3 Extension of the Ultra-thin Layer Method to Structurally Diverse Membrane Proteins and Mixtures

To demonstrate that the dramatic elimination of MSP and enhancement of membrane protein peaks is general for multiple types of membrane proteins, the ultra-thin layer method was applied to Nanodiscs containing membrane proteins of different sizes and membrane topologies. Cytochrome P450 reductase (CPR) is a membrane-associated redox partner with many P450 enzymes. Structurally, CPR is bound to the membrane by a single transmembrane helix. Thus, it is primarily a soluble protein with a small transmembrane anchor (Figure 4.1). Figure 4.4 shows the MALDI-TOF spectrum of CPR in Nanodiscs with the ultra-thin layer method. There are peaks at 77.7 kDa, 39.0 kDa, and 25.9 kDa corresponding to the mono-, di-, and tri-cation of the full-length protein. A triply charged dimer species appears at 51.4 kDa. Dimers also appear weakly in spectra from rhodopsin and CYP3A4.

The method was further tested on rhodopsin, a member of the G protein-coupled receptor family of integral membrane proteins. Rhodopsin is a polytopic transmembrane protein and is more completely embedded in the membrane than either CYP3A4 or CPR (Figure 4.1). Previously, strong MSP peaks and weak rhodopsin peaks were observed in SAMDI spectra of rhodopsin in Nanodiscs.[77] MALDI-TOF mass spectra of rhodopsin in Nanodiscs using the ultra-thin layer method showed rhodopsin peaks at 41.7 kDa and 20.9 kDa for the mono- and di-cation species with almost no MSP present (see Figure 4.4). Dimeric rhodopsin is also observed around 83 kDa. The successful application of the ultra-thin layer method to structurally diverse proteins ranging from integral transmembrane to monotopically embedded to membrane anchored proteins demonstrates the general applicability of this method for MALDI of membrane proteins in Nanodiscs.

One of the potential applications of MALDI mass spectrometry of Nanodiscs is in the identification of specific membrane proteins binding in a mixture or complex. While mass spectrometry of full-length proteins will not likely yield the specificity required to identify unknown proteins, it allows fast identification of known proteins from a heterogeneous mixture in experiments where multiple proteins are interacting. For heterogeneous populations of membrane proteins in Nanodiscs, MALDI with the dried-drop method will be severely hampered by strong MSP signal as the ratio of each protein to MSP will be smaller in mixtures. To examine the efficacy of the ultra-thin layer method on heterogeneous Nanodisc samples, mixtures were prepared by combining the CYP3A4, CPR, and rhodopsin Nanodisc samples described above. MALDI mass spectrometry using the ultra-thin layer method demonstrated that MSP peaks were suppressed in the mixture, and CYP3A4, CPR, and rhodopsin could all be detected in the spectrum (see Figure 4.5). These results demonstrate the ability to identify

multiple and diverse membrane proteins in Nanodiscs and open the door for future applications involving larger protein complexes.

4.4 Conclusion

This chapter detailed a method for studying membrane proteins in Nanodiscs using MALDI-TOF mass spectrometry. The dried-drop method of sample preparation showed strong signal from the membrane scaffold protein belt and weak signal from membrane proteins inside Nanodiscs. Using the ultra-thin layer method,[133] enhanced signal from membrane proteins in Nanodiscs and a nearly complete elimination of MSP signal was observed. These results have been demonstrated for a variety of membrane proteins in Nanodiscs, including mixtures of proteins. The ability to efficiently detect membranes proteins in Nanodiscs with MALDI mass spectrometry enables the development of future mass spectrometry experiments for functional and structural studies.

4.5 Figures

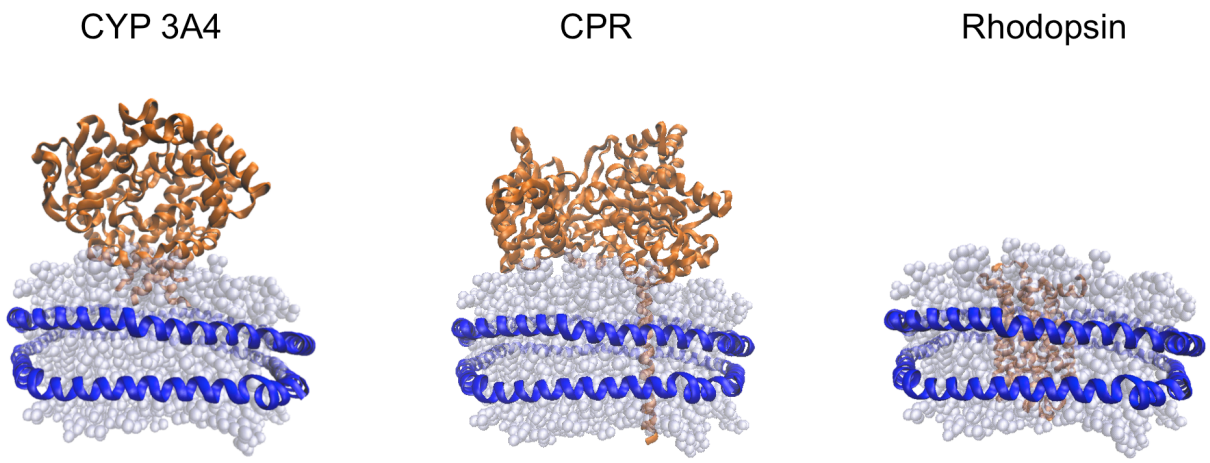


Figure 4.1: Model of CYP3A4, CPR, and rhodopsin in Nanodiscs. The two MSP molecules are shown in blue, proteins are shown in orange, and the POPC lipid bilayer is shown in a translucent light blue. CYP3A4 is monotopically embedded in the membrane, CPR is associated with the membrane through a single transmembrane helix, and rhodopsin is polytopically buried in the membrane.

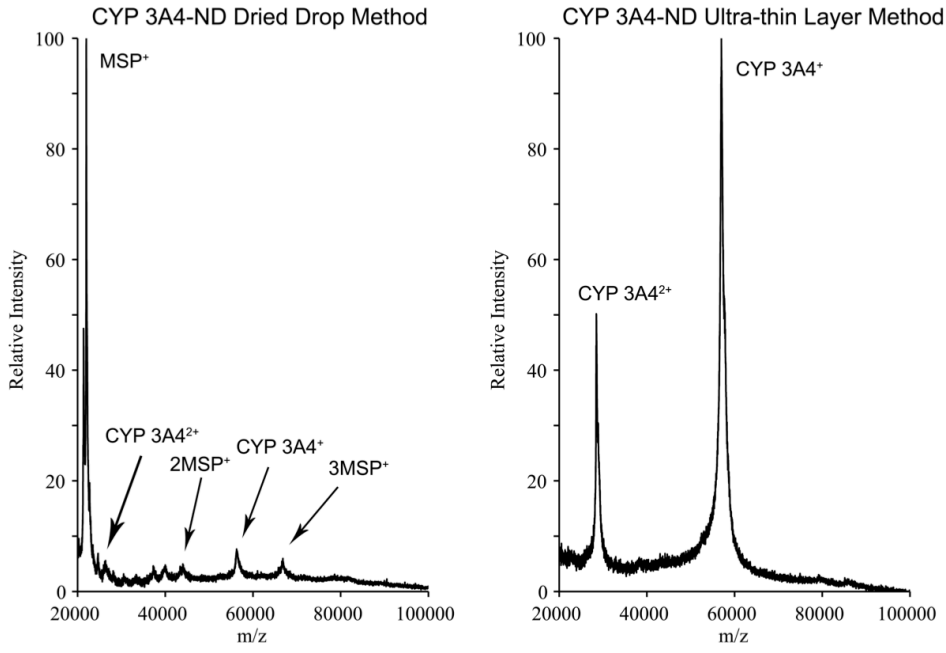


Figure 4.2: Comparison of the MALDI-TOF spectra with sinapinic acid matrix for CYP3A4 in Nanodiscs using the dried drop method (*left*) and the ultra-thin layer method (*right*). With the dried drop method, strong MSP peaks are observed with monomers, dimers, and trimers at 22.0 kDa, 44.0 kDa, and 66.0 kDa respectively. CYP3A4 peaks are relatively weak with peaks at 57.0 kDa and 28.5 kDa. With the ultra-thin layer method, MSP is absent, and the mono- and di-cation CYP3A4 peaks are enhanced.

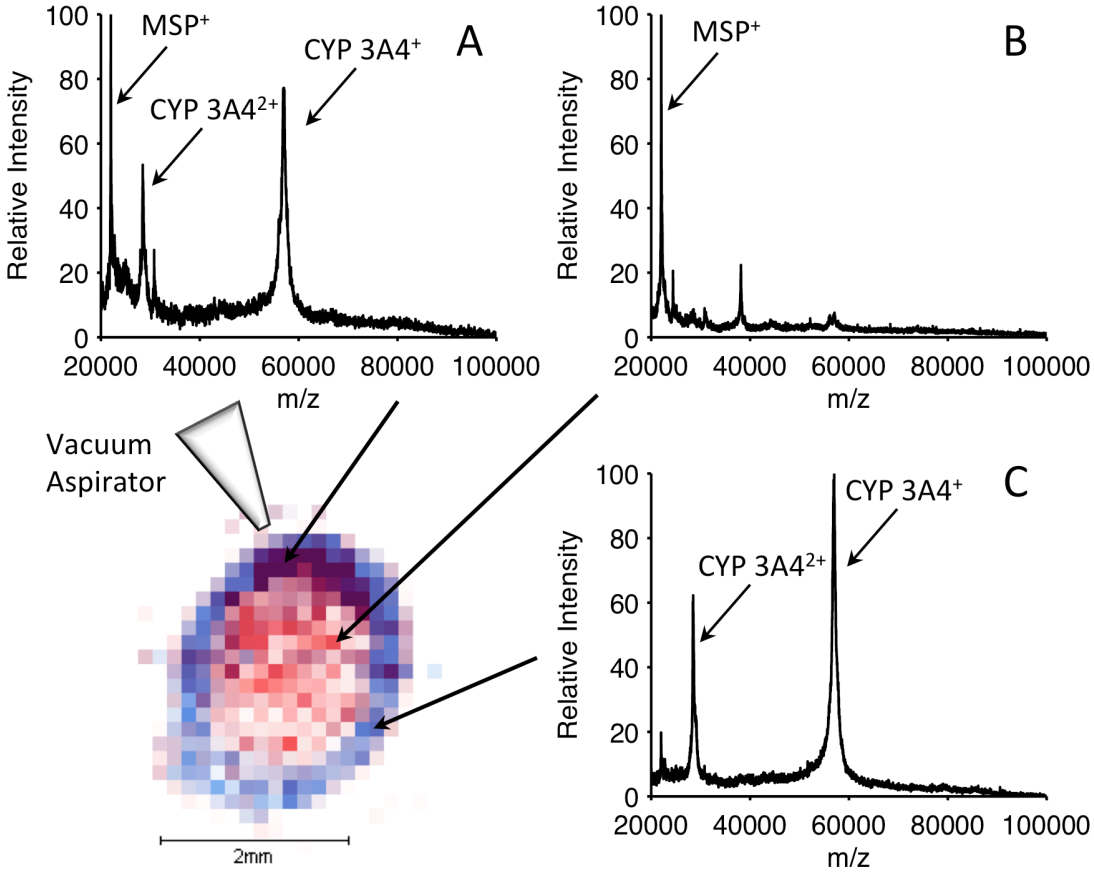


Figure 4.3: Mass spectra and MALDI mass spectrometry image of a rapidly-dried coffee ring spot of CYP3A4 in Nanodiscs using the ultra-thin layer method and sinapinic acid. In the region adjacent where the vacuum aspirator had suctioned the drop off the chip, a mixed spectrum is observed showing both MSP and CYP3A4 (*A*). In the middle, the MSP peak is strong, and CYP3A4 peaks are weak (*B*). Around the edge, CYP3A4 peaks are prevalent, and MSP is suppressed (*C*). The MALDI-MS image shows the integrated intensity of the CYP 3A4 peak at 57.0 kDa in blue and the integrated intensity of the MSP peak at 22.0 kDa in red. The image mirrors spectra *C*, *B*, and *A* with a blue CYP3A4 ring around the edge of the spot, red in the middle of the spot, and mixed purple adjacent to the aspirator.

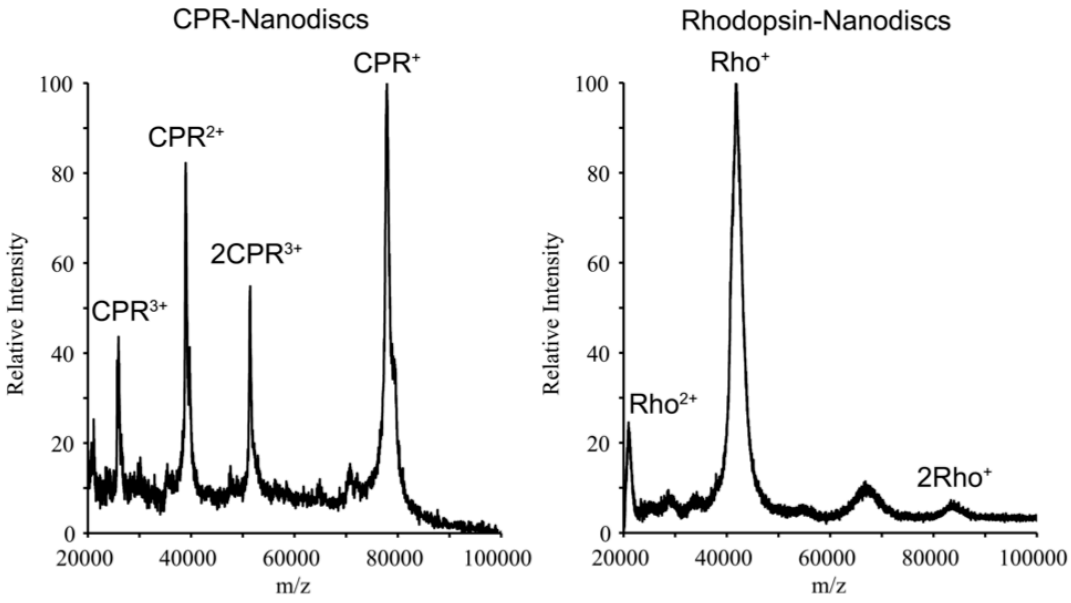


Figure 4.4: The MALDI-TOF mass spectrum of cytochrome P450 reductase in Nanodiscs using the ultra-thin layer method is shown on the *left*. Mono-, di-, and tri-cation peaks are observed at 77.7 kDa, 39.0 kDa and 25.9 kDa respectively. A dimer with three charges appears at 51.4 kDa. The MALDI-TOF mass spectrum of rhodopsin in Nanodiscs using the ultra-thin layer method is shown on the *right*. Mono-and di-cation peaks appear at 41.7 kDa and 20.9 kDa. Dimers appear around 83 kDa. An unidentifiable peak around 66 kDa may be MSP trimers or some other aggregate species.

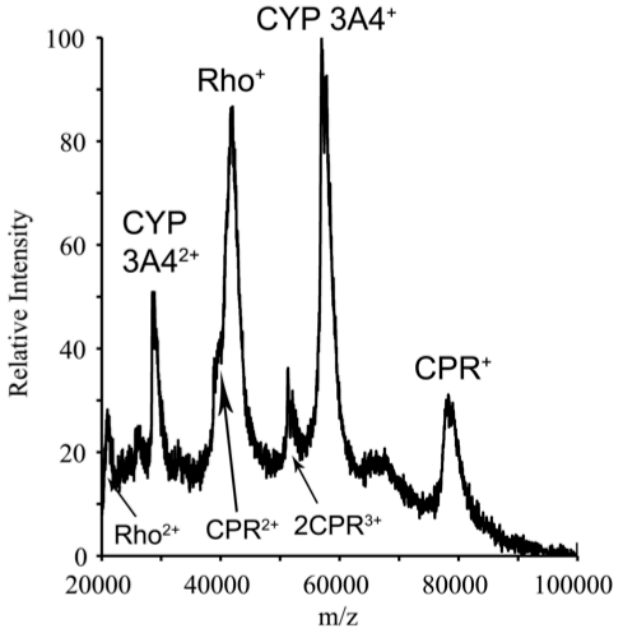


Figure 4.5: Mass spectrum of a mixture of CYP3A4 Nanodiscs, CPR Nanodiscs, and rhodopsin Nanodiscs. Peaks appearing in Figures 4.2 and 4.4 are all present, and MSP is still nearly absent despite representing a larger fraction of total protein.

CHAPTER 5: INTERFACING NANODISCS WITH SILICON PHOTONIC MICRORING RESONATORS

5.1 Introduction

As described in Section 1.4.1, Nanodiscs are highly useful for surface-based biosensor studies of biomolecular interactions involving membrane systems. However, previous applications of Nanodiscs to biosensor analysis have generally focused on a single membrane protein or lipid target with lipid-only Nanodiscs immobilized on a second channel as a control. Two-channel assays are useful for measuring interactions involving a single immobilized ligand, but most commercial SPR instruments are limited in their multiplex capabilities. With systems involving multiple membrane protein targets or a range of lipid bilayer compositions, biosensor technology with greater multiplex capabilities improves the analysis by decreasing consumption of precious material, reducing run-to-run variability, and increasing assay throughput.

Silicon photonic microring resonators are a biosensor platform that relies on arrays of individual micron-scale sensors. Dozens of microring sensors are patterned on an inexpensive silicon chip to provide a highly multiplexed biosensor technology. Microring resonators were previously used for studying protein-protein interactions,[140-142] quantifying proteins,[143-146] detecting nucleic acids,[147-149] and determining binding kinetics[87,150] in both single and multiplex assays. This chapter details the extension of the microring resonator platform to measuring

---

Reproduced in part with permission from Sloan, C. D.; Marty, M. T.; Sligar, S. G.; Bailey, R. C. Interfacing lipid bilayer nanodiscs and silicon photonic sensor arrays for multiplexed protein-lipid and protein-membrane protein interaction screening. *Anal. Chem.* **2013**, *85*, 2970-2976. Copyright 2013 American Chemical Society. The published version may be found online at http://pubs.acs.org/doi/abs/10.1021/ac3037359. This chapter includes significant contributions, including data and figures, from Courtney Sloan.

biomolecular interactions involving membrane protein and lipid targets by presenting a straightforward approach to immobilization of Nanodiscs on the biosensor surface.[86]

Nanodiscs were directly immobilized to the silica microring substrate via physisorption. Adsorption of lipids on silica is a simple method for attaching Nanodiscs on the surface but must account for differences in loading from different lipid head groups. Using the physisorption strategy, the binding of soluble proteins to Nanodisc-solubilized receptors allowed evaluation of concentration-dependent binding of soluble proteins to membrane-embedded receptors. Functionalization with four different Nanodisc systems provided a multiplexed assay of the binding specificity of interactions between soluble proteins and four separate Nanodisc species. This work represents the first application of the microring resonator biosensors to membrane-bound targets and a novel immobilization strategy for Nanodiscs.

5.2 Experimental Methods

5.2.1 Materials

Lipids 1-palmitoyl-2-oleoyl-*sn*-glycero-3-phosphocholine (POPC), 1-palmitoyl-2-oleoyl-*sn*-glycero-3-[phospho-L-serine] (POPS), 1,2-dipalmitoyl-*sn*-glycero-3-phosphocholine (DPPC), N-(biotinoyl)-1,2-dipalmitoyl-*sn*-glycero-3-phosphoethanolamine (biotin-DPPE), and 1,2-dimyristoyl-*sn*-glycero-3-phosphocholine (DMPC) were purchased from Avanti Polar Lipids (Alabaster, AL, USA). MSP1D1 was expressed and purified as described previously.[27,28] Streptavidin was purchased from Thermo Fisher Scientific Inc. (Rockford, IL, USA). An antibody to human cytochrome P450 3A4 was purchased from Santa Cruz Biotechnology, Inc. (Santa Cruz, CA, USA). Annexin V, cholera toxin B subunit, Amberlite XAD-2 hydrophobic beads, and all other chemicals were purchased from Sigma Aldrich (St. Louis, MO, USA). Buffers were prepared with 18 MΩ deionized water and sterile filtered prior to use.

5.2.2 Nanodisc Self-assembly and Purification

Preparation of CYP3A4 Nanodiscs is described in Sections 4.2.2 and 4.2.3. Procedures for Nanodisc preparation with POPS,[71] GM1,[36] and biotin-DPPE[75] have been previous described in detail and follow the same general protocol outlined in Section 2.2.2. Briefly, for mixed lipid systems of POPC:POPS, DMPC:GM1, and DPPC:biotin-DPPE, lipids were combined in the appropriate ratios by mixing their chloroform stocks prior to drying and resuspension in sodium cholate. Cholate-solubilized lipids were combined with scaffold protein MSP1D1. Next, detergent removal was accomplished with Amberlite XAD-2 beads. Nanodisc samples were purified via a Superdex 200 prep grade column (1.6 x 30 cm). The concentration of Nanodisc stock solutions was measured by the MSP absorbance at 280 nm.

5.2.3 Chip Design, Instrumentation, and Data Analysis

Microring resonator instrumentation and sensor chips were obtained from Genalyte, Inc. (San Diego, CA) and have been described previously.[145,151] Arrays of silicon photonic microrings were fabricated of silicon oxide substrates. Each 6×6 mm microchip contained 32 microrings, each 30 μm in diameter, with adjacent linear waveguides. Input and output diffractive grating couplers at the end of the linear waveguides allow independent measurements to be made at each ring using a tunable cavity diode laser centered at λ=1560 nm. Light is coupled from the linear waveguide into the microring only at wavelengths that travel an integer number of wavelengths around the ring. This resonance condition is given by: $m\lambda=2\pi r n_{eff}$ where, m is an integer, r is the microring radius, and n_{eff} is the effective refractive index sampled by the optical mode. Biomolecular binding at the ring surface cause a change in local refractive index that is measured as a shift in the resonance wavelengths in units of Δpm. The magnitude of the wavelength shift is directly proportional to the amount of bound analyte. Solution is flowed over the surface through

a custom-built microfluidic chamber that features channels defined by a 0.007 inch thick Mylar gasket (RMA Laser, El Caljon, CA, USA). Net shifts were quantified at saturation of the Nanodisc or protein sample.

5.2.4 Microchip Functionalization

Chips were cleaned with a fresh piranha solution of 1:3 30%H_2O_2:H_2SO_4 for 30 s, rinsed with water, and dried with nitrogen. (Caution! Piranha solutions are dangerous and react explosively with trace quantities of organics.) Nanodiscs were immobilized on the microchip substrate by flowing Nanodisc solution through 1-, 2-, or 4-channel microfluidic gaskets.[145] Nanodisc solutions were diluted to 250 or 500 nM and allowed to adsorb for 10 minutes or until saturation was observed. The chips were blocked by flowing 2% bovine serum albumin (BSA) solution to prevent nonspecific binding to the silica surface. Following blocking, soluble proteins were flowed across the sensor surface. A flow rate of 10 μL/min was used for all steps.

5.3 Results and Discussion

5.3.1 Nanodisc Immobilization on Microring Resonator Biosensors

There are a number of methods for immobilizing Nanodiscs to biosensor surfaces.[36] As discussed in Section 1.4.1, conventional methods rely on modification of the surface to introduce immunocapture agents, nickel-chelation sites, or reactive groups that covalently attach to the Nanodiscs. These modifications to the surface are necessary, as the biosensor surfaces in SPR or localized surface plasmon resonance do not have any native affinity for Nanodiscs. Other surface-based analysis techniques such as atomic force microscopy[27] have utilized direct physisorption of phospholipids on silica as a surface attachment strategy. Silica has a strong affinity for phospholipids, and Nanodiscs generally lie flat with the bilayer parallel to the

surface.[27,58,152] Although microrings resonators are fabricated as silicon waveguides on a silica substrate, exposure of silicon to air and piranha solution leads to formation of a thin layer of silica on the surface ideal for deposition of Nanodiscs.

To test the direct immobilization Nanodiscs on the microring resonator surface, Nanodiscs containing POPC and a mixture of POPC and POPS were flowed across separate channels of the sensor array. Surface deposition on microrings was detected as a shift in resonance wavelength measured in Δpm. As shown in Figure 5.1, a shift in the resonant wavelength consistent with a layer of Nanodiscs on the surface[153] demonstrated immobilization of Nanodiscs on the microring resonator surface by direct adsorption. Even after switching to a blank buffer solution (marked by ** in Figure 5.1), Nanodiscs remained bound to the surface at a constant level, demonstrating the tight binding to the surface.

To determine whether Nanodiscs adsorbed on the surface were viable for monitoring specific interactions, binding of annexin V was monitored for the channels containing POPC and POPC:POPS Nanodiscs. Annexins interact with membranes through calcium ions that bridge between binding sites on the proteins and anionic lipids such as POPS.[154-158] Binding of annexin V was only observed on microrings functionalized with Nanodiscs that contained anionic POPS lipids (Figure 5.1). Switching the buffer to calcium-free PBS buffer immediately caused dissociation of the bound annexin V from the POPC:POPS Nanodiscs, demonstrating the calcium-dependence of this interaction. These data establish the utility of direct adsorption of Nanodiscs on the microring resonator array as an effective strategy for immobilization of lipids for binding assays.

One interesting observation from this simple two-channel assays is the differential loading between Nanodiscs with POPC and POPC:POPS. To further investigate this effect, a

four-channel assay was used to investigate the loading of Nanodiscs as a function of POPS content. As shown in Figure 5.2a and 5.2b, loading decreased as the POPS content increased from 0 to 50%. These data suggest that the electrostatics of the Nanodiscs affect adsorption on silica. Nanodiscs containing only POPC (a neutral lipid) are slightly negatively charged due to the MSP. Addition of anionic lipids further decreases the charge.[42] Because silica has negatively charged moieties at the neutral pH used in this study,[159] the microring surface may exert a repulsive force against anionic lipids in the Nanodiscs, leading to a lower affinity for the silica surface.

Binding of annexin V to immobilized Nanodiscs with variable POPS content was monitored in a four-channel assay. The net shift at 10 μg/mL of annexin V is shown in Figure 5.2c. Differences in loading of Nanodiscs lead to a decrease in net annexin binding at high POPS levels. However, normalization of binding response to Nanodisc loading demonstrates a clear trend towards increased annexin V binding at higher POPS levels (Figure 5.2d), as previous studies have shown.[75]

5.3.2 Concentration-dependent Binding of CTB to GM1 Nanodiscs

After establishing the ability to functionalize microring resonators with POPS Nanodiscs, another prototype system, glycolipid GM1 and cholera toxin B (CTB), was used to test the concentration dependence of binding. GM1 is a ganglioside glycolipid that binds the pentameric B subunit of the AB_5 cholera enterotoxin.[160,161] The GM1-CTB interaction has been previously studied in Nanodiscs with SPR,[36] microcantilevers,[75] and native mass spectrometry.[76] Nanodiscs containing 5% GM1 were immobilized in one channel, and control DMPC Nanodiscs were immobilized on a second channel. As opposed to POPS, GM1 did not alter the loading level relative to DMPC Nanodiscs, so normalization of CTB binding was not required. As shown in

Figure 5.3, increasing concentrations of CTB bound linearly to the GM1 Nanodisc channel over the range of concentrations tested here. It is important to note that the complex cooperative binding of CTB to GM1 precludes kinetic interpretation of these data. Cooperativity from the five binding sites on CTB or other potential instrumental factors could lead to the sigmoidal association curve and relatively large error at higher concentrations.[86] In any case, binding of CTB to GM1 Nanodiscs demonstrates the ability to quantitate interactions with Nanodisc-embedded targets.

5.3.3 Multiplexed Assay of Membrane Protein and Lipid Binding

Two key advantages of the microring resonator platform over other biosensor technologies are its low cost chips and easy multiplexability. Each microring represents a separate sensor, and dozens of rings can be arrayed on the chip. To test the multiplex capabilities of the microring resonator technology, a prototype array of four separate Nanodisc systems was immobilized on a single chip using a four-channel gasket.[141] Three of the four systems contained Nanodiscs spiked with a specific lipid species, POPS, GM1, or biotin-DPPE. The fourth system contained a monotopic membrane protein, cytochrome P450 3A4. After immobilization of the four species by direct adsorption, the surface was blocked with BSA. Soluble binding partners of the Nanodisc-embedded targets, annexin V, CTB, streptavidin, and anti-CYP3A4, were sequentially flowed across all channels of the chip to probe for specific and nonspecific interactions. As seen in Figure 5.4, the soluble partners bound to POPS, GM1, biotin-DPPE, and CYP3A4 respectively with little off-target binding. The orthogonal binding to four separate Nanodisc-embedded targets demonstrates the utility of the microring resonator biosensors for multiplexed detection of biomolecular interactions involving membrane systems.

5.4 Conclusion

This chapter detailed interfacing Nanodiscs with the microring resonator biosensor platform using direct adsorption on the silica surface. Immobilization of Nanodiscs by direct adsorption offers a simple and rapid attachment strategy without the need for modifying the surface or the Nanodiscs. After correcting for difference in immobilization rates, binding of a fixed concentration of annexin V to POPS Nanodiscs scaled with POPS content. In a related assay, binding of cholera toxin B to a fixed ratio of GM1 in Nanodiscs was directly proportional to the solution concentration of CTB. These two assays demonstrated the utility of the microring resonator platform to quantify the interaction of soluble proteins with Nanodisc-embedded targets, both with a variable concentration of soluble protein and with an array Nanodiscs of varying lipid content. The multiplexability of the microring resonator platform was utilized to simultaneously examine interactions between four Nanodisc systems, biotin-DPPE, POPS, GM1, and CYP3A4, and four sequential soluble binding partners, streptavidin, annexin, cholera toxin, and an anti-CYP3A4 antibody. Each soluble protein bound to the anticipated partner with minimal nonspecific binding to the other channels. This fusion of two technologies, Nanodiscs and microring resonators, represents important progress towards multiplexed examination of membrane interactions.

5.5 Figures

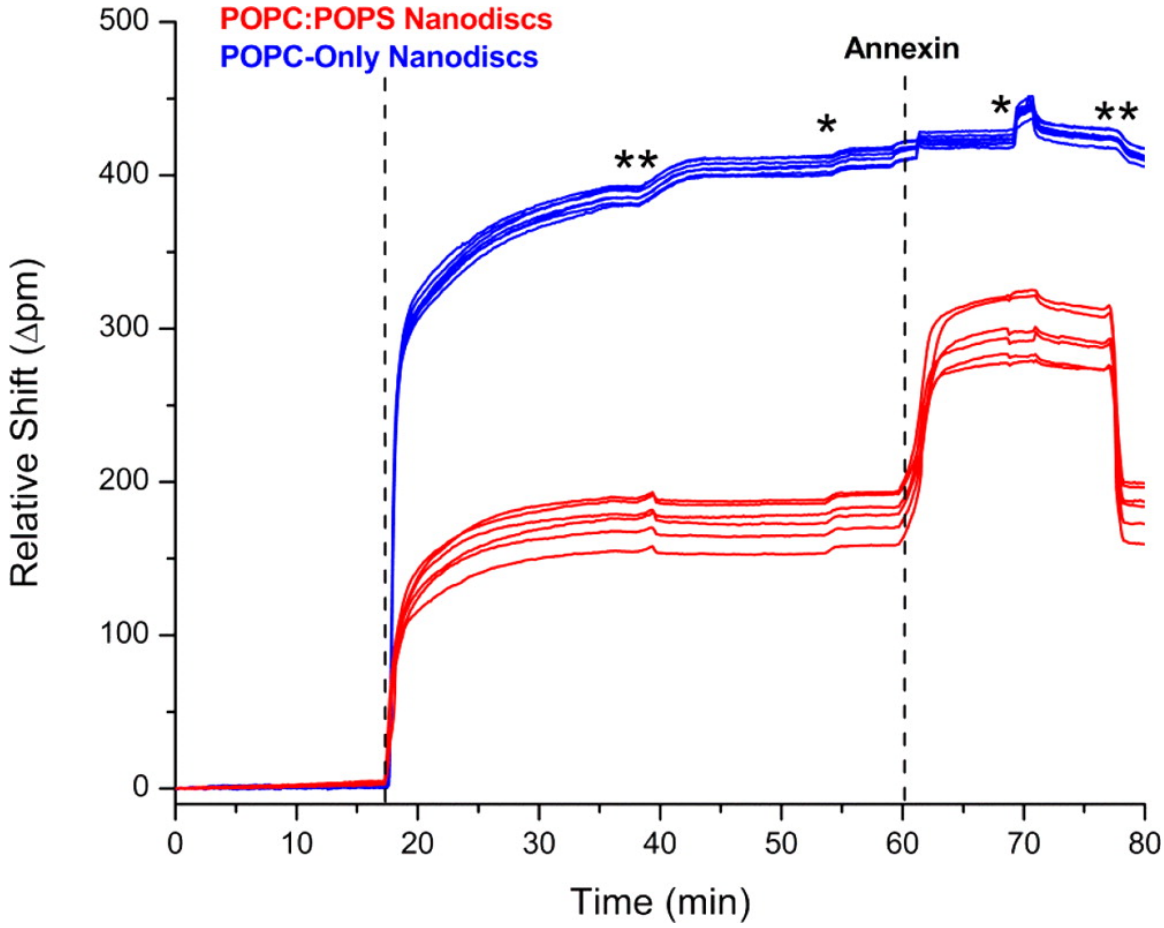


Figure 5.1: Direct immobilization of POPC (*blue*) and 50/50 POPC:POPS (*red*) Nanodiscs on the microring resonator surface. Dashed lines indicate the introduction of Nanodiscs at 18 minutes and 10 μg/mL annexin V at 60 minutes. Immobilization is observed for both species, although higher levels of immobilization are observed for POPC Nanodiscs. Binding of annexin is observed primarily on microrings with POPS-containing Nanodiscs. Introduction of a calcium-free PBS buffer causes rapid dissociation of annexin form the immobilized POPS Nanodiscs. Asterisks indicate a buffer change to either PBS (**) or to HEPES-Ca^{2+} buffer (*).

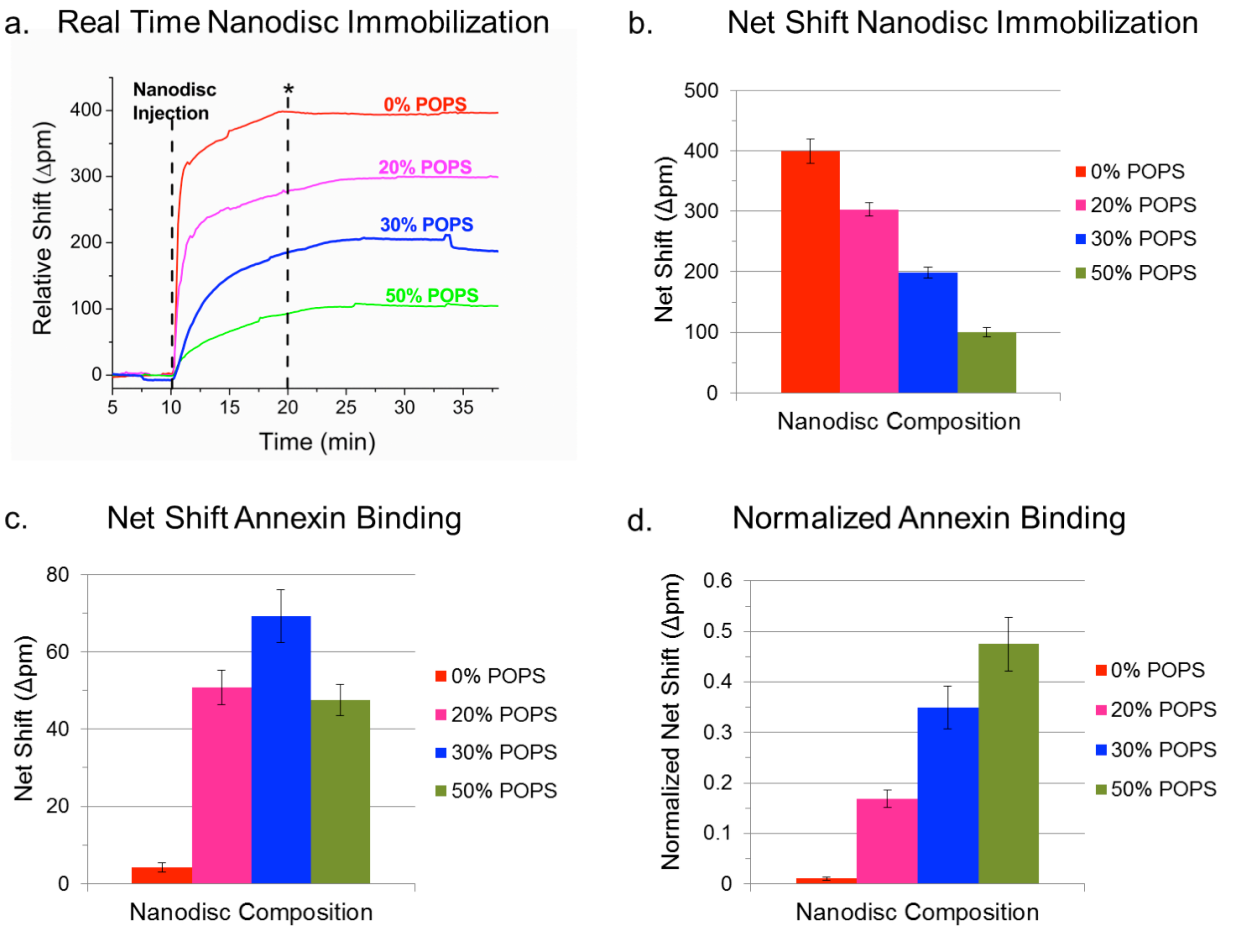


Figure 5.2: Nanodiscs with increasing amounts (0-50%) of POPS have lower loading capacity on microring resonators as observed in real-time binding curves (*a*) and net shift at saturation (*b*). Total binding of annexin depends on both the POPS content and amount of Nanodiscs loaded (*c*). After normalizing annexin binding to Nanodisc loading, an increase in annexin binding with increasing phosphatidylserine content is observed (*d*). Average net shifts and standard deviations are calculated based on the average of the signal over five minutes at saturation for three separate experiments, each with five individual sensor rings.

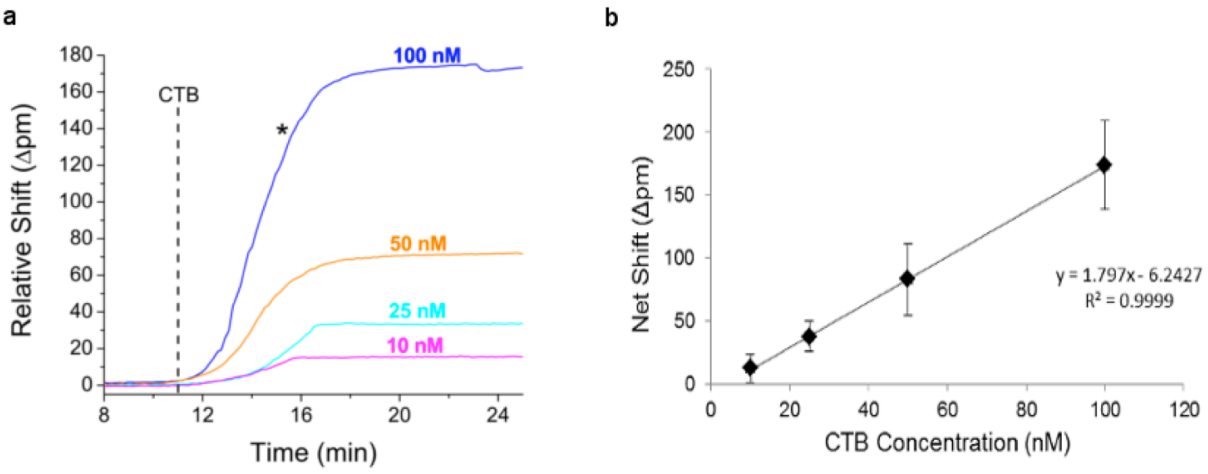


Figure 5.3: Binding of CTB at various concentrations to Nanodiscs with 5% GM1 content. Data is shown from representative microring sensors (*a*) and for average net shift (*b*). A linear increase in net shift is observed with increased CTB concentration. Averaged data represents 5 different microchips, approximately 18 individual microrings per concentration. Error bars are presented as one standard deviation.

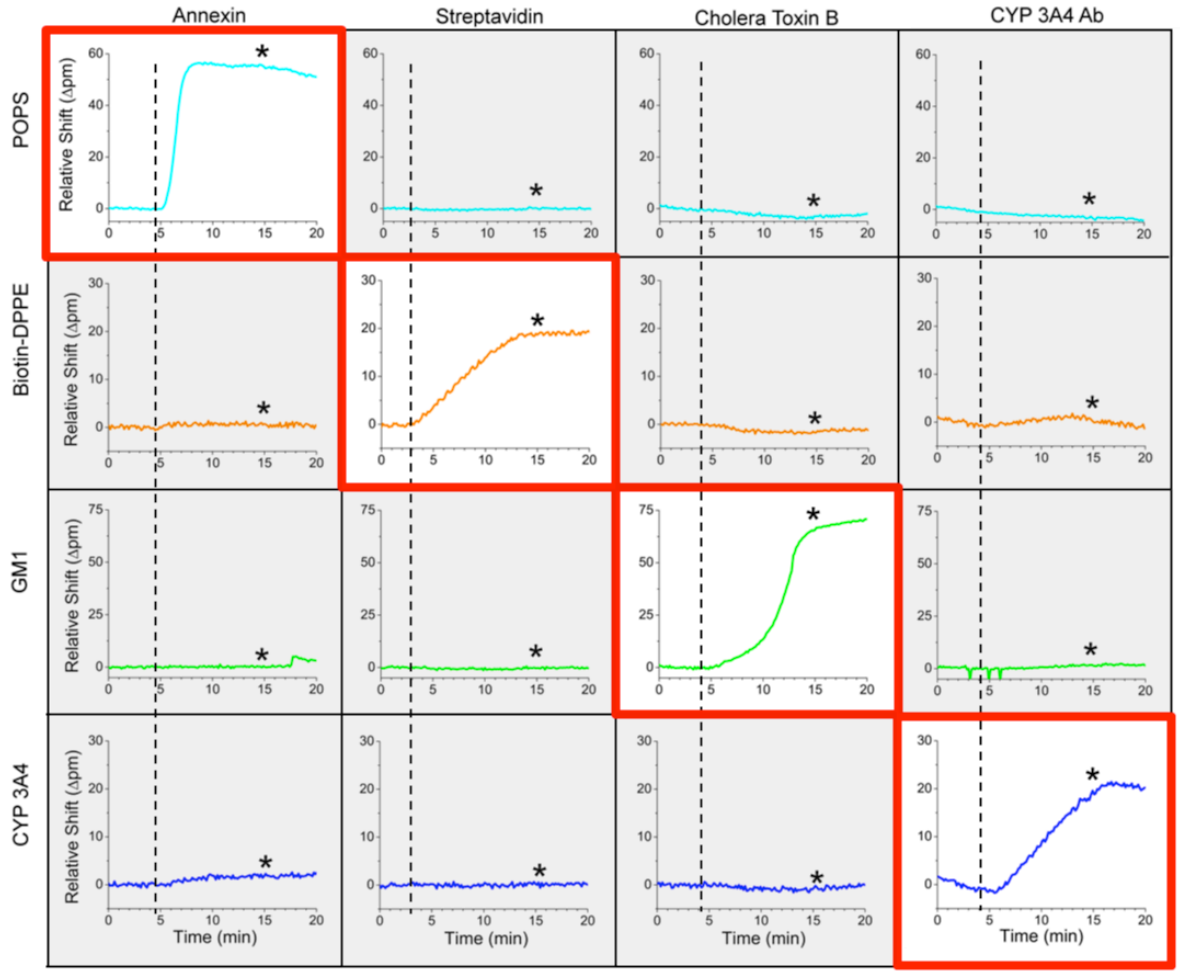


Figure 5.4: Multiplexed assay of four orthogonal Nanodisc systems with minimal off-target binding. For simplicity, a representative microring is presented in each row. Each row represents a separate parallel channel functionalized via direct adsorption with Nanodiscs containing 30% POPS, biotin-DPPE, GM1, and CYP3A4. Each column exhibits the binding response with sequential flowing of annexin, streptavidin, CTB, and anti-CYP3A4 in parallel across the all four channels. Dashed lines indicate sample introduction, and asterisks indicate the switch back to buffer.

CHAPTER 6: NONLINEAR CONCENTRATION GRADIENTS FOR KINETIC EXPERIMENTS EMPLOYING MICRORING RESONATORS

6.1 Introduction

Refractive index-based biosensors have become widely used for determining the kinetic rates of biomolecular interactions. Although the optical phenomena are distinct, the experimental design and data analysis for surface plasmon resonance (SPR),[162-165] localized surface plasmon resonance,[166] photonic crystal,[167] and optical microring resonator biosensors[141,151] are all similar. The success of these methods in measuring kinetic rates has been driven by the ability to monitor binding in real-time without the need for spectroscopic or enzymatic labels.

Typical kinetic experiments involve immobilization of a biomolecule on the biosensor surface. Analyte solution flows across the surface, and binding is monitored over time by measuring the change in refractive index within the evanescent field near the sensor surface. Kinetic experiments usually employ a stepwise titration of analyte concentrations. A constant concentration of analyte is injected for a defined period of time in the association phase, followed by the injection of a blank buffer solution to monitor the dissociation phase. The cycle of association and dissociation is repeated at multiple concentrations. Data from the concentration steps are then fit globally using numerical integration of the rate equations for a given model. Various linearization strategies can also be employed in data analysis.[168,169]

Reproduced in part with permission from Marty, M. T.; Sloan, C. D.; Bailey, R. C.; Sligar, S. G. Nonlinear analyte concentration gradients for one-step kinetic analysis employing optical microring resonators. *Anal. Chem.* **2012**, *84*, 5556-5564. Copyright 2012 American Chemical Society. The published work may be found online at http://pubs.acs.org/doi/abs/10.1021/ac300478f. Contributions of microring resonator data from Courtney Sloan are gratefully acknowledged.

The conventional stepwise titration approach has several limitations. In order to repeat the analysis at multiple concentration levels, the surface is typically regenerated before each injection. These multiple regeneration steps increase the total analysis time, consume more material, and can lead to run-to-run variability, as precise loading of the immobilized biomolecule is often difficult to achieve. Multiple regenerations are also particularly problematic for multiplexed assays where the surface is more complex.

In cases where it is difficult or impossible to regenerate the surface after each analysis, several different methods may be used to measure kinetics on a single surface by performing the titration in parallel or series. Bravman *et al.* have described the use of the ProteOn XPR 36 array SPR biosensor where the surface functionalization is performed orthogonal to a six-channel flow cell.[170] Thus, each loaded surface is split into six regions that are simultaneously and separately addressed by six concentration steps. Although this method demonstrates the utility of one-shot parallel kinetic experiments for multiplexed measurements, it is limited by the complex instrumentation associated with addressing the chip in orthogonal directions.

A titration series in which the surface is not regenerated after each association and dissociation cycle may also be used.[171] This method has been widely adopted, as it does not require additional instrumental components. A recent variation on the titration series method described by Rich *et al.* is known as a FastStep injection.[172] This method utilizes a SensiQ Pioneeer SPR instrument with a dual syringe pump system that is able to mix analyte solution and buffer during the injection to generate defined dilutions or gradients. A FastStep injection uses the syringe mixer to increase the concentration from low to high in discrete steps. As the concentration is increased, only the association phases are monitored. The dissociation is finally

measured by injecting buffer after the highest concentration step. These series methods have greatly increased the throughput of kinetic experiments.

In addition to parallel and series titrations, which utilize step concentration titrations, Shank-Retzlaff and Sligar demonstrated that a constantly increasing linear analyte gradient can be used to extract accurate kinetic rates and affinities in a single step.[173] The analyte gradient method offers many of the same advantages as the FastStep method in that kinetic experiments can be performed quickly, in a single step, and by preparing only a single analyte solution. Numerical simulations showed that the linear gradient method is applicable across a wide range of kinetic rates. It can be analyzed with the two-compartment model[174,175] to account for mass transport as well as a model for heterogeneous binding sites. The linear analyte gradient method was experimentally tested by measuring the binding of cytochrome *c* with cytochrome b_5 using a custom-built SPR instrument. A linear concentration gradient was generated by a straight-walled gradient maker and a High Pressure Liquid Chromatography (HPLC) pump.

This chapter expands the theory and application of analyte gradient methods as a one-step method for kinetic experiments.[87] A simple and scalable non-linear gradient maker has been designed to generate precise concentration gradients. This nonlinear gradient maker is more amenable to microfluidic systems than the gradient maker and HPLC pump previously used. Numerical simulations demonstrate that nonlinear gradients of different curvature offer the same capabilities as linear gradients over a wide range of kinetic rates. Furthermore, mass transport in nonlinear gradient systems can be modeled using both the two-compartment model and a temporally adjusted one-to-one interaction model. This nonlinear gradient instrumentation and theory is readily applicable to a variety of different biosensor platforms.

The nonlinear gradient maker was implemented with the microring resonator array biosensor platform.[151] Microring resonators are refractive index-sensitive silicon photonic devices comprised of microfabricated rings arrayed on a single chip (see Chapter 5). Light couples into the microrings from adjacent linear waveguides at a particular resonant wavelength. As biomolecules bind to the microring surface, the local refractive index changes, which is detected as a shift in the resonant wavelength. The chip architecture positions thirty-two individually addressable rings, eight thermal controls and twenty-four active rings, sequentially along a U-shaped flow cell (see Figure 6.1).

Microring resonators have previously been used for conventional kinetic analysis[141] as well as titration series.[150] This chapter expands the utility of this platform by providing the first report of "single shot" kinetics on microring resonators. The analyte gradient method was applied to the binding of cancer biomarker prostate specific antigen (PSA) to an anti-PSA antibody, which is attached to the microring surface by a DNA tag. Of the twenty-four active sensor rings, twelve are left intentionally blank (non-DNA functionalized) and serve as controls for the assay, allowing background corrections to the average of the binding curves from the twelve functionalized rings. However, different ligands can be attached to subsets of these rings for multiplexed measurements as previously demonstrated.[150] This multiplexable sensor surface combined with the single run kinetics will facilitate future high-throughput kinetic studies of biomolecular interactions.

6.2 Experimental and Theoretical Methods

6.2.1 Nonlinear Gradient Maker Design

The design for a nonlinear gradient maker is adapted from previous designs[176] to facilitate easy instrumentation with microfluidic systems. A schematic is shown in Figure 6.1.

This nonlinear gradient maker is based on a two-compartment system. An analyte solution with concentration M is placed in the analyte reservoir compartment. A peristaltic pump with flow rate r pumps solution from the analyte reservoir to the mixing compartment. Because solution is constantly removed from the analyte reservoir, it is important to have enough volume in the analyte reservoir to complete the experiment. The mixing compartment contains a blank buffer solution of volume V and is stirred by a small stir bar. Solution is pumped from the mixing compartment to the instrument at the same rate r that solution is pumped into the mixing compartment. Although the schematic depicts two peristaltic pumps for clarity, both tubes were fed through the same peristaltic pump. This both reduces the number of components and ensures that the rates to and from the mixing compartment are equal. Both compartments consisted of 1.5 mL microcentrifuge tubes with Teflon tubing for fluid delivery.

The concentration of the mixing compartment over time, $C_G(t)$, is described by the ordinary differential equation:

$$\frac{dC_G(t)}{dt} = \frac{rM - rC_G(t)}{V} \tag{6.1}$$

where M, r, and V are defined above. Equation 6.1 can be analytically solved by separation of variables to yield:

$$C_G(t) = M\left(1 - e^{-\frac{rt}{V}}\right) \tag{6.2}$$

Thus, the output of the nonlinear gradient maker is determined by three independent variables, the flow rate r, the mixing compartment volume V, and the concentration of analyte in the reservoir M. Each of these variables can be easily adjusted to define the curvature and slope of the gradient profile.

To test the nonlinear gradient maker prototype, the analyte reservoir was filled with 10X Dulbecco's Phosphate Buffered Saline (PBS) (Sigma, St. Louis, MO), and a defined volume of deionized water was added to the mixing compartment. The flow rate was measured by determining the mass of water pumped over a period of time. The concentration term *M* was measured by introducing the PBS solution directly over the microrings and measuring the refractive index change in units of picometer shift (Δpm), the shift in the resonant wavelength of the microring resonator. The predicted gradient profile was calculated in units of Δpm by inputting the measured *V*, *r*, and *M* into Equation 6.2. The experimental response was measured by flowing the output from the gradient maker over the microring resonators and measuring the Δpm shift. Responses were tested for mixing volumes ranging from 250-1000 μL and flow rates ranging from 5-20 μL/min.

6.2.2 Numerical Simulations

Simulations were used to generate analyte gradient binding curves with known kinetic rates. Similar to previous studies,[173] programs developed with Mathematica 8.0.4 numerically integrated a two-dimensional partial differential equations (PDE) model. This two-dimensional PDE model was derived from Glaser[177] as expanded by Myszka *et al.*[174] It accounts for diffusion parallel to the flow, the *x*-direction, and perpendicular to the surface, the *y*-direction, as well as a parabolic flow profile and is given by:

$$\frac{\partial C}{\partial t} = D\left(\frac{\partial^2 C}{\partial x^2} + \frac{\partial^2 C}{\partial y^2}\right) - 4vy(1-y)\frac{\partial C}{\partial x} \tag{6.3}$$

where *C* is the analyte concentration in mol/L, *t* is time in seconds, *v* is the average fluid velocity in cm/s, and *D* is the diffusion constant in cm^2/s.

Boundary conditions were included to model conditions at the four walls of the virtual flow cell. It was assumed that analyte does not diffuse out the back of the flow cell, where $x=l$ and l is the length of the flow cell, and that analyte does not diffuse out of the top of the flow cell, where $y=h$ and h is the height of the flow cell. Thus,

$$\frac{\partial C(t,l,y)}{\partial x} = 0 \tag{6.4}$$

$$\frac{\partial C(t,x,h)}{\partial y} = 0 \tag{6.5}$$

Fluid flowed into the flow cell at $x=0$ with a concentration equal to the gradient concentration given by Equation 6.2:

$$C(t,0,y) = C_G(t) \tag{6.6}$$

Finally, the binding kinetics of the surface were assumed to be first order governed by:

$$D\frac{\partial C(t,x,0)}{\partial y} = \frac{\partial \Gamma_{bound}}{\partial t} = k_a C(t,x,0)(\Gamma_{tot} - \Gamma_{bound}(t,x)) - k_d \Gamma_{bound}(t,x) \tag{6.7}$$

where $C(t,x,0)$ is the concentration directly above the surface, $\Gamma_{bound}(t,x)$ is the total number of binding sites in mol/cm^2 as a function of time and position in the flow cell, Γ_{tot} is the total number of binding sites in mol/cm^2, k_a is the association rate in $M^{-1}s^{-1}$, and k_d is the dissociation rate in s^{-1}.

The microring resonator flow cell has a height of 175 μm and a width of 500 μm with the 30 μm diameter microrings situated in the middle of the channel,[151] so any concentration differences along the width should be negligible. Although experiments were performed using a U-shaped flow cell,[153] the flow cell length was modeled as a 5 mm linear path. The flow cell was divided into a 34×34 grid, and concentration was calculated at each point on the grid over time using Equations 6.3−6.7. Unless stated differently, the diffusion constant was set to 1×10^{-6} cm^2/s,

the flow rate was set to 10 μL/min, the mixing volume was set to 500 μL, the total number of binding sites was set to 6×10^{-13} mol/cm^2, and flow cell height and length were set to 175 μm and 5 mm. Diffusion constants within an order of magnitude of this range showed very similar results. However, diffusion constants that were several orders of magnitude smaller, simulating very viscous solutions, showed much larger mass transport effects that limit the method.

The reservoir concentration was typically set to 10-25 times the equilibrium dissociation constant K_D so that the binding approached saturation at the end of the association phase. As a general guideline, it is best to ensure that the maximum concentration of the gradient is at saturating conditions at the end of the association phase so that the full range of appropriate concentrations is covered by the analyte gradient. Although it is easy to accomplish saturating conditions in systems with prior knowledge of the dissociation constant, some estimation will be required in unknown experimental systems. A pilot study is recommended to establish an appropriate estimation.

Numerical integration was performed over 7500 seconds with a time step of 0.01 seconds. The gradient concentration profile was allowed to run for 2500 seconds and was then set to zero molar to monitor the dissociation phase. The binding curves at each of the interior thirty-two grid locations were assumed to equal the response from the thirty-two microrings. The data from the thirty-two binding curves was averaged to form one binding curve that was then fit to extract kinetic rates. All thirty-two curves can be fit individually and show similar results to the averaged curves. However, fitting all individual curves greatly increased computation time. Alignment of the individual binding curves before averaging was also evaluated to correct for spatial offsets between the individual sensors. This was performed by simply shifting each binding curve until it achieved maximum overlap with the first curve.

6.2.3 Kinetic Models

Kinetic rate constants were extracted from the simulated binding curves by fitting the association phase to the one-to-one interaction model or the two-compartment model and fitting the dissociation phase to a simple exponential decay. The one-to-one model assumes that the concentration of analyte at the surface is identical to the gradient concentration and that the binding is first order on the surface. This model is governed by an ordinary differential equation given by:

$$\frac{d\Gamma_{bound}}{dt} = k_a C_G(\Gamma_{tot} - \Gamma_{bound}) - k_d \Gamma_{bound} \tag{6.8}$$

where C_G is given by Equation 6.2 in mol/L, k_a is the association rate in M^{-1}, and k_d is the dissocation rate in s^{-1}. Γ_{bound} and Γ_{tot} are the amount of analyte bound to the surface and the total number of binding sites respectively. Both are given in mol/cm^2 for simulations and in Δpm for experiments.

The two-compartment model also assumes first order binding at the surface but adds an extra layer of complexity. Here, the flow cell is divided into two regions, the flowing region and a stagnant region. The concentration in the flowing region is assumed to be equal to the gradient concentration input. Analyte diffuses between the flowing region and the stagnant region with a rate k_m. Analyte in the stagnant region can diffuse back into the flowing region or bind to the surface. This leads to a system of ordinary differential equations:

$$\frac{dC_s}{dt} = \frac{1}{h}(-k_a C_s(\Gamma_{tot} - \Gamma_{bound}) + k_d \Gamma_{bound} + k_m(C_G - C_s)) \tag{6.9}$$

$$\frac{d\Gamma_{bound}}{dt} = k_a C_s(\Gamma_{tot} - \Gamma_{bound}) - k_d \Gamma_{bound} \tag{6.10}$$

where C_s is the concentration in the stagnant layer, k_a is the association rate in $M^{-1}s^{-1}$, k_d is the dissociation rate in s^{-1}, k_m is the mass transport rate in cm/s, C_G is gradient concentration given by Equation 6.2 in mol/L, and h is the theoretical height of the stagnant layer. Γ_{bound} and Γ_{tot} are respectively the amount of analyte bound to the surface and the total number of binding sites as described above.

The dissociation phase can be modeled as a simple exponential decay. Assuming $C_G(t)=0$, Equation 6.8 becomes a simple ordinary differential equation, which solves to:

$$\Gamma_{bound}(t) = \Gamma_{\max} e^{-k_d t} \tag{6.11}$$

where k_d is the dissociation rate in s^{-1}. Γ_{bound} and Γ_{max} are respectively the amount of analyte bound to the surface and the total number of occupied sites at the start of the dissociation, $t=0$, and have units described above.

6.2.4 Data Fitting

For the experimental data, binding curves from the active rings were corrected by subtracting the average of the control rings as well as correcting for a constantly decreasing baseline of 0.5 pm/min due to antibody falloff.[150] Baseline corrected curves were normalized to correct for differences in antibody loading. Several minutes were discarded from the start of the dissociation phase to account for nonzero concentration in the flow cell. Figure 6.2 and 6.3B demonstrate this fall time before the concentration is truly zero in the dissociation phase. The fall time depends on instrumental parameters such as flow rate and on the diffusion constant of the analyte. Rather than trying to explicitly calculate the delay or to model this effect, the part of the dissociation curve that appeared to be nonexponential decay, which was roughly the region before the inflection point (see Figure 6.7 as an example), was truncated. This fall time represents an instrumental limitation for systems with fast dissociation times. Finally, association

and dissociation curves from active rings were averaged. Averaging both reduces computation time and lowers the noise, allowing for a more precise fit. However, it is possible to fit each active ring individually. The median values from these individual fits are very close to the fit from the average curve, but the confidence interval is larger.

Theoretical and experimental binding curves were fit to the models described above with a custom program in Mathematica 8.0.4. The general data fitting strategy employed numerical integration of the models to generate modeled curves and calculate chi-squared values.[169,173,178] The association and dissociation phases were fit globally using either the one-to-one model or the two-compartment model for the association phase and the exponential decay model for the dissociation phase. With theoretical data, the first 20 seconds of the dissociation was discarded to remove the fall time introduced by mass transport.

For both theoretical and experimental data, the reservoir concentration, mixing volume, and flow rate were manually input to calculate the gradient concentration profile. An iterative Monte Carlo routine was used to adjust the k_a, k_d, k_m, and Γ_{tot} to minimize the chi-squared values. Initial values were randomly generated across a range of values and evaluated. Preliminary tests demonstrated that Γ_{tot} values fit to within 1% of actual values in theoretical system, so Γ_{tot} values were manually input for theoretical binding curves to lower the computation time. However, Γ_{tot} was fit as an independent variable for the experimental data. Since each experiment was designed to saturate, the initial estimate for Γ_{tot} was the maximum picometer shift (Δpm) observed at saturation. Equilibrium constants were calculated as $K_D=k_d/k_a$.

The height of the stagnant layer (*h)* has previously been shown to have no influence on extracted association and dissociation rates.[173,174] The only parameter influenced by the value of h is k_m. h is therefore set as one in order to keep units consistent depending on the data set being

analyzed. For simulated systems, h was set to 1 mol/cm^2/M=10^3 cm. For the microring resonator data, h was set to 1 Δpm/M. k_m values are reported in terms of k_m/h.[174]

Due to the nonlinear nature of the model equations, confidence intervals on extracted kinetic rates were calculated by determining F-values for a combination of k_a, k_d, k_m, and Γ_{tot} values.[179] Confidence intervals are recorded as the maximum and minimum values for each variable that were under the critical F-value. All ranges are reported in parentheses at the 95% confidence interval.

6.2.5 Reagents and Materials

Purified human phosphate specific antigen (PSA) and monoclonal mouse anti-human PSA antibody (clone 5G6) were purchased from Meridian Life Science, Inc. (Saco, ME). Custom DNA oligonucleotides were synthesized by Integrated DNA Technologies (Coralville, IA) and contained a 5' terminal amino group attached via a 6-carbon chain (5AmMC6). Succinimidyl 4-formylbenzoate (S-4FB), 3-N-((6-(N'-Isopropylidene-hydrazino))nicotinamide) propyltriethoxysilane (HyNic Silane), succinimidyl 6-hydrazinonicotinamide acetone hydrazine (S-HyNic), and antibody-oligonucleotide conjugation kits were purchased from SoluLink (San Diego, CA).

Zeba spin filter columns and Starting Block were purchased from Pierce (Rockford, IL). Vivaspin molecular weight cutoff filters (50,000 and 5000 Da MWCO) were obtained from GE Healthcare (Waukesha, WI). Aniline was purchased from Acros Organics (Geel, Belgium). Phosphate buffered saline, pH 7.4 (PBS, Dulbecco's formulation) was made from 10X stock solutions (Sigma Aldrich, St. Louis, MO) for all microchip assays. The full 10X concentration was employed for salt gradient experiments. PBS with 0.05% Tween-20 (PBST) was made by

adding Tween-20 to standard PBS buffer. All buffers were degassed under vacuum sonication before use in microchip assays. All other reagents were purchased from Sigma Aldrich.

6.2.6 Instrumentation and Chip Functionalization

Ring resonator optical scanning instrumentation, software, and chips were obtained from Genalyte, Inc. (San Diego, CA) and have been described previously.[151] More details may be found in Section 5.2.4. Microchip functionalization procedures including DNA functionalization and conjugation of DNA-antibodies to the chip surface have also been detailed previously.[150]

Briefly, microchips were cleaned with piranha solution, rinsed with water, and dried with N_2. Chip surfaces were prepared for silane functionalization by a 30 min sonication in 100% ethanol and subsequent N_2 drying. Chips were then spotted with a 1 mg/mL HyNic Silane solution in 95% ethanol/5% N-dimethylformamide for 30 min at room temperature, followed by a 20 min sonication in 100% ethanol and N_2 drying.

Single stranded DNA, specifically strand M, (AAA AAA AAA AGT CGA GGA TTC TGA ACC TGT) was functionalized with S-4FB according to manufacturer's instructions and immobilized on a HyNic Silane functionalized microchip surface via a Nano eNabler spotting system from BioForce Nanosciences (Ames, IA). DNA strands were loaded onto the microchip surface at a concentration of at least 100 μM in a 1:1 mixture of 100 mM PBS, pH 6.0 and dimethyl sulfoxide. Following functionalization with DNA, the chips were stored in Starting Block at 4° C until use, and prior to loading DNA-antibody conjugates on the chip surface, the chips were soaked in PBST for ~20 min.

Following the PBST soak, DNA functionalized chips were then loaded into the flow cartridge and fluidically addressed by a U-shaped Mylar gasket (Scarpati Technical Services/RMS Laser). Solution delivery to the microchip surface employed a Teflon cartridge

top with fluid access holes, attached to an 11 Plus syringe pump (Harvard Apparatus, Holliston, MO) that was operated in withdrawal mode. M'anti-PSA-5G6 was loaded onto the chip surface at a concentration of ~5μg/mL in PBST by flowing antibody solution over the chip surface for ~5 min, allowing the M strand on the chip to base pair with the M' strand that was previously conjugated to the anti-PSA antibody (described below). The antibody loading was completed by flowing PBST across the chip surface.

Anti-PSA-5G6 was functionalized with S-HyNic Silane per the manufacturer's instructions. The modified antibody was then mixed with S-4FB modified DNA (specifically strand M', AAA AAA AAA AAC AGG TTC AGA ATC CTC GAC) and allowed to react overnight at 4°C. The DNA-antibody conjugate (M'anti-PSA-5G6) was then purified using a Superdex 200 10/300 GL column on an AKTA HPLC, both from GE Healthcare (Waukesha, WI). Conjugate concentrations were then determined using a NanoDrop UV-vis absorbance system (ThermoFisher Scientific, Wilmington, DE).

6.2.7 Analyte Gradient Delivery

The gradient maker described above pumped fluid across the sensor surface via the same U-shaped gasket that was employed for antibody immobilization (see Figure 6.1) using a P625/10K.133 miniature peristaltic pump (Instech, Plymouth Meeting, PA). Tubes were prefilled with the appropriate solutions to eliminate delay due to fluid flow. Concentrated PSA was added to the analyte reservoir, and a defined volume of PBST was added to the mixing compartment. All runs were monitored in real-time and allowed to proceed until saturation conditions were met. Once the binding curve appeared saturated, the inlet from the mixing compartment was switched to buffer. PBST flow was maintained until PSA dissociation was near completion.

6.3 Results and Conclusions

6.3.1 Design and Testing of Nonlinear Gradient Maker

A key component of the analyte gradient method is the accurate and reproducible creation of a gradient concentration profile. Although previous studies utilized a straight-walled gradient maker and HPLC pump,[173] a system was designed that was more compatible with small sample volumes and microfluidic flow cells. Many commercial linear gradient makers, such as the straight-walled gradient maker, operate on the principle of a two-compartment system. One compartment, the reservoir, contains a concentrated analyte solution. The reservoir flows into the mixing compartment, which initially contains only buffer. The mixing compartment is stirred to ensure proper mixing. If the reservoir and mixing compartments drain at the same rate, the solution flowing from the mixing compartment will linearly increase in concentration over time.

Many gradient makers use gravity to drive the drainage of each compartment.[176] Greater control over the flow rate can be achieved by using two peristaltic pumps to pump solution from the reservoir tube into the mixing compartment and from the mixing compartment to the instrument. However, a linear gradient maker based on this peristaltic pump design is complicated by the need for two flow rates, one from the reservoir into the mixing compartment and twice that rate from the mixing tube into the instrument, and by the constantly decreasing volume in the mixing compartment.

A nonlinear gradient maker allows for a simpler two-compartment system than a linear gradient maker. In this system, a single flow rate is used to pump from the reservoir into the mixing compartment and from the mixing compartment into the instrument. Thus, a single pump with two tubes may be used to drive the flow, and the mixing chamber remains at a constant volume. The nonlinear gradient output from this system depends on three variables, the

concentration in the reservoir, the flow rate, and the volume of the mixing compartment, and is governed by Equation 6.2.

To test whether the nonlinear gradient maker produced the expected gradient profile, a concentrated phosphate buffered saline (PBS) solution was used in the reservoir tube and deionized water in the mixing compartment. First, the PBS solution was directly injected over the microring resonators to determine the maximum response to the refractive index difference. The gradient maker was then tested at flow rates ranging from 5-20 μL/min and mixing volumes from 250 to 1000 μL. All showed close agreement between the gradient curves predicted by Equation 6.2 and the refractive index shift measured by the microring resonators. A representative plot is shown in Figure 6.2. A comparison of the concentration profiles generated by a step titration and the gradient titration can be found in Figure 6.3.

As seen in Figure 6.3 and explored in recent reports,[180,181] Taylor dispersion occurring in the fluidic system upstream of the sensor surface can cause significant deviation from ideal step concentration profiles. Diffusion in the tubes from the mixing compartment to the chip surface causes significant rise and fall times on the order of minutes for the step titration (Figure 6.3B). A much smaller rise time is observed for the nonlinear gradient (Figure 6.3A). Fick's first law states that diffusive flux is proportional to the concentration gradient. Because the concentration gradient is much smaller for the nonlinear gradient titration than the step titration, nonlinear gradient concentration profiles are less influenced by these fluidic diffusion effects than traditional step titrations.

6.3.2 Theoretical Validation of the Nonlinear Gradient Method

Numerical simulations were used to assess whether the nonlinear gradient method offered the same capabilities as the linear gradient method. Numerical simulations allowed evaluation of

a greater number and wider range of conditions than would have been experimentally feasible. It also allowed theoretical validation of the nonlinear gradient strategy against precisely known kinetic rates. Theoretical binding curves were generated by inputting the concentration gradient profiles, kinetic rate constants, the number of surface binding sites, flow cell dimensions, and diffusion constant into a two-dimension partial differential equation model accounting for diffusion and lateral flow. Binding at the surface was assumed to be first order. This model is governed by Equations 6.3−6.7.

Theoretical binding curves generated with the more complex two-dimensional partial differential equations model were fit to simpler models to extract kinetic rates. A range of association rates ranging from 5×10^{3} to 1×10^{8} $M^{-1}s^{-1}$ and dissociation rates from 1×10^{-5} to 1 s^{-1} were examined. Fitting the theoretical curves with a simple one-to-one interaction model for the association (Equation 6.8) and a single exponential dissociation model (Equation 6.11) generally yielded fits that were accurate to within 1-3% and a confidence interval within 5 to 10% of the actual value (see Table 6.1). One exception was observed when dissociation rates greater than 0.1 s^{-1} were investigated. For very fast dissociation rates, the dissociation of analyte from the surface happens on the same time scale as the diffusion of analyte. This leads to nonzero free analyte concentration levels throughout the dissociation phase that invalidate the simple exponential dissociation model. More complex models for the dissociation phase showed somewhat improved fits for these fast dissociation rates but were still nearly 15% from the known value. Thus, the nonlinear gradient method is valid for association rates ranging from 5×10^{3} to 1×10^{8} $M^{-1}s^{-1}$ and dissociation rates less than 0.1 s^{-1}, ranges similar to those reported for Biacore experiments.[162,182] However, even for kinetic rates outside this range, it is possible to obtain accurate equilibrium binding constants.

Although the one-to-one model generally fit well for kinetic rates within the bounds listed above, there was still some discrepancy between the actual and extracted rates that may be attributed to mass transport effects. There are several ways to account for mass transport of analyte to the biosensor surface. One commonly used approach is known as the two-compartment model.[174,175,182] The two-compartment model was used in previous theoretical studies of the linear analyte gradient method[173] and has also been applied to account for spatial offsets in surface plasmon resonance arrays.[183] Application of the two-compartment model to the simulated nonlinear gradient binding curves yielded kinetic rates accurate to within 1% (see Table 6.2). Similar to linear gradients, the nonlinear gradient method shows poor confidence in the k_m value indicating that the method does not produce reliable estimates of diffusion constants.[173,174] However, the two-compartment model is more accurate for association and dissection rates than the one-to-one model.

An alternative approach to the two-compartment model is to manually adjust the input into the model to account for the fact that the concentration profile seen by the surface is influenced by mass transport. For example, with FastStep injection, the instrument generates a calibration curve based on a sucrose injection before the analysis.[172] This calibration concentration profile is used to define the analyte concentration profile in data analysis. However, mass transport has different effects in a step titration system versus a gradient system. In a step titration, the concentration changes sharply. Mass transport causes the distortion of the concentration profile at the beginning of the step but quickly reaches equilibrium.[172,174] In a gradient experiment, the concentration is constantly changing, and the concentration profile will always be in flux. When the gradient is linear or near linear, this flux is fairly constant, and mass transport may be approximated as a delay of the gradient curve rather than a distortion of the

concentration profile. In the microring resonator system, this delay is exaggerated by the spatial offset of microrings along the length of the flow cell. Because the concentration profile is not constant, each microring experiences a slightly different environment at any point in time. Fortunately, the spatial offset and mass transport can both be approximated as a time delay of the ideal concentration profile. This delay can be corrected by simply shifting the binding curves on the time axis thereby temporally aligning the curves from each microring with the first curve (see Figure 6.4). After aligning and averaging the curves, the one-to-one model fits nearly as well as the two-compartment model (see Table 6.3).

Although the fits from both the two-compartment and temporal alignment model were similar in minimally mass transport-influenced systems, the two-compartment model gives more accurate fits in significantly mass transport-influenced systems. A key measure of the degree of mass transport influence is the ratio of $k_a\Gamma_{tot}/k_m$, which is referred to as the mass transport coefficient (MTC).[184] Larger MTC values correspond to a greater mass transport influence on the system. To evaluate the limits of the nonlinear gradient method with regards to mass transport, binding curves were simulated for a constant K_D but with increasing association rates.[182] These rates were simulated at a low binding site density and at high binding site density to achieve different MTC values for the same kinetic rates. Simulated rates, extracted rates, and MTC values are given in Table 6.4. At low MTC values, accurate kinetic rates are extracted using the two-compartment model. However, at MTC values above about 5, the kinetic rates are no longer reliable. Although kinetic rates are not reliable for high MTC, accurate equilibrium constants may still be obtained. This agrees with previously published results[182] for the two-compartment model applied to step titrations. Therefore, the nonlinear analyte gradient method has similar theoretical capabilities and limitations as step titrations with regards to mass transport.

Finally, to determine if nonlinearity of the gradient slope influenced the accuracy of the extracted kinetic rates, the nonlinear gradient method was tested at a variety of flow rates and mixing compartment volumes to adjust the curvature of the gradient concentration profile. Fitting to the two-compartment model yielded kinetic rates that were accurate to within 1-2% (see Table 6.5). Concentration profiles and binding curves for the parameters in Table 6.5 are illustrated in Figure 6.5. These results demonstrate that the nonlinear gradient method is applicable to varying gradient slopes and curvatures. There are, however, theoretical and experimental limitations on the gradient. The primary theoretical limitation to slope is lateral mass transport effects. For a very steep slope, the spatial differences in the concentration profile will be exaggerated, and greater mass transport distortions will be introduced. Shallow slopes reduce mass transport effects but require more time. Experimentally, fast flow rates will improve mass transport but will consume more material. Larger mixing volumes will also consume more material but can be measured more precisely than small mixing volumes. Regardless, the above results demonstrate that under a range of reasonable experimental conditions the nonlinear gradient method extracts accurate kinetic rates and equilibrium binding constants.

6.3.3 Application of the Nonlinear Gradient Method to Measure PSA-Antibody Binding on Microring Resonators

To apply the nonlinear gradient method experimentally, the prototype nonlinear gradient maker described above was interfaced with the microring resonator platform to measure the binding of PSA with an anti-PSA antibody. Of the thirty-two individually addressable microrings, eight microrings remained covered in a polymer cladding layer as thermal controls, twelve exposed microrings served as bulk index control surfaces, and twelve microrings were functionalized with single stranded DNA (see Figure 6.1 for schematic). The DNA-antibody

conjugate was attached to the surface by Watson-Crick base paring. The binding response was measured in real-time for a nonlinear gradient association followed by a buffer injection to monitor dissociation. Three different gradient curvatures were tested and fit individually to determine the effects of flow rate and gradient curvature. Extracted kinetic rates are given in Table 6.6. Normalized association and dissociation curves as well as fits are seen in Figure 6.6.

In all three experiments, k_a, k_d, and K_D values agree within the 95% confidence interval. The k_d values agree closely with the previously published rate for anti-PSA-5G6 and PSA measured on the same platform with a step titration series, while the k_a values are around 40% of the previously published rate.[150] Of the three binding curves, only curve A with the steep gradient (concentration equal to 100 nM) and low flow rate (11.3 μL/min) shows evidence of mass transport influences. For the curves B and C with a faster flow rate (18.4 μL/min) or with a shallower slope (50 nM), fitted k_m values have no upper bound indicating an essentially infinitely fast mass transport rate (see Table 6.6). Moreover, fitting these two curves to the one-to-one model yields fits very similar to the two-compartment model. Conversely, curve A showed an improved fit with the two-compartment model and bounded k_m values. Thus, experimental results reinforce theoretical conclusions that shallower slopes and faster flow rates limit mass transport effects in the nonlinear gradient method. These experimental results demonstrate the utility of the nonlinear gradient method for single shot kinetic experiments on the microring resonator platform.

6.4 Conclusions

This chapter detailed the instrumentation, simulation, and experimental application of the nonlinear analyte gradient method for kinetics of biomolecular interactions. This represents the first application of single shot kinetic experiments on the microring resonator biosensor platform.

Because the surface does not need to be regenerated, as with step-wise titrations, the analyte gradient method requires less time, materials, and sample preparation than conventional methods, and it offers increased analyte throughput. Although this experiment focused on a single ligand and analyte, future experiments making use of the multiplexing capabilities of the microring resonators will allow for single shot kinetic experiments for multiple ligands and increased assay throughput.

The principles of nonlinear analyte gradient instrumentation and experiment design are readily applicable to other refractive index-based biosensor platforms. The simplicity of the nonlinear gradient maker design makes it available to a variety of platforms and instruments. Some commercial fluidic systems have the capability to generate analyte gradients.[172] Because the nonlinear gradient maker design detailed here could be powered by a single syringe pump with a sealed mixing compartment, existing instruments could be retrofitted with a gradient maker.

Finally, it is important to note that the nonlinear analyte gradient method is limited by many of the same constraints as conventional step titration experiments. Similar to step titration experiments, kinetic rates should be in the bounds detailed above. The curvature and slope of the analyte gradient profile must be tuned to avoid mass transport problems. Finally, data must be of high quality with appropriate controls to correct for baseline shifts. Despite these limitations, the nonlinear analyte gradient method is an effective alternative to conventional step-titration techniques that allows for higher throughput and single shot kinetic experiments with minimal additional instrumentation.

6.5 Tables and Figures

Table 6.1: Kinetic Rates Determined by Fitting Simulated Nonlinear Analyte Gradient Data to the One-to-One Interaction Model

Simulated Parameters		Extracted Rates One-to-One Model			
k_a ($M^{-1}s^{-1}$)	k_d (s^{-1})	k_a ($M^{-1}s^{-1}$)		k_d (s^{-1})	
5.00×10^{5}	1.00×10^{0}	1.35×10^{5}	(0.81-2.56)	2.75×10^{-1}	(1.66-5.22)
5.00×10^{5}	1.00×10^{-1}	4.47×10^{5}	(4.07-6.01)	9.17×10^{-2}	(8.18-12.1)
5.00×10^{5}	1.00×10^{-2}	4.86×10^{5}	(4.68-5.19)	9.94×10^{-3}	(9.54-10.4)
5.00×10^{5}	1.00×10^{-3}	4.92×10^{5}	(4.86-5.04)	9.99×10^{-4}	(9.81-10.2)
5.00×10^{5}	1.00×10^{-4}	4.96×10^{5}	(4.94-5.00)	1.00×10^{-4}	(0.989-1.01)
5.00×10^{6}	1.00×10^{-2}	4.86×10^{6}	(4.68-5.19)	9.94×10^{-3}	(9.54-10.4)
5.00×10^{4}	1.00×10^{-2}	4.95×10^{4}	(4.86-5.09)	9.96×10^{-3}	(9.76-10.2)
5.00×10^{3}	1.00×10^{-2}	4.95×10^{3}	(4.87-5.08)	9.96×10^{-3}	(9.76-10.2)
5.00×10^{4}	5.00×10^{-4}	4.94×10^{4}	(4.90-5.05)	5.00×10^{-4}	(4.95-5.05)

Table 6.2: Kinetic Rates Determined by Fitting Simulated Nonlinear Analyte Gradient Data from Table 6.1 to the Two-Compartment Model

Extracted Rates Two-Compartment Model

k_a ($M^{-1}s^{-1}$)		k_d (s^{-1})		k_m (cm/s)	
2.29×10^{5}	(2.03-2.47)	4.58×10^{-1}	(4.06-4.93)	1.99×10^{-1}	(1.67-2.81)
4.99×10^{5}	(4.88-5.05)	9.96×10^{-2}	(9.76-10.1)	1.60×10^{-1}	(1.36-2.32)
5.00×10^{5}	(4.99-5.01)	9.99×10^{-3}	(9.98-10.0)	1.68×10^{-1}	(1.60-1.85)
5.00×10^{5}	(4.98-5.00)	1.00×10^{-3}	(0.997-1.00)	2.00×10^{-1}	(1.40-2.53)
5.02×10^{5}	(5.00-5.02)	1.00×10^{-4}	(0.995-1.00)	1.27×10^{-1}	(0.824-1.84)
5.01×10^{6}	(4.99-5.02)	1.00×10^{-2}	(0.998-1.00)	1.64×10^{-1}	(1.51-1.88)
5.00×10^{4}	(4.99-5.01)	1.00×10^{-2}	(0.998-1.00)	1.74×10^{-1}	(1.53-2.05)
5.00×10^{3}	(4.99-5.01)	1.00×10^{-2}	(0.998-1.00)	1.74×10^{-1}	(1.48-2.07)
5.00×10^{4}	(4.99-5.01)	5.00×10^{-4}	(4.99-5.00)	1.68×10^{-1}	(1.57-1.76)

Table 6.3: Kinetic Rates Determined by Fitting Simulated Nonlinear Analyte Gradient Data from Table 6.1 to the Temporally Shifted One-to-One Model

Extracted Rates Temporally Shifted One-to-One Model

k_a ($M^{-1}s^{-1}$)		k_d (s^{-1})	
2.22×10^{5}	(1.82-3.57)	4.45×10^{-1}	(3.65-7.17)
4.90×10^{5}	(4.78-5.17)	9.85×10^{-2}	(9.57-10.4)
4.97×10^{5}	(4.93-5.02)	9.98×10^{-3}	(9.90-10.1)
4.99×10^{5}	(4.97-5.00)	1.00×10^{-3}	(0.997-1.00)
4.99×10^{5}	(4.99-5.00)	1.00×10^{-4}	(0.998-1.00)
4.97×10^{6}	(4.93-5.03)	9.99×10^{-3}	(9.90-10.0)
4.99×10^{4}	(4.97-5.02)	9.99×10^{-3}	(9.95-10.0)
4.99×10^{3}	(4.97-5.02)	9.99×10^{-3}	(9.95-10.0)
4.99×10^{4}	(4.98-5.00)	5.00×10^{-4}	(4.99-5.01)

Table 6.4: Kinetic Rates Determined by Fitting Simulated Nonlinear Analyte Gradient Data to Two-Compartment Model

Simulated Parameters[a]			Extracted Rates Two-Compartment Model						
k_a ($M^{-1}s^{-1}$)	k_d (s^{-1})	Γ_{tot} (mol/cm^2)	k_a ($M^{-1}s^{-1}$)		k_d (s^{-1})		k_m (cm/s)		*MTC*
1.00×10^{6}	1.00×10^{-3}	6.00×10^{-13}	1.01×10^{6}	(0.997-1.01)	1.00×10^{-3}	(0.995-1.01)	1.31×10^{-1}	(0.932-2.49)	0.005
1.00×10^{7}	1.00×10^{-2}	6.00×10^{-13}	1.00×10^{7}	(0.999-1.00)	1.00×10^{-2}	(0.998-1.00)	1.66×10^{-1}	(1.58-1.82)	0.036
1.00×10^{8}	1.00×10^{-1}	6.00×10^{-13}	9.97×10^{7}	(9.73-10.1)	9.95×10^{-2}	(9.72-10.1)	1.60×10^{-1}	(1.31-2.33)	0.373
1.00×10^{6}	1.00×10^{-3}	1.20×10^{-10}	1.00×10^{6}	(0.998-1.01)	1.00×10^{-3}	(0.997-1.00)	1.51×10^{-1}	(1.21-1.97)	0.795
1.00×10^{7}	1.00×10^{-2}	1.20×10^{-10}	1.00×10^{7}	(0.996-1.00)	9.98×10^{-3}	(9.95-10.0)	1.70×10^{-1}	(1.55-2.01)	7.050
1.00×10^{8}	1.00×10^{-1}	1.20×10^{-10}	9.78×10^{7}	(9.57-9.90)	9.76×10^{-2}	(9.57-9.90)	1.74×10^{-1}	(1.51-2.47)	67.57

[a] Additional parameters used included V = 1000 μL, r = 10 μL/min, M = 25 nM. Other parameters are as stated in the text.

Table 6.5: Kinetic Rates Determined by Fitting Various Nonlinear Concentration Profiles to the Two-Compartment Model

	Simulated Parameters						Extracted Rates Two-Compartment Model			
	k_a ($M^{-1}s^{-1}$)	k_d (s^{-1})	V (μL)	r (μL/min)	*V/r (min)*	*M (nM)*	k_a ($M^{-1}s^{-1}$)		k_d (s^{-1})	
A	5.00×10^{5}	0.01	1000	10	100	396	5.00×10^{5}	(4.99-5.00)	1.00×10^{-2}	(0.999-1.00)
B	5.00×10^{5}	0.01	250	10	25	168	5.00×10^{5}	(4.99-5.01)	1.00×10^{-2}	(0.998-1.00)
C	5.00×10^{6}	0.1	500	20	25	168	5.01×10^{6}	(4.97-5.05)	1.00×10^{-1}	(0.993-1.01)
D	5.00×10^{6}	0.1	500	50	10	138	5.01×10^{6}	(4.97-5.04)	1.00×10^{-1}	(0.995-1.01)
E	5.00×10^{6}	0.1	100	100	1	138	5.03×10^{6}	(4.93-5.15)	1.00×10^{-1}	(0.986-1.03)
F	5.00×10^{6}	0.1	100	40	2.5	168	5.04×10^{6}	(4.90-5.22)	1.00×10^{-1}	(0.977-0.103)

Table 6.6: PSA Binding to Anti-PSA Antibody with Nonlinear Gradient Method Fit to Two-Compartment Model

	Concentration Profile			Extracted Rates Two-Compartment Model					
	r (μL/min)	V (μL)	M (nM)	k_a ($M^{-1}s^{-1}$)		k_d (s^{-1})		k_m (Δpm/Ms)	
A	11.3	1000	100	9.76×10^{5}	(6.38-14.6)	1.09×10^{-3}	(0.947-1.27)	1.32×10^{7}	(0.631-3.69)
B	18.4	1000	100	7.37×10^{5}	(5.60-9.58)	1.02×10^{-3}	(0.898-1.20)	5.21×10^{9}	(2.61-∞)
C	11.3	1000	50	1.00×10^{6}	(0.749-1.40)	1.20×10^{-3}	(1.03-1.50)	4.03×10^{7}	(2.22-∞)

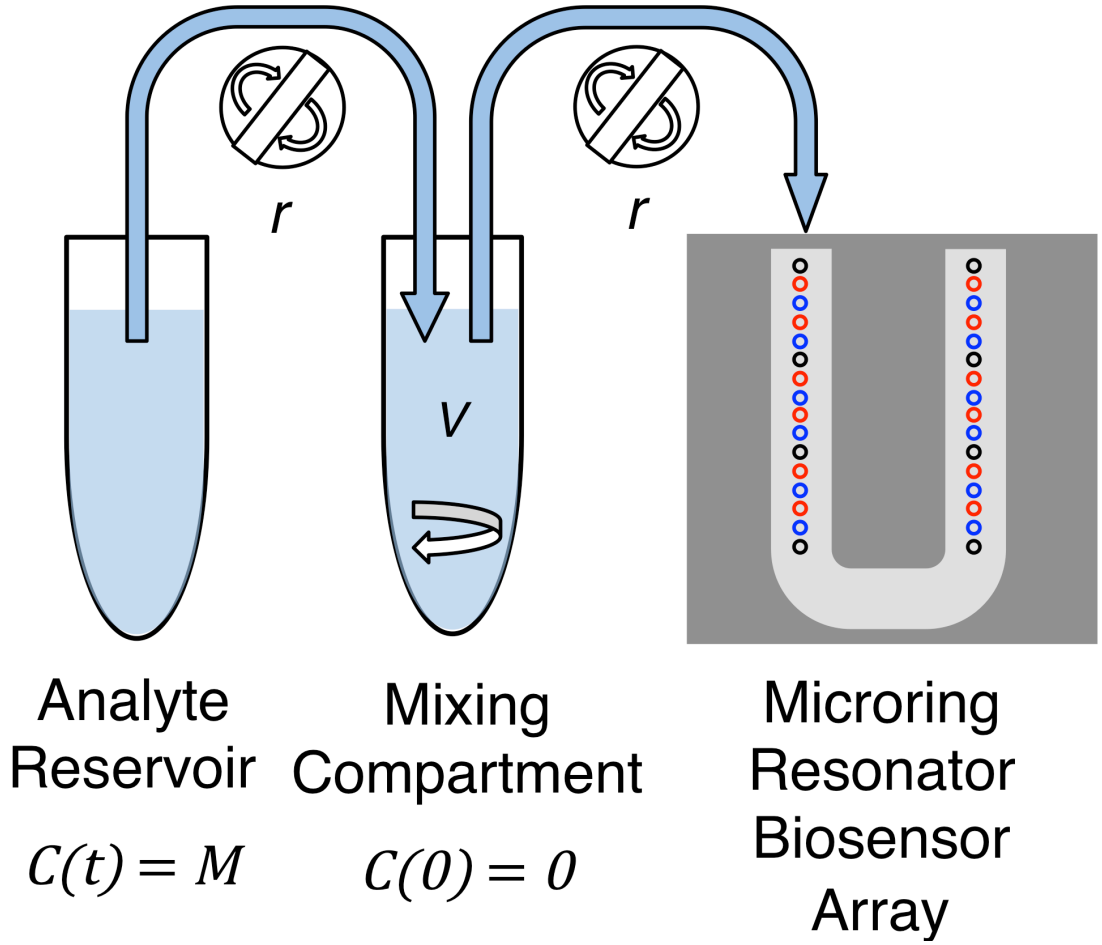


Figure 6.1: Schematic of nonlinear gradient maker and microring resonator array. Analyte solution with concentration M is placed in the analyte reservoir. Buffer with volume V is placed in the mixing compartment. Analyte is pumped from the analyte reservoir into the mixing tube by a peristaltic pump at flow rate r, and the gradient solution is also pumped at rate r across the microring resonator array. The microring resonator array is made up of thirty-two rings addressed via a U-channel flow cell. *Black* rings represent thermal controls, *blue* rings represent control rings (non-DNA functionalized), and *red* rings represent active rings (DNA functionalized).

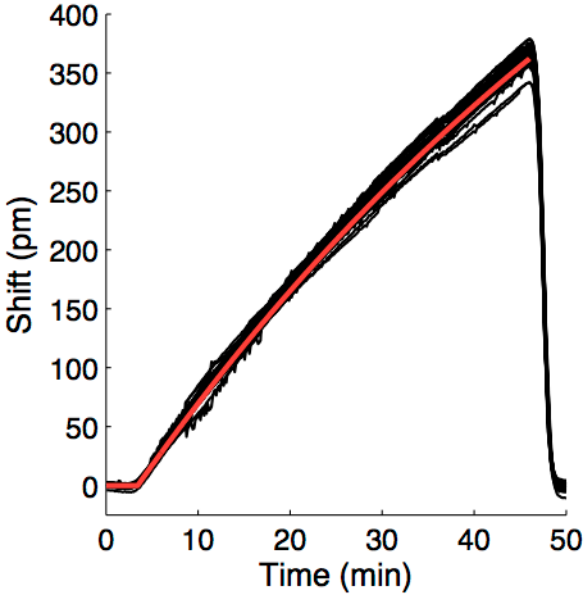


Figure 6.2: Validation of the nonlinear gradient maker. A 10X PBS buffer is used in the analyte reservoir with a 1 mL mixing volume and 13 μL/min flow rate. The maximum shift is calculated from the average maximum response from the undiluted 10X PBS buffer (Figure 6.3B). The microring resonator response from all twenty-four rings is shown in *black*, and the predicted gradient output calculated from Equation 6.2 is shown in *red*.

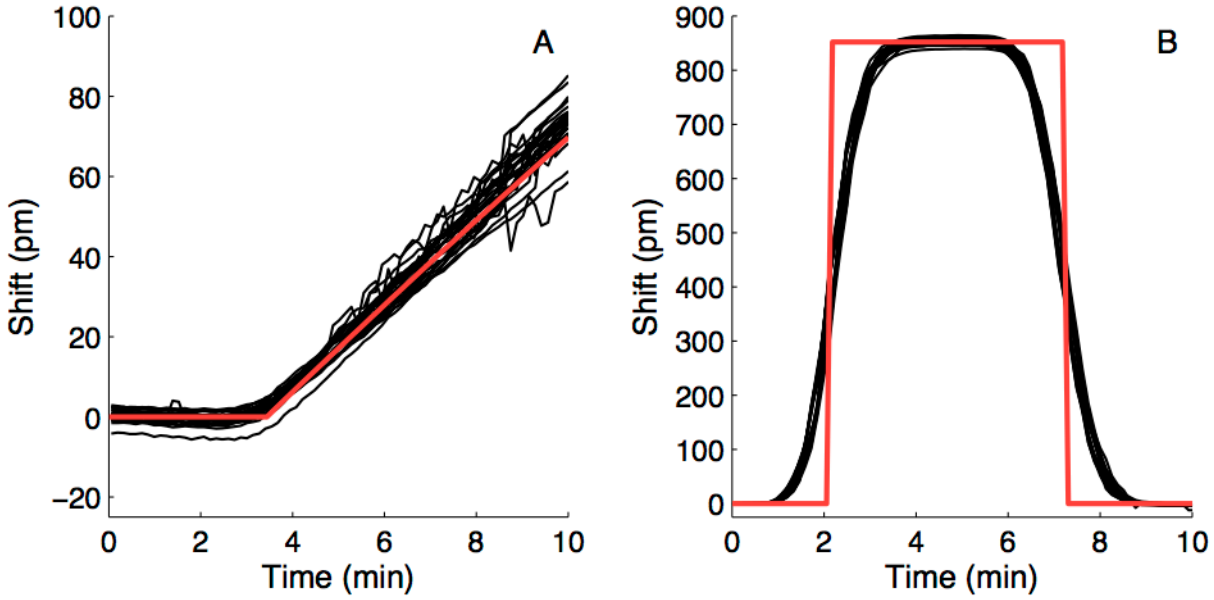


Figure 6.3: Comparison of (*A*) nonlinear gradient concentration profile and (*B*) step titration profile. *A* is taken as an expanded view of Figure 6.2. *B* is the microring resonator response to a step titration of 10X PBS at full concentration with the same flow rate as *A*. Microring resonator response is shown in *black* and predicted response is shown in *red*.

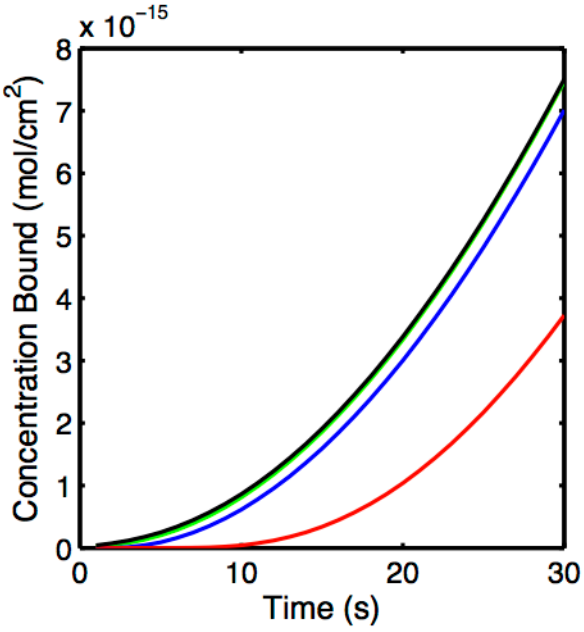


Figure 6.4: Simulated binding curves for the first parameters in Table 6.5. The binding curve for the first simulated microring is shown in *blue* and for the last simulated microring in *red*. Temporal alignment transforms the last microring (*red*) to a corrected binding curve in *black*. The average of all temporally shifted microrings is shown in *green* and overlaps nearly completely with the *black* curve.

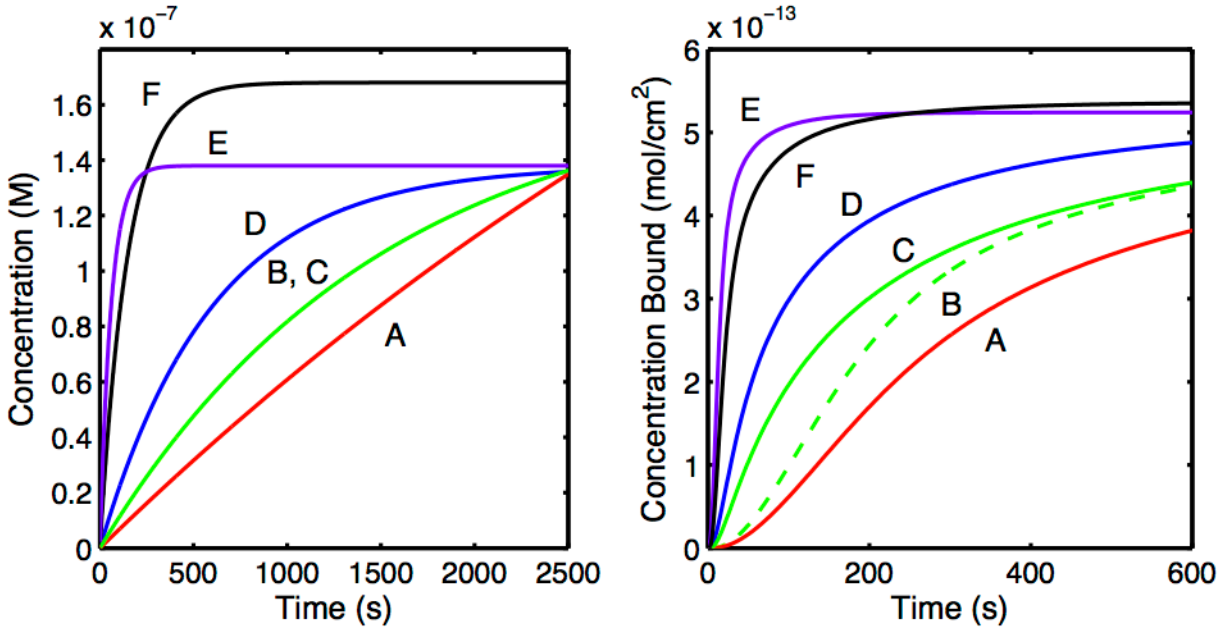


Figure 6.5: Concentration (*left*) and simulated binding curves (*right*) for the data in Table 6.5. Rows in Table 6.5 are shown as *red* (A), *dashed green* (B), *solid green* (C), *blue* (D), *purple* (E), and *black* (F). *Solid* (C) and *dashed green* (B) lines both derive from the *green* (B, C) concentration profile. Note that the time scale in the right plot has been shortened for clarity.

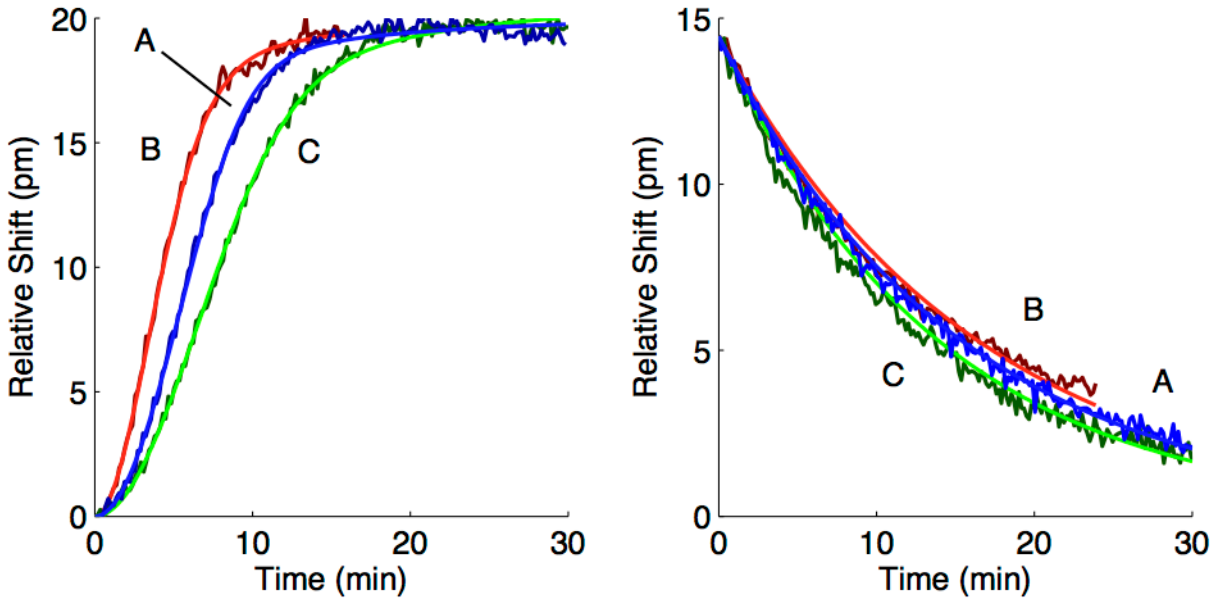


Figure 6.6: Microring resonator response for PSA binding to anti-PSA antibody and fits to the two-compartment model for concentration profiles detailed in Table 6.6. Normalized experimental association (*left*) and dissociation (*right*) curves from Table 6.6 are presented as *dark blue* (A), *dark red* (B), and *dark green* (C). Fits are presented as *blue*, *red*, and *green* respectively.

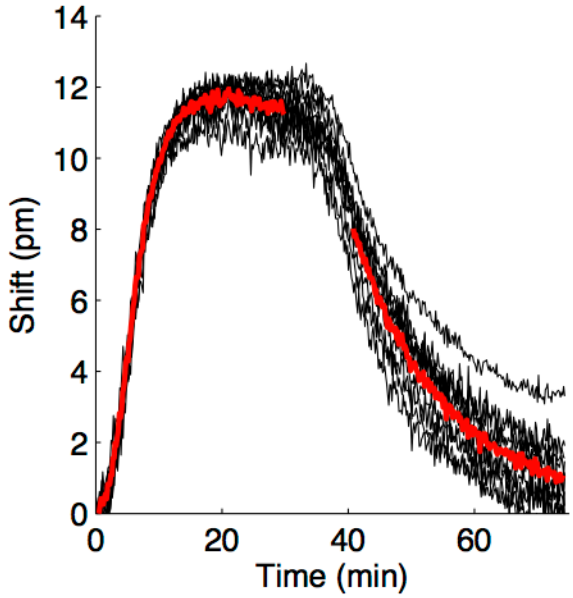


Figure 6.7: Data set from active rings (*black*) from A in Table 6.6 with the averaged and cropped curves shown in *red*.

CHAPTER 7: CONCLUSIONS AND FUTURE DIRECTIONS

Membrane systems play a central role in biochemistry, pharmacology, and bioenergy. It is therefore crucial to understand the complex biochemical interactions that occur at membrane surfaces. Previous technologies for solubilizing membrane proteins have either neglected the membrane component, as in the case of detergents or amphipols, or provided polydisperse and ill-defined lipid bilayer system, as with bicelles and liposomes. Nanodiscs provide a platform for solubilizing and studying membrane proteins that offers a well-defined, monodisperse, and native-like lipid bilayer.

Native mass spectrometry of intact Nanodisc complexes was employed in Chapter 2 to characterize the polydispersity of Nanodiscs at the molecular level.[83] Single lipid resolution combined with a probability-based strategy to deconvolute overlapping mass and charge distributions provided a direct picture of the monodispersity of Nanodiscs in the gas phase. The gas-phase monodispersity of Nanodiscs highlights the solution-phase advantage that Nanodiscs provide a uniform and homogeneous bilayer environment. These studies also demonstrated the robustness of Nanodiscs through the desolvation and ionization process.

Their monodispersity and robustness suggest that Nanodiscs are a promising platform for studies of membrane proteins and mixed lipid systems by native mass spectrometry. For membrane proteins in Nanodiscs, this monodispersity offers the unique potential to resolve the full membrane protein-Nanodisc complex. Comparing the total number of lipids present in the complex with an empty control would allow measurement of the lipid bilayer footprint for a given membrane protein. Fragmentation of the membrane protein-Nanodisc complex may reveal intermediates with bound lipids that provide information on interactions with loosely bound annular lipids as well as tightly bound structural lipids.[5,6,38] Fragmentation of mixed lipid

Nanodiscs offers the exciting potential to observe lipid-lipid interactions. In homogenous systems, homo-oligomers including dimers and trimers are observed in the low mass region of the spectra. It is possible that mixed lipid systems would present meaningful hetero-oligomers that reveal nanoclusters of lipids. In both membrane protein and mixed lipid systems, the central challenges are sample heterogeneity and physiological relevance. Experimental methods, theory, and data analysis methods outlined in this dissertation for homogeneous Nanodisc systems will lay the groundwork for future Nanodisc mass spectrometry studies of more complex systems.

Heterogeneous libraries of membrane proteins in Nanodiscs hold great potential to shed light on the molecular mechanisms of disease. Chapter 3 developed the formation of Nanodisc-solubilized membrane protein libraries from *E. Coli* outer and inner membranes and demonstrated that the SMPL proteome mimics the native membrane proteome.[84]

The SMPL approach is being applied to study the interaction of amyloid β oligomers (AβO) with synaptic receptors.[185,186] The binding of AβO to the synapse surface is believed to be a key step in the pathogenesis of Alzheimer's disease.[187-189] However, the identity of its interaction partner or partners is not known.[190] Synaptic SMPL Nanodiscs reflect the protein content of synaptic membranes and show receptor and enzymatic activity for two important classes of synaptic proteins. SMPL Nanodiscs reproduce key elements of AβO binding including saturability and selectivity to a small population of protein, adding unique support to the protein receptor hypothesis of AβO binding. SMPL Nanodiscs also enable development of a high-throughput assay using an unbiased membrane receptor pool to identify potential Alzheimer's disease therapeutics. This application demonstrates the unique potential of heterogeneous SMPL Nanodiscs for biochemical assays, drug discovery, and target identification.

The same approach used with the amyloid β oligomers can be extended to identify binding partners for pathogens, biomolecules, or drugs. In theory, any system that binds membrane proteins and can be captured could utilize the SMPL technology. One particularly interesting concept is the study of interactions between two separate soluble membrane protein libraries. SMPL-SMPL studies could be used to look at cell-cell communications and to isolate specific points of contact.

Chapter 4 described the use of the ultra-thin layer sample preparation technique to selectively analyze membrane proteins inside Nanodiscs with MALDI mass spectrometry while limiting the signal from MSP.[85] Full-length protein mass spectrometry provides a means of characterizing covalent modifications of proteins and could be used for novel bioassays.

Photonic microring resonator biosensors provide a platform for multiplexed assays of protein-protein and protein-lipid interactions. Chapter 5 described the interfacing of Nanodiscs with the microring resonator chips via direct physisorption on the silica biosensor surface.[86] After correcting for differences in loading due to electrostatics of the lipid head groups, microring resonator biosensors can be used to measure the interactions between fixed Nanodisc samples with varying concentrations of soluble binding partner and between a fixed concentration of the soluble binding partner with Nanodiscs of varying lipid compositions. A prototype four-plexed assay demonstrated the potential for multiplexed sensing arrays of Nanodiscs with different membrane protein or lipid species. Chapter 6 described the theoretical and instrumental basis for using nonlinear analyte gradients to perform single run kinetic experiments.[87] The nonlinear analyte gradient approach was applied to measure the binding of PSA to an anti-PSA antibody.

There are several promising future directions for the application of Nanodiscs and microring resonators. One application is in the development of multiplexed "lipid chips" to probe the binding of peripheral membrane proteins to lipid bilayers of varying composition. Peripheral membrane binding is important in a variety of biological processes including blood coagulation[71] and integrin signaling.[37] A multiplexed chip that allowed probing of not only binary[75] but also ternary combinations of lipid species in a single experiment would significantly increase the throughput of these studies. A related application is the development of membrane protein arrays to probe for potential binding to a number of targets simultaneously. This type of membrane protein chip would likely rely on improved attachment strategies such as a DNA-encoded antibody library[150] targeted to peptide sequences on MSP (FLAG or polyhistidine for example) or DNA-tagged Nanodiscs themselves.

Nanodiscs were first developed just over a decade ago[27] and have over this time emerged as a robust and mature technology for studying membrane systems. Although they are not universally applicable, Nanodiscs provide multiple advantages over competing membrane mimetics in providing a well-defined lipid bilayer system to study membrane proteins and lipids. There is ample reason to be optimistic about the applications of Nanodiscs to biochemical research over the next decade. The potential of Nanodiscs as therapeutic delivery agents is just beginning to be realized.[191] The development of heterogeneous Nanodisc-solubilized membrane protein libraries opens new avenues for fundamental biochemistry, target identification, and drug discovery. Finally, growing acceptance within the mass spectrometry and biosensor communities promises exciting future applications of Nanodiscs to bioanalytical chemistry.

REFERENCES

(1) von Heijne, G. The membrane protein universe: what's out there and why bother? *J. Intern. Med.* **2007**, *261*, 543-557.

(2) Bakheet, T. M.; Doig, A. J. Properties and identification of human protein drug targets. *Bioinformatics* **2009**, *25*, 451-457.

(3) Bernaudat, F.; Frelet-Barrand, A.; Pochon, N.; Dementin, S.; Hivin, P.; Boutigny, S.; Rioux, J. B.; Salvi, D.; Seigneurin-Berny, D.; Richaud, P.; Joyard, J.; Pignol, D.; Sabaty, M.; Desnos, T.; Pebay-Peyroula, E.; Darrouzet, E.; Vernet, T.; Rolland, N. Heterologous expression of membrane proteins: choosing the appropriate host. *PLoS ONE* **2011**, *6*, e29191.

(4) Zoonens, M.; Miroux, B. Expression of Membrane Proteins at the Escherichia coli Membrane for Structural Studies. In *Heterologous Expression of Membrane Proteins*; Humana Press, 2010; Vol. 601; pp 49-66.

(5) Lee, A. G. Lipid-protein interactions. *Biochem. Soc. Trans.* **2011**, *39*, 761-766.

(6) Barrera, N. P.; Zhou, M.; Robinson, C. V. The role of lipids in defining membrane protein interactions: insights from mass spectrometry. *Trends Cell Biol.* **2013**, *23*, 1-8.

(7) Das, A.; Sligar, S. G. Modulation of the cytochrome P450 reductase redox potential by the phospholipid bilayer. *Biochemistry* **2009**, *48*, 12104-12112.

(8) Jones, M. N. Surfactants in membrane solubilisation. *Int. J. Pharm.* **1999**, *177*, 137-159.

(9) Arnold, T.; Linke, D. The Use of Detergents to Purify Membrane Proteins. In *Current Protocols in Protein Science*; John Wiley & Sons, Inc., 2001.

(10) Garavito, R. M.; Ferguson-Miller, S. Detergents as tools in membrane biochemistry. *J. Biol. Chem.* **2001**, *276*, 32403-32406.

(11) Seddon, A. M.; Curnow, P.; Booth, P. J. Membrane proteins, lipids and detergents: not just a soap opera. *Biochim. Biophys. Acta* **2004**, *1666*, 105-117.

(12) Duquesne, K.; Sturgis, J. N. Membrane Protein Solubilization. In *Heterologous Expression of Membrane Proteins*; Humana Press, 2010; Vol. 601; pp 205-217.

(13) Popot, J. L. Amphipols, nanodiscs, and fluorinated surfactants: three nonconventional approaches to studying membrane proteins in aqueous solutions. *Annu. Rev. Biochem.* **2010**, *79*, 737-775.

(14) Popot, J. L.; Althoff, T.; Bagnard, D.; Baneres, J. L.; Bazzacco, P.; Billon-Denis, E.; Catoire, L. J.; Champeil, P.; Charvolin, D.; Cocco, M. J.; Cremel, G.; Dahmane, T.; de la Maza, L. M.; Ebel, C.; Gabel, F.; Giusti, F.; Gohon, Y.; Goormaghtigh, E.; Guittet, E.; Kleinschmidt, J. H.; Kuhlbrandt, W.; Le Bon, C.; Martinez, K. L.; Picard, M.; Pucci, B.; Sachs, J. N.; Tribet, C.; van Heijenoort, C.; Wien, F.; Zito, F.; Zoonens, M. Amphipols from A to Z. *Annu. Rev. Biophys.* **2011**, *40*, 379-408.

(15) Rigaud, J. L.; Paternostre, M. T.; Bluzat, A. Mechanisms of membrane protein insertion into liposomes during reconstitution procedures involving the use of detergents. 2. Incorporation of the light-driven proton pump bacteriorhodopsin. *Biochemistry* **1988**, *27*, 2677-2688.

(16) Sanders, C. R.; Prosser, R. S. Bicelles: a model membrane system for all seasons? *Structure* **1998**, *6*, 1227-1234.

(17) Czerski, L.; Sanders, C. R. Functionality of a membrane protein in bicelles. *Anal. Biochem.* **2000**, *284*, 327-333.

(18) Durr, U. H.; Gildenberg, M.; Ramamoorthy, A. The magic of bicelles lights up membrane protein structure. *Chem. Rev.* **2012**, *112*, 6054-6074.
(19) Faham, S.; Bowie, J. U. Bicelle crystallization: a new method for crystallizing membrane proteins yields a monomeric bacteriorhodopsin structure. *J. Mol. Biol.* **2002**, *316*, 1-6.
(20) Ujwal, R.; Bowie, J. U. Crystallizing membrane proteins using lipidic bicelles. *Methods* **2011**, *55*, 337-341.
(21) Atkinson, D.; Small, D. M. Recombinant lipoproteins: implications for structure and assembly of native lipoproteins. *Annu. Rev. Biophys. Biophys. Chem.* **1986**, *15*, 403-456.
(22) Jonas, A. Reconstitution of high-density lipoproteins. *Methods Enzymol.* **1986**, *128*, 553-582.
(23) Bayburt, T. H.; Carlson, J. W.; Sligar, S. G. Reconstitution and imaging of a membrane protein in a nanometer-size phospholipid bilayer. *J. Struct. Biol.* **1998**, *123*, 37-44.
(24) Chromy, B. A.; Arroyo, E.; Blanchette, C. D.; Bench, G.; Benner, H.; Cappuccio, J. A.; Coleman, M. A.; Henderson, P. T.; Hinz, A. K.; Kuhn, E. A.; Pesavento, J. B.; Segelke, B. W.; Sulchek, T. A.; Tarasow, T.; Walsworth, V. L.; Hoeprich, P. D. Different apolipoproteins impact nanolipoprotein particle formation. *J. Am. Chem. Soc.* **2007**, *129*, 14348-14354.
(25) Bricarello, D. A.; Smilowitz, J. T.; Zivkovic, A. M.; German, J. B.; Parikh, A. N. Reconstituted lipoprotein: a versatile class of biologically-inspired nanostructures. *ACS Nano* **2011**, *5*, 42-57.
(26) Ryan, R. O. Nanobiotechnology applications of reconstituted high density lipoprotein. *J. Nanobiotechnology* **2010**, *8*, 28.
(27) Bayburt, T. H.; Grinkova, Y. V.; Sligar, S. G. Self-assembly of discoidal phospholipid bilayer nanoparticles with membrane scaffold proteins. *Nano Lett.* **2002**, *2*, 853-856.
(28) Denisov, I. G.; Grinkova, Y. V.; Lazarides, A. A.; Sligar, S. G. Directed self-assembly of monodisperse phospholipid bilayer nanodiscs with controlled size. *J. Am. Chem. Soc.* **2004**, *126*, 3477-3487.
(29) Grinkova, Y. V.; Denisov, I. G.; Sligar, S. G. Engineering extended membrane scaffold proteins for self-assembly of soluble nanoscale lipid bilayers. *Protein Eng. Des. Sel.* **2010**, *23*, 843-848.
(30) Baas, B. J.; Denisov, I. G.; Sligar, S. G. Homotropic cooperativity of monomeric cytochrome P450 3A4 in a nanoscale native bilayer environment. *Arch. Biochem. Biophys.* **2004**, *430*, 218-228.
(31) Bayburt, T. H.; Grinkova, Y. V.; Sligar, S. G. Assembly of single bacteriorhodopsin trimers in bilayer nanodiscs. *Arch. Biochem. Biophys.* **2006**, *450*, 215-222.
(32) Civjan, N. R.; Bayburt, T. H.; Schuler, M. A.; Sligar, S. G. Direct solubilization of heterologously expressed membrane proteins by incorporation into nanoscale lipid bilayers. *Biotechniques* **2003**, *35*, 556-563.
(33) Mi, L.-Z.; Grey, M. J.; Nishida, N.; Walz, T.; Lu, C.; Springer, T. A. Functional and structural stability of the epidermal growth factor receptor in detergent micelles and phospholipid nanodiscs. *Biochemistry* **2008**, *47*, 10314-10323.
(34) Inagaki, S.; Ghirlando, R.; White, J. F.; Gvozdenovic-Jeremic, J.; Northup, J. K.; Grisshammer, R. Modulation of the interaction between neurotensin receptor NTS1 and Gq protein by lipid. *J. Mol. Biol.* **2012**, *417*, 95-111.
(35) Bayburt, T. H.; Vishnivetskiy, S. A.; McLean, M. A.; Morizumi, T.; Huang, C.-C.; Tesmer, J. J. G.; Ernst, O. P.; Sligar, S. G.; Gurevich, V. V. Monomeric rhodopsin is sufficient for

normal rhodopsin kinase (GRK1) phosphorylation and arrestin-1 binding. *J. Biol. Chem.* **2011**, *286*, 1420-1428.
(36) Borch, J.; Torta, F.; Sligar, S. G.; Roepstorff, P. Nanodiscs for immobilization of lipid bilayers and membrane receptors: kinetic analysis of cholera toxin binding to a glycolipid receptor. *Anal. Chem.* **2008**, *80*, 6245-6252.
(37) Ye, F.; Hu, G.; Taylor, D.; Ratnikov, B.; Bobkov, A. A.; McLean, M. A.; Sligar, S. G.; Taylor, K. A.; Ginsberg, M. H. Recreation of the terminal events in physiological integrin activation. *J. Cell Biol.* **2010**, *188*, 157-173.
(38) Akkaladevi, N.; Hinton-Chollet, L.; Katayama, H.; Mitchell, J.; Szerszen, L.; Mukherjee, S.; Gogol, E. P.; Pentelute, B. L.; Collier, R. J.; Fisher, M. T. Assembly of anthrax toxin pore: Lethal-factor complexes into lipid nanodiscs. *Protein Sci.* **2013**, *22*, 492-501.
(39) Frauenfeld, J.; Gumbart, J.; van der Sluis, E. O.; Funes, S.; Gartmann, M.; Beatrix, B.; Mielke, T.; Berninghausen, O.; Becker, T.; Schulten, K.; Beckmann, R. Cryo-EM structure of the ribosome-SecYE complex in the membrane environment. *Nat. Struct. Mol. Biol.* **2011**, *18*, 614-621.
(40) Katayama, H.; Wang, J.; Tama, F.; Chollet, L.; Gogol, E. P.; Collier, R. J.; Fisher, M. T. Three-dimensional structure of the anthrax toxin pore inserted into lipid nanodiscs and lipid vesicles. *Proc. Natl. Acad. Sci.* **2010**, *107*, 3453-3457.
(41) Skar-Gislinge, N.; Arleth, L. Small-angle scattering from phospholipid nanodiscs: derivation and refinement of a molecular constrained analytical model form factor. *Phys. Chem. Chem. Phys.* **2011**, *13*, 3161-3170.
(42) Justesen, B. H.; Laursen, T.; Weber, G.; Fuglsang, A. T.; Moeller, B. L.; Gunther Pomorski, T. Isolation of monodisperse nanodisc-reconstituted membrane proteins using free flow electrophoresis. *Anal. Chem.* **2013**, *85*, 3497-3500.
(43) Alami, M.; Dalal, K.; Lelj-Garolla, B.; Sligar, S. G.; Duong, F. Nanodiscs unravel the interaction between the SecYEG channel and its cytosolic partner SecA. *EMBO J.* **2007**, *26*, 1995-2004.
(44) Inagaki, S.; Ghirlando, R.; Grisshammer, R. Biophysical characterization of membrane proteins in nanodiscs. *Methods* **2013**, *59*, 287-300.
(45) Monterroso, B.; Alfonso, C.; Zorrilla, S.; Rivas, G. Combined analytical ultracentrifugation, light scattering and fluorescence spectroscopy studies on the functional associations of the bacterial division FtsZ protein. *Methods* **2013**, *59*, 349-362.
(46) Denisov, I. G.; McLean, M. A.; Shaw, A. W.; Grinkova, Y. V.; Sligar, S. G. Thermotropic phase transition in soluble nanoscale lipid bilayers. *J. Phys. Chem. B* **2005**, *109*, 15580-15588.
(47) Shaw, A. W.; McLean, M. A.; Sligar, S. G. Phospholipid phase transitions in homogeneous nanometer scale bilayer discs. *FEBS Lett.* **2003**, *556*, 260-264.
(48) Bayburt, T. H.; Leitz, A. J.; Xie, G.; Oprian, D. D.; Sligar, S. G. Transducin activation by nanoscale lipid bilayers containing one and two rhodopsins. *J. Biol. Chem.* **2007**, *282*, 14875-14881.
(49) Denisov, I. G.; Grinkova, Y. V.; Baas, B. J.; Sligar, S. G. The ferrous-dioxygen intermediate in human cytochrome P450 3A4. Substrate dependence of formation and decay kinetics. *J. Biol. Chem.* **2006**, *281*, 23313-23318.
(50) Chougnet, A.; Grinkova, Y.; Ricard, D.; Sligar, S.; Woggon, W.-D. Fluorescent probes for rapid screening of potential drug-drug interactions at the CYP3A4 level. *ChemMedChem* **2007**, *2*, 717-724.

(51) Nath, A.; Trexler, A. J.; Koo, P.; Miranker, A. D.; Atkins, W. M.; Rhoades, E. Single-molecule fluorescence spectroscopy using phospholipid bilayer nanodiscs. *Methods Enzymol.* **2010**, *472*, 89-117.
(52) Mak, P. J.; Denisov, I. G.; Grinkova, Y. V.; Sligar, S. G.; Kincaid, J. R. Defining CYP3A4 structural responses to substrate binding. raman spectroscopic studies of a nanodisc-incorporated mammalian cytochrome P450. *J. Am. Chem. Soc.* **2011**, *133*, 1357-1366.
(53) Gregory, M.; Mak, P. J.; Sligar, S. G.; Kincaid, J. R. Differential hydrogen bonding in human CYP17 dictates hydroxylation versus lyase chemistry. *Angew. Chem. Int. Ed.* **2013**, *52*, 5342-5345.
(54) Das, A.; Grinkova, Y. V.; Sligar, S. G. Redox potential control by drug binding to cytochrome P 450 3A4. *J. Am. Chem. Soc.* **2007**, *129*, 13778-13779.
(55) Li, M.; Khursigara, C. M.; Subramaniam, S.; Hazelbauer, G. L. Chemotaxis kinase CheA is activated by three neighbouring chemoreceptor dimers as effectively as by receptor clusters. *Mol. Microbiol.* **2011**, *79*, 677-685.
(56) Bayburt, T. H.; Sligar, S. G. Self-assembly of single integral membrane proteins into soluble nanoscale phospholipid bilayers. *Protein Sci.* **2003**, *12*, 2476-2481.
(57) Clifton, L. A.; Neylon, C.; Lakey, J. H. Examining protein-lipid complexes using neutron scattering. *Methods Mol. Biol.* **2013**, *974*, 119-150.
(58) Wadsater, M.; Barker, R.; Mortensen, K.; Feidenhans'l, R.; Cardenas, M. Effect of phospholipid composition and phase on nanodisc films at the solid-liquid interface as studied by neutron reflectivity. *Langmuir* **2013**, *29*, 2871-2880.
(59) Wadsater, m.; Simonsen, J. B.; Lauridsen, T.; Tveten, E. G.; Naur, P.; Bjoernholm, T.; Wacklin, H.; Mortensen, K.; Arleth, L.; Feidenhans'l, R.; Cardenas, M. Aligning nanodiscs at the air-water interface, a neutron reflectivity study. *Langmuir* **2011**, *27*, 15065-15073.
(60) Glueck, J. M.; Wittlich, M.; Feuerstein, S.; Hoffmann, S.; Willbold, D.; Koenig, B. W. Integral membrane proteins in nanodiscs can be studied by solution NMR spectroscopy. *J. Am. Chem. Soc.* **2009**, *131*, 12060-12061.
(61) Hagn, F.; Etzkorn, M.; Raschle, T.; Wagner, G. Optimized phospholipid bilayer nanodiscs facilitate high-resolution structure determination of membrane proteins. *J. Am. Chem. Soc.* **2013**, *135*, 1919-1925.
(62) Kijac, A.; Shih, A. Y.; Nieuwkoop, A. J.; Schulten, K.; Sligar, S. G.; Rienstra, C. M. Lipid-protein correlations in nanoscale phospholipid bilayers determined by solid-state nuclear magnetic resonance. *Biochemistry* **2010**, *49*, 9190-9198.
(63) Kijac, A. Z.; Li, Y.; Sligar, S. G.; Rienstra, C. M. Magic-angle spinning solid-state NMR spectroscopy of nanodisc-embedded human CYP3A4. *Biochemistry* **2007**, *46*, 13696-13703.
(64) Li, Y.; Kijac, A. Z.; Sligar, S. G.; Rienstra, C. M. Structural analysis of nanoscale self-assembled discoidal lipid bilayers by solid-state NMR spectroscopy. *Biophys. J.* **2006**, *91*, 3819-3828.
(65) Ma, P.; Mohrlueder, J.; Schwarten, M.; Stoldt, M.; Singh, S. K.; Hartmann, R.; Pacheco, V.; Willbold, D. Preparation of a functional GABARAP-lipid conjugate in nanodiscs and its investigation by solution NMR spectroscopy. *ChemBioChem* **2010**, *11*, 1967-1970.
(66) Puthenveetil, R.; Vinogradova, O. Optimization of the design and preparation of nanoscale phospholipid bilayers for its application to solution NMR. *Proteins* **2013**, *81*, 1222-1231.

(67) Shenkarev, Z. O.; Lyukmanova, E. N.; Paramonov, A. S.; Shingarova, L. N.; Chupin, V. V.; Kirpichnikov, M. P.; Blommers, M. J. J.; Arseniev, A. S. Lipid-protein nanodiscs as reference medium in detergent screening for high-resolution NMR studies of integral membrane proteins. *J. Am. Chem. Soc.* **2010**, *132*, 5628-5629.
(68) Tzitzilonis, C.; Eichmann, C.; Maslennikov, I.; Choe, S.; Riek, R. Detergent/nanodisc screening for high-resolution NMR studies of an integral membrane protein containing a cytoplasmic domain. *PLoS ONE* **2013**, *8*, e54378.
(69) Yu, T. Y.; Raschle, T.; Hiller, S.; Wagner, G. Solution NMR spectroscopic characterization of human VDAC-2 in detergent micelles and lipid bilayer nanodiscs. *Biochim. Biophys. Acta* **2012**, *1818*, 1562-1569.
(70) Besenicar, M.; Macek, P.; Lakey, J. H.; Anderluh, G. Surface plasmon resonance in protein-membrane interactions. *Chem. Phys. Lipids* **2006**, *141*, 169-178.
(71) Shaw, A. W.; Pureza, V. S.; Sligar, S. G.; Morrissey, J. H. The local phospholipid environment modulates the activation of blood clotting. *J. Biol. Chem.* **2007**, *282*, 6556-6563.
(72) Glueck, J. M.; Koenig, B. W.; Willbold, D. Nanodiscs allow the use of integral membrane proteins as analytes in surface plasmon resonance studies. *Anal. Biochem.* **2011**, *408*, 46-52.
(73) Das, A.; Zhao, J.; Schatz, G. C.; Sligar, S. G.; Van Duyne, R. P. Screening of type I and II drug binding to human cytochrome P450-3A4 in nanodiscs by localized surface plasmon resonance spectroscopy. *Anal. Chem.* **2009**, *81*, 3754-3759.
(74) Tark, S.-H.; Das, A.; Sligar, S.; Dravid, V. P. Nanomechanical detection of cholera toxin using microcantilevers functionalized with ganglioside nanodiscs. *Nanotechnology* **2010**, *21*, 435502/1-435502/7.
(75) Goluch, E. D.; Shaw, A. W.; Sligar, S. G.; Liu, C. Microfluidic patterning of nanodisc lipid bilayers and multiplexed analysis of protein interaction. *Lab Chip* **2008**, *8*, 1723-1728.
(76) Zhang, Y.; Liu, L.; Daneshfar, R.; Kitova, E. N.; Li, C.; Jia, F.; Cairo, C. W.; Klassen, J. S. Protein-glycosphingolipid interactions revealed using catch-and-release mass spectrometry. *Anal. Chem.* **2012**, *84*, 7618-7621.
(77) Marin, V. L.; Bayburt, T. H.; Sligar, S. G.; Mrksich, M. Functional assays of membrane-bound proteins with SAMDI-TOF mass spectrometry. *Angew. Chem. Int. Ed.* **2007**, *46*, 8796-8798.
(78) Hebling, C. M.; Morgan, C. R.; Stafford, D. W.; Jorgenson, J. W.; Rand, K. D.; Engen, J. R. Conformational analysis of membrane proteins in phospholipid bilayer nanodiscs by hydrogen exchange mass spectrometry. *Anal. Chem.* **2010**, *82*, 5415-5419.
(79) Morgan, C. R.; Hebling, C. M.; Rand, K. D.; Stafford, D. W.; Jorgenson, J. W.; Engen, J. R. Conformational transitions in the membrane scaffold protein of phospholipid bilayer nanodiscs. *Mol. Cell. Proteomics* **2011**, *10*, M111 010876, 11.
(80) Borch, J.; Roepstorff, P.; Moeller-Jensen, J. Nanodisc-based co-immunoprecipitation for mass spectrometric identification of membrane-interacting proteins. *Mol. Cell. Proteomics* **2011**, *10*, O110 006775, 9.
(81) Zhang, X. X.; Chan, C. S.; Bao, H.; Fang, Y.; Foster, L. J.; Duong, F. Nanodiscs and SILAC-based mass spectrometry to identify a membrane protein interactome. *J. Proteome Res.* **2012**, *11*, 1454-1459.

(82) Chung, K. Y.; Day, P. W.; Velez-Ruiz, G.; Sunahara, R. K.; Kobilka, B. K. Identification of GPCR-interacting cytosolic proteins using HDL particles and mass spectrometry-based proteomic approach. *PLoS ONE* **2013**, *8*, e54942.
(83) Marty, M. T.; Zhang, H.; Cui, W.; Blankenship, R. E.; Gross, M. L.; Sligar, S. G. Native mass spectrometry characterization of intact nanodisc lipoprotein complexes. *Anal. Chem.* **2012**, *84*, 8957-8960.
(84) Marty, M. T.; Wilcox, K. C.; Klein, W. L.; Sligar, S. G. Nanodisc-solubilized membrane protein library reflects the membrane proteome. *Anal. Bioanal. Chem.* **2013**, *405*, 4009-4016.
(85) Marty, M. T.; Das, A.; Sligar, S. G. Ultra-thin layer MALDI mass spectrometry of membrane proteins in nanodiscs. *Anal. Bioanal. Chem.* **2012**, *402*, 721-729.
(86) Sloan, C. D.; Marty, M. T.; Sligar, S. G.; Bailey, R. C. Interfacing lipid bilayer nanodiscs and silicon photonic sensor arrays for multiplexed protein-lipid and protein-membrane protein interaction screening. *Anal. Chem.* **2013**, *85*, 2970-2976.
(87) Marty, M. T.; Sloan, C. D.; Bailey, R. C.; Sligar, S. G. Nonlinear analyte concentration gradients for one-step kinetic analysis employing optical microring resonators. *Anal. Chem.* **2012**, *84*, 5556-5564.
(88) Barrera, N. P.; Di Bartolo, N.; Booth, P. J.; Robinson, C. V. Micelles protect membrane complexes from solution to vacuum. *Science* **2008**, *321*, 243-246.
(89) Barrera, N. P.; Isaacson, S. C.; Zhou, M.; Bavro, V. N.; Welch, A.; Schaedler, T. A.; Seeger, M. A.; Miguel, R. N.; Korkhov, V. M.; van Veen, H. W.; Venter, H.; Walmsley, A. R.; Tate, C. G.; Robinson, C. V. Mass spectrometry of membrane transporters reveals subunit stoichiometry and interactions. *Nat. Methods* **2009**, *6*, 585-587.
(90) Barrera, N. P.; Robinson, C. V. Advances in the mass spectrometry of membrane proteins: from individual proteins to intact complexes. *Annu. Rev. Biochem.* **2011**, *80*, 247-271.
(91) Hilton, G. R.; Benesch, J. L. P. Two decades of studying non-covalent biomolecular assemblies by means of electrospray ionization mass spectrometry. *J. R. Soc. Interface* **2012**, *9*, 801-816.
(92) Zhou, M.; Morgner, N.; Barrera, N. P.; Politis, A.; Isaacson, S. C.; Matak-Vinkovic, D.; Murata, T.; Bernal, R. A.; Stock, D.; Robinson, C. V. Mass spectrometry of intact V-type ATPases reveals bound lipids and the effects of nucleotide binding. *Science* **2011**, *334*, 380-385.
(93) Felitsyn, N.; Peschke, M.; Kebarle, P. Origin and number of charges observed on multiply-protonated native proteins produced by ESI. *Int. J. Mass Spectrom.* **2002**, *219*, 39-62.
(94) Bayburt, T. H.; Sligar, S. G. Membrane protein assembly into Nanodiscs. *FEBS Lett.* **2010**, *584*, 1721-1727.
(95) Borysik, A. J.; Robinson, C. V. Formation and dissociation processes of gas-phase detergent micelles. *Langmuir* **2012**, *28*, 7160-7167.
(96) Hsu, F.-F.; Turk, J. Electrospray ionization/tandem quadrupole mass spectrometric studies on phosphatidylcholines: the fragmentation processes. *J. Am. Soc. Mass Spectrom.* **2003**, *14*, 352-363.
(97) Murphy, R. C.; Harrison, K. A. Fast atom bombardment mass spectrometry of phospholipids. *Mass Spectrom. Rev.* **1994**, *13*, 57-75.
(98) Freeke, J.; Robinson, C. V.; Ruotolo, B. T. Residual counter ions can stabilise a large protein complex in the gas phase. *Int. J. Mass Spectrom.* **2010**, *298*, 91-98.

(99) Hernandez, H.; Robinson, C. V. Determining the stoichiometry and interactions of macromolecular assemblies from mass spectrometry. *Nat. Protoc.* **2007**, *2*, 715-726.
(100) Stengel, F.; Baldwin, A. J.; Bush, M. F.; Hilton, G. R.; Lioe, H.; Basha, E.; Jaya, N.; Vierling, E.; Benesch, J. L. Dissecting heterogeneous molecular chaperone complexes using a mass spectrum deconvolution approach. *Chem. Biol.* **2012**, *19*, 599-607.
(101) Aquilina, J. A.; Benesch, J. L.; Bateman, O. A.; Slingsby, C.; Robinson, C. V. Polydispersity of a mammalian chaperone: mass spectrometry reveals the population of oligomers in alphaB-crystallin. *Proc. Natl. Acad. Sci.* **2003**, *100*, 10611-10616.
(102) Baldwin, A. J.; Lioe, H.; Robinson, C. V.; Kay, L. E.; Benesch, J. L. alphaB-crystallin polydispersity is a consequence of unbiased quaternary dynamics. *J. Mol. Biol.* **2011**, *413*, 297-309.
(103) Smith, A. M.; Jahn, T. R.; Ashcroft, A. E.; Radford, S. E. Direct observation of oligomeric species formed in the early stages of amyloid fibril formation using electrospray ionisation mass spectrometry. *J. Mol. Biol.* **2006**, *364*, 9-19.
(104) Laganowsky, A.; Reading, E.; Hopper, J. T. S.; Robinson, C. V. Mass spectrometry of intact membrane protein complexes. *Nat. Protoc.* **2013**, *8*, 639-651.
(105) Borysik, A. J.; Hewitt, D. J.; Robinson, C. V. Detergent release prolongs the lifetime of native-like membrane protein conformations in the gas-phase. *J. Am. Chem. Soc.* **2013**, *135*, 6078-6083.
(106) Ceraulo, L.; Giorgi, G.; Liveri, V. T.; Bongiorno, D.; Indelicato, S.; Di Gaudio, F.; Indelicato, S. Mass spectrometry of surfactant aggregates. *Eur. J. Mass Spectrom.* **2011**, *17*, 525-541.
(107) van der Spoel, D.; Marklund, E. G.; Larsson, D. S.; Caleman, C. Proteins, lipids, and water in the gas phase. *Macromol. Biosci.* **2011**, *11*, 50-59.
(108) Hooker, B. S.; Bigelow, D. J.; Lin, C. T. Methods for mapping of interaction networks involving membrane proteins. *Biochem. Biophys. Res. Commun.* **2007**, *363*, 457-461.
(109) Piehler, J. New methodologies for measuring protein interactions in vivo and in vitro. *Curr. Opin. Struct. Biol.* **2005**, *15*, 4-14.
(110) Babu, M.; Vlasblom, J.; Pu, S.; Guo, X.; Graham, C.; Bean, B. D.; Burston, H. E.; Vizeacoumar, F. J.; Snider, J.; Phanse, S.; Fong, V.; Tam, Y. Y.; Davey, M.; Hnatshak, O.; Bajaj, N.; Chandran, S.; Punna, T.; Christopolous, C.; Wong, V.; Yu, A.; Zhong, G.; Li, J.; Stagljar, I.; Conibear, E.; Wodak, S. J.; Emili, A.; Greenblatt, J. F. Interaction landscape of membrane-protein complexes in Saccharomyces cerevisiae. *Nature* **2012**, *489*, 585-589.
(111) Stagljar, I.; Fields, S. Analysis of membrane protein interactions using yeast-based technologies. *Trends Biochem. Sci.* **2002**, *27*, 559-563.
(112) Grinkova, Y. V.; Denisov, I. G.; Sligar, S. G. Functional reconstitution of monomeric CYP3A4 with multiple cytochrome P450 reductase molecules in Nanodiscs. *Biochem. Biophys. Res. Commun.* **2010**, *398*, 194-198.
(113) Wessel, D.; Flugge, U. I. A method for the quantitative recovery of protein in dilute solution in the presence of detergents and lipids. *Anal. Biochem.* **1984**, *138*, 141-143.
(114) Du, P.; Kibbe, W. A.; Lin, S. M. Improved peak detection in mass spectrum by incorporating continuous wavelet transform-based pattern matching. *Bioinformatics* **2006**, *22*, 2059-2065.
(115) Speers, A. E.; Wu, C. C. Proteomics of integral membrane proteins--theory and application. *Chem. Rev.* **2007**, *107*, 3687-3714.

(116) Ritchie, T. K.; Grinkova, Y. V.; Bayburt, T. H.; Denisov, I. G.; Zolnerciks, J. K.; Atkins, W. M.; Sligar, S. G. Reconstitution of membrane proteins in phospholipid bilayer nanodiscs. *Methods Enzymol.* **2009**, *464*, 211-231.
(117) Banerjee, P.; Joo, J. B.; Buse, J. T.; Dawson, G. Differential solubilization of lipids along with membrane proteins by different classes of detergents. *Chem. Phys. Lipids* **1995**, *77*, 65-78.
(118) Boldog, T.; Grimme, S.; Li, M.; Sligar, S. G.; Hazelbauer, G. L. Nanodiscs separate chemoreceptor oligomeric states and reveal their signaling properties. *Proc. Natl. Acad. Sci.* **2006**, *103*, 11509-11514.
(119) Denisov, I. G.; Baas, B. J.; Grinkova, Y. V.; Sligar, S. G. Cooperativity in cytochrome P450 3A4: linkages in substrate binding, spin state, uncoupling, and product formation. *J. Biol. Chem.* **2007**, *282*, 7066-7076.
(120) Schulz, G. E. The structure of bacterial outer membrane proteins. *Biochim. Biophys. Acta, Biomembr.* **2002**, *1565*, 308-317.
(121) Tommassen, J. Assembly of outer-membrane proteins in bacteria and mitochondria. *Microbiology* **2010**, *156*, 2587-2596.
(122) Stenberg, F.; Chovanec, P.; Maslen, S. L.; Robinson, C. V.; Ilag, L. L.; von Heijne, G.; Daley, D. O. Protein complexes of the Escherichia coli cell envelope. *J. Biol. Chem.* **2005**, *280*, 34409-34419.
(123) Ishmukhametov, R.; Hornung, T.; Spetzler, D.; Frasch, W. D. Direct observation of stepped proteolipid ring rotation in E. coli F(0)F(1)-ATP synthase. *EMBO J.* **2010**, *29*, 3911-3923.
(124) le Coutre, J.; Whitelegge, J. P.; Gross, A.; Turk, E.; Wright, E. M.; Kaback, H. R.; Faull, K. F. Proteomics on full-length membrane proteins using mass spectrometry. *Biochemistry* **2000**, *39*, 4237-4242.
(125) Weinglass, A. B.; Whitelegge, J. P.; Hu, Y.; Verner, G. E.; Faull, K. F.; Kaback, H. R. Elucidation of substrate binding interactions in a membrane transport protein by mass spectrometry. *EMBO J.* **2003**, *22*, 1467-1477.
(126) Gabant, G.; Cadene, M. Mass spectrometry of full-length integral membrane proteins to define functionally relevant structural features. *Methods* **2008**, *46*, 54-61.
(127) Alves, I. D.; Sachon, E.; Bolbach, G.; Millstine, L.; Lavielle, S.; Sagan, S. Analysis of an intact G-protein coupled receptor by MALDI-TOF mass spectrometry: molecular heterogeneity of the tachykinin NK-1 receptor. *Anal. Chem.* **2007**, *79*, 2189-2198.
(128) Cohen, S. L.; Chait, B. T. Mass spectrometry as a tool for protein crystallography. *Annu. Rev. Biophys. Biomol. Struct.* **2001**, *30*, 67-85.
(129) Gheyi, T.; Rodgers, L.; Romero, R.; Sauder, J. M.; Burley, S. K. Mass spectrometry guided in situ proteolysis to obtain crystals for X-ray structure determination. *J. Am. Soc. Mass Spectrom.* **2010**, *21*, 1795-1801.
(130) Liu, Z.; Schey, K. L. Fragmentation of multiply-charged intact protein ions using MALDI TOF-TOF mass spectrometry. *J. Am. Soc. Mass Spectrom.* **2008**, *19*, 231-238.
(131) Loo, J. A.; Edmonds, C. G.; Smith, R. D. Primary sequence information from intact proteins by electrospray ionization tandem mass spectrometry. *Science* **1990**, *248*, 201-204.
(132) Berridge, G.; Chalk, R.; D'Avanzo, N.; Dong, L.; Doyle, D.; Kim, J. I.; Xia, X.; Burgess-Brown, N.; Deriso, A.; Carpenter, E. P.; Gileadi, O. High-performance liquid

chromatography separation and intact mass analysis of detergent-solubilized integral membrane proteins. *Anal. Biochem.* **2011**, *410*, 272-280.
(133) Cadene, M.; Chait, B. T. A robust, detergent-friendly method for mass spectrometric analysis of integral membrane proteins. *Anal. Chem.* **2000**, *72*, 5655-5658.
(134) Fenyo, D.; Wang, Q.; DeGrasse, J. A.; Padovan, J. C.; Cadene, M.; Chait, B. T. MALDI sample preparation: the ultra thin layer method. *J. Vis. Exp.* **2007**, *3*.
(135) Vishnivetskiy, S. A.; Raman, D.; Wei, J.; Kennedy, M. J.; Hurley, J. B.; Gurevich, V. V. Regulation of arrestin binding by rhodopsin phosphorylation level. *J. Biol. Chem.* **2007**, *282*, 32075-32083.
(136) Denisov, I. G.; Sligar, S. G. Cytochromes P 450 in nanodiscs. *Biochim. Biophys. Acta, Proteins Proteomics* **2011**, *1814*, 223-229.
(137) Wortmann, A.; Pimenova, T.; Alves, S.; Zenobi, R. Investigation of the first shot phenomenon in MALDI mass spectrometry of protein complexes. *Analyst* **2007**, *132*, 199-207.
(138) Cohen, S. L.; Chait, B. T. Influence of matrix solution conditions on the MALDI-MS analysis of peptides and proteins. *Anal. Chem.* **1996**, *68*, 31-37.
(139) Beavis, R. C.; Bridson, J. N. Epitaxial protein inclusion in sinapic acid crystals. *J. Phys. D Appl. Phys.* **1993**, *26*, 442-447.
(140) Byeon, J. Y.; Limpoco, F. T.; Bailey, R. C. Efficient bioconjugation of protein capture agents to biosensor surfaces using aniline-catalyzed hydrazone ligation. *Langmuir* **2010**, *26*, 15430-15435.
(141) Byeon, J. Y.; Bailey, R. C. Multiplexed evaluation of capture agent binding kinetics using arrays of silicon photonic microring resonators. *Analyst* **2011**, *136*, 3430-3433.
(142) Luchansky, M. S.; Washburn, A. L.; McClellan, M. S.; Bailey, R. C. Sensitive on-chip detection of a protein biomarker in human serum and plasma over an extended dynamic range using silicon photonic microring resonators and sub-micron beads. *Lab Chip* **2011**, *11*, 2042-2044.
(143) Luchansky, M. S.; Bailey, R. C. Silicon photonic microring resonators for quantitative cytokine detection and T-cell secretion analysis. *Anal. Chem.* **2010**, *82*, 1975-1981.
(144) Luchansky, M. S.; Bailey, R. C. Rapid, multiparameter profiling of cellular secretion using silicon photonic microring resonator arrays. *J. Am. Chem. Soc.* **2011**, *133*, 20500-20506.
(145) Washburn, A. L.; Gunn, L. C.; Bailey, R. C. Label-free quantitation of a cancer biomarker in complex media using silicon photonic microring resonators. *Anal. Chem.* **2009**, *81*, 9499-9506.
(146) Washburn, A. L.; Luchansky, M. S.; Bowman, A. L.; Bailey, R. C. Quantitative, label-free detection of five protein biomarkers using multiplexed arrays of silicon photonic microring resonators. *Anal. Chem.* **2010**, *82*, 69-72.
(147) Qavi, A. J.; Bailey, R. C. Multiplexed detection and label-free quantitation of microRNAs using arrays of silicon photonic microring resonators. *Angew. Chem. Int. Ed.* **2010**, *49*, 4608-4611.
(148) Qavi, A. J.; Kindt, J. T.; Gleeson, M. A.; Bailey, R. C. Anti-DNA:RNA antibodies and silicon photonic microring resonators: increased sensitivity for multiplexed microRNA detection. *Anal. Chem.* **2011**, *83*, 5949-5956.

(149) Qavi, A. J.; Mysz, T. M.; Bailey, R. C. Isothermal discrimination of single-nucleotide polymorphisms via real-time kinetic desorption and label-free detection of DNA using silicon photonic microring resonator arrays. *Anal. Chem.* **2011**, *83*, 6827-6833.
(150) Washburn, A. L.; Gomez, J.; Bailey, R. C. DNA-encoding to improve performance and allow parallel evaluation of the binding characteristics of multiple antibodies in a surface-bound immunoassay format. *Anal. Chem.* **2011**, *83*, 3572-3580.
(151) Iqbal, M.; Gleeson, M. A.; Spaugh, B.; Tybor, F.; Gunn, W. G.; Hochberg, M.; Baehr-Jones, T.; Bailey, R. C.; Gunn, L. C. Label-free biosensor arrays based on silicon ring resonators and high-speed optical scanning instrumentation. *IEEE J. Sel. Top. Quant.* **2010**, *16*, 654-661.
(152) Sackmann, E. Supported membranes: scientific and practical applications. *Science* **1996**, *271*, 43-48.
(153) Luchansky, M. S.; Washburn, A. L.; Martin, T. A.; Iqbal, M.; Gunn, L. C.; Bailey, R. C. Characterization of the evanescent field profile and bound mass sensitivity of a label-free silicon photonic microring resonator biosensing platform. *Biosens. Bioelectron.* **2010**, *26*, 1283-1291.
(154) Binder, H.; Kohler, G.; Arnold, K.; Zschornig, O. pH and Ca2+ dependent interaction of Annexin V with phospholipid membranes: a combined study using fluorescence techniques, microelectrophoresis and infrared spectroscopy. *Phys. Chem. Chem. Phys.* **2000**, *2*, 4615-4623.
(155) Janshoff, A.; Ross, M.; Gerke, V.; Steinem, C. Visualization of annexin I binding to calcium-induced phosphatidylserine domains. *ChemBioChem* **2001**, *2*, 587-590.
(156) Kastl, K.; Menke, M.; Luthgens, E.; Faiss, S.; Gerke, V.; Janshoff, A.; Steinem, C. Partially reversible adsorption of annexin A1 on POPC/POPS bilayers investigated by QCM measurements, SFM, and DMC simulations. *ChemBioChem* **2006**, *7*, 106-115.
(157) Kastl, K.; Ross, M.; Gerke, V.; Steinem, C. Kinetics and thermodynamics of annexin A1 binding to solid-supported membranes: a QCM study. *Biochemistry* **2002**, *41*, 10087-10094.
(158) Raynal, P.; Pollard, H. B. Annexins: the problem of assessing the biological role for a gene family of multifunctional calcium- and phospholipid-binding proteins. *Biochim. Biophys. Acta* **1994**, *1197*, 63-93.
(159) Parks, G. A. Isoelectric points of solid oxides, solid hydroxides, and aqueous hydroxo complex systems. *Chem. Rev.* **1965**, *65*, 177-198.
(160) Fishman, P. H.; Pacuszka, T.; Orlandi, P. A. Gangliosides as receptors for bacterial enterotoxins. *Adv. Lipid Res.* **1993**, *25*, 165-187.
(161) Lencer, W. I.; Hirst, T. R.; Holmes, R. K. Membrane traffic and the cellular uptake of cholera toxin. *Biochim. Biophys. Acta* **1999**, *1450*, 177-190.
(162) Myszka, D. G. Kinetic analysis of macromolecular interactions using surface plasmon resonance biosensors. *Curr. Opin. Biotech.* **1997**, *8*, 50-57.
(163) Karlsson, R.; Falt, A. Experimental design for kinetic analysis of protein-protein interactions with surface plasmon resonance biosensors. *J. Immunol. Methods* **1997**, *200*, 121-133.
(164) Nguyen, B.; Tanious, F. A.; Wilson, W. D. Biosensor-surface plasmon resonance: quantitative analysis of small molecule-nucleic acid interactions. *Methods* **2007**, *42*, 150-161.

(165) Schuck, P. Use of surface plasmon resonance to probe the equilibrium and dynamic aspects of interactions between biological macromolecules. *Annu. Rev. Biophys. Biomol. Struct.* **1997**, *26*, 541-566.
(166) Yonzon, C. R.; Jeoung, E.; Zou, S.; Schatz, G. C.; Mrksich, M.; Van Duyne, R. P. A comparative analysis of localized and propagating surface plasmon resonance sensors: the binding of concanavalin a to a monosaccharide functionalized self-assembled monolayer. *J. Am. Chem. Soc.* **2004**, *126*, 12669-12676.
(167) Choi, C. J.; Cunningham, B. T. A 96-well microplate incorporating a replica molded microfluidic network integrated with photonic crystal biosensors for high throughput kinetic biomolecular interaction analysis. *Lab Chip* **2007**, *7*, 550-556.
(168) Karlsson, R.; Michaelsson, A.; Mattsson, L. Kinetic analysis of monoclonal antibody-antigen interactions with a new biosensor based analytical system. *J. Immunol. Methods* **1991**, *145*, 229-240.
(169) Morton, T. A.; Myszka, D. G.; Chaiken, I. M. Interpreting complex binding kinetics from optical biosensors: a comparison of analysis by linearization, the integrated rate equation, and numerical integration. *Anal. Biochem.* **1995**, *227*, 176-185.
(170) Bravman, T.; Bronner, V.; Lavie, K.; Notcovich, A.; Papalia, G. A.; Myszka, D. G. Exploring "one-shot" kinetics and small molecule analysis using the ProteOn XPR36 array biosensor. *Anal. Biochem.* **2006**, *358*, 281-288.
(171) Karlsson, R.; Katsamba, P. S.; Nordin, H.; Pol, E.; Myszka, D. G. Analyzing a kinetic titration series using affinity biosensors. *Anal. Biochem.* **2006**, *349*, 136-147.
(172) Rich, R. L.; Quinn, J. G.; Morton, T.; Stepp, J. D.; Myszka, D. G. Biosensor-based fragment screening using FastStep injections. *Anal. Biochem.* **2010**, *407*, 270-277.
(173) Shank-Retzlaff, M. L.; Sligar, S. G. Analyte gradient-surface plasmon resonance: a one-step method for determining kinetic rates and macromolecular binding affinities. *Anal. Chem.* **2000**, *72*, 4212-4220.
(174) Myszka, D. G.; He, X.; Dembo, M.; Morton, T. A.; Goldstein, B. Extending the range of rate constants available from BIACORE: interpreting mass transport-influenced binding data. *Biophys. J.* **1998**, *75*, 583-594.
(175) Schuck, P.; Minton, A. P. Analysis of mass transport-limited binding kinetics in evanescent wave biosensors. *Anal. Biochem.* **1996**, *240*, 262-272.
(176) Scopes, R. K. *Protein Purification: Principles and Practice*; 3rd. ed.; Springer-Verlag, 1994.
(177) Glaser, R. W. Antigen-antibody binding and mass transport by convection and diffusion to a surface: a two-dimensional computer model of binding and dissociation kinetics. *Anal. Biochem.* **1993**, *213*, 152-161.
(178) Myszka, D. G.; Morton, T. A. CLAMP: a biosensor kinetic data analysis program. *Trends Biochem. Sci.* **1998**, *23*, 149-150.
(179) Johnson, M. L. Evaluation and propagation of confidence intervals in nonlinear, asymmetrical variance spaces. Analysis of ligand-binding data. *Biophys. J.* **1983**, *44*, 101-106.
(180) Quinn, J. G. Evaluation of Taylor dispersion injections: determining kinetic/affinity interaction constants and diffusion coefficients in label-free biosensing. *Anal. Biochem.* **2012**, *421*, 401-410.

(181) Quinn, J. G. Modeling Taylor dispersion injections: determination of kinetic/affinity interaction constants and diffusion coefficients in label-free biosensing. *Anal. Biochem.* **2012**, *421*, 391-400.
(182) Karlsson, R. Affinity analysis of non-steady-state data obtained under mass transport limited conditions using BIAcore technology. *J. Mol. Recognit.* **1999**, *12*, 285-292.
(183) Rich, R. L.; Cannon, M. J.; Jenkins, J.; Pandian, P.; Sundaram, S.; Magyar, R.; Brockman, J.; Lambert, J.; Myszka, D. G. Extracting kinetic rate constants from surface plasmon resonance array systems. *Anal. Biochem.* **2008**, *373*, 112-120.
(184) Karlsson, R.; Roos, H.; Fägerstam, L.; Persson, B. Kinetic and concentration analysis using BIA technology. *Methods* **1994**, *6*, 99-110.
(185) Wilcox, K. C.; Das, A.; Kuhns, B.; Velasco, P.; Marty, M. T.; Luan, C. H.; Sligar, S. G.; Klein, W. L. Targeting toxic A beta oligomer (ADDL) receptors: Cell-free method for receptor identification and high-throughput drug screening using artificial nanoscale membranes. Program No. 637.01. 2011 Neuroscience Meeting Planner. Washington, DC: Society for Neuroscience, 2011. Online.
(186) Wilcox, K. C.; Das, A.; Velasco, P. T.; Kuhns, B. D.; Marty, M. T.; Luan, C. H.; Sligar, S. G.; Klein, W. L. Alzheimer's drug discovery using Nanodisc-stabilized receptors for oligomeric A beta. Program No. 748.04. 2012 Neuroscience Meeting Planner. New Orleans, LA: Society for Neuroscience, 2012. Online.
(187) Klein, W. L. Abeta toxicity in Alzheimer's disease: globular oligomers (ADDLs) as new vaccine and drug targets. *Neurochem. Int.* **2002**, *41*, 345-352.
(188) Klein, W. L. Synaptotoxic amyloid-beta oligomers: a molecular basis for the cause, diagnosis, and treatment of Alzheimer's disease? *J. Alzheimers Dis.* **2013**, *33*, S49-65.
(189) Krafft, G. A.; Klein, W. L. ADDLs and the signaling web that leads to Alzheimer's disease. *Neuropharmacology* **2010**, *59*, 230-242.
(190) Benilova, I.; Karran, E.; De Strooper, B. The toxic Abeta oligomer and Alzheimer's disease: an emperor in need of clothes. *Nat. Neurosci.* **2012**, *15*, 349-357.
(191) Numata, M.; Grinkova, Y. V.; Mitchell, J. R.; Chu, H. W.; Sligar, S. G.; Voelker, D. R. Nanodiscs as a therapeutic delivery agent: inhibition of respiratory syncytial virus infection in the lung. *Int. J. Nanomedicine* **2013**, *8*, 1417-1427.